NORTHWESTERN UNIVERSITY

Designing Nanostructured Oxides for Supported Metal Catalysts

A DISSERTATION

SUBMITTED TO THE GRADUATE SCHOOL
IN PARTIAL FULFILLMENT OF THE REQUIREMENTS

for the degree

DOCTOR OF PHILOSOPHY

Field of Materials Science and Engineering

By

Zhenyu Bo

EVANSTON, ILLINOIS

SEPTEMBER 2017

ABSTRACT

Supported metal catalysts find many important uses in areas including chemical production, petroleum refining and emission control. The catalytic behavior of a supported metal catalyst is influenced by size and type of reaction sites on metal nanoparticles. For many structure insensitive reactions catalyzed by the supported metal catalysts, smaller metal nanoparticles have more surface metal atoms per unit mass of metal, which are active sites for reactants, thus giving higher reactivity. Therefore it is critical to develop methods for controlling the metal particle size at synthesis stage. Meanwhile, preserving the metal particle size in the high temperature environment, as is typical of many industrial relevant reactions, remains another unsolved scientific challenge. Many studies before have proposed different synthesis strategies to control the size of the metal nanoparticles, though studying the size and the reactivity of the catalyst post synthesis are both important.

To modify the support in this thesis, a support material (TiO_2 and Al_2O_3) is first grafted with bulky organic templates then sol-gel coated with a nanometer thick oxide overcoat followed by subsequent treatment to remove the organic templates. After this, metals (Ag and Pt) are deposited onto the modified support materials via photodeposition, wetness impregnation or strong electrostatic adsorption to generate the supported metal catalysts. In the first study of photodepositing Ag nanoparticles onto SiO_2 partially overcoated TiO_2 support, the combined use of sol-gel overcoat and organic templates helped generate highly dispersed Ag nanoparticles (<5nm) on TiO_2 supports and preserved the metal particle size up to 450°C for prolonged time. In the next study of synthesizing highly dispersed TiO_2 supported Pt nanoparticles, Pt nanoparticles were deposited onto TiO_2 supports with partially overcoated SiO_2 through wetness impregnation. The as-synthesized Pt nanoparticles are 1-2 nm by electron microscope

characterization and maintain dispersion (percent of surface atoms) >45% by CO chemisorption even after prolonged heating at 500 °C, whereas Pt nanoparticles on unmodified TiO_2 are less dispersed (~33%) and their dispersion falls further upon prolonged heating. Ethylene hydrogenation reaction study demonstrated that the Pt nanoparticles on modified TiO_2 preserve the catalytic activities of Pt on unmodified TiO_2. In the following study, strong electrostatic adsorption is proved to be a self-limiting approach to prepare highly dispersed supported Pt catalysts.

The structure of active sites not only affects the catalytic behavior of supported metal nanoparticle catalysts but also influences the catalytic behavior of supported oxide catalysts. Therefore controlling the structure of supported oxides is important when preparing supported oxide catalysts, and various physical and chemical tools have been used to characterize the materials post synthesis. Among all characterization tools, direct visualization of active sites on supported oxide catalysts using electron microscope remains challenging. Here, an approach that uses molecular precursors and 2D oxide supports to enable direct visualization of highly dispersed supported oxide catalysts has been developed to prove the existence of isolated Ta sites on the TiO_2 support.

In summary, novel approaches for synthesizing highly dispersed thermal stable supported metal catalysts have been developed in this thesis and can be applied to scale-up synthesis of many other supported metal catalysts.

ACKNOWLEDGEMENT

The author wants to thank the U.S Department of Energy, Office of Science, Office of Basic Energy Science, and Northwestern University Institute for Catalysis in Energy Processes for funding support. Portion of the work was completed in EPIC facility of the NUANCE Center at Northwestern University, which has received support from the Soft and Hybrid Nanotechnology Experimental (SHyNE) Resource (NSF NNCI-1542205); the MRSEC program (NSF DMR-1121262) at the Materials Research Center; the International Institute for Nanotechnology (IIN); the Keck Foundation; and the State of Illinois, through the IIN. This work also involves using the Advanced Photon Source, which is supported by the U.S. Department of Energy under Contract DE-AC02-06CH11357.

I want to thank all of the collaborators including Alex Ardagh, Sol Ahn, LingXuan Peng, Dr. Nick Thornburg, Lauren McCullough and Sam Dull for their contributions in my work and their generous help throughout my Ph.D career.

I want to thank my advisor Dr. Justin Notestein for his continuous support, advice and help throughout my Ph.D career.

I want to thank Dr. Neil Schweitzer for his help and insights in the reaction study. I also want to thank all committee members including Dr. Justin Notestein, Dr. Michael Bedzyk, Dr. Scott Barnett and Dr. Yip Wah Chung for their time and commitments.

Last but not least, I want to thank my family and friends for their encouragement and help. Ph.D study is not an easy journey, I won’t be able to finish it without their support.

Table of Contents

List of Tables, Figures and Illustrations

Tables

Figures

Illustrations

Chapter 1

Current Challenges in Supported Metal Catalysts

1.1 Introduction

Catalysts are used in reactions to decrease the activation energy barrier therefore increase the speed of the reaction. Given that a catalyst can specifically accelerate the rate of a certain reaction and improve the product selectivity in a reaction, it is widely used in many important industrial processes and scientific studies.[2, 3] In particular, heterogeneous catalysts are solid materials that catalyze reactions in the gas or liquid phase, and are essential in chemical manufacturing, fuel production and emission control.[2, 3] Supported metal catalysts, made out of highly dispersed metal nanoparticles supported on high surface area supports, is an important category in heterogeneous catalysts which finds many important uses in modern society. For example, supported Pd catalysts are used in catalytic converters for oxidation of pollutants including CO and unburned hydrocarbon,[4] supported Pt catalysts are used in petroleum refining to convert low octane to high octane gasoline[5] and supported Au catalysts are used in removal of CO at room temperature[6] and production of hydrogen in water-gas shift reactions.[7]

Therefore, it is critical to understand the relationship between structure and catalytic performance of supported metal catalysts in order to develop new catalysts. In particular, the size of the metal nanoparticle is a critical determinant in catalytic activities and selectivity. Previous studies show many catalysts achieve high catalytic reactivity when the supported metal nanoparticles are highly dispersed.[8-10] This is because in many structure-insensitive reactions catalyzed by the supported metal catalysts, smaller metal nanoparticles have higher fraction of surface metal atoms, which are accessible to reactants and available for catalysis.[10-12] Therefore, much effort is focused on controlling the metal nanoparticle size and understanding the size effects. While metal nanoparticles can be deliberately synthesized then deposited on supports, most catalysts are prepared by some form of controlled deposition of a metal salt then reduction, including incipient wetness impregnation,[13, 14] strong electrostatic adsorption,[13, 15, 16] deposition-precipitation[13, 17] or surface organometallic chemistry approaches.[13, 18, 19] The catalysis community continues to seek new synthesis methods capable of generating highly dispersed supported metal catalysts with significant metal loading.

While controlling the size of metal nanoparticles at the synthesis stage is challenging, preserving the size of metal nanoparticles in the reaction stage also remains challenging. In the high temperatures typical of many important reactions or catalyst regeneration procedures, catalytic nanoparticles can grow by Ostwald ripening or particle migration.[20-22] Ostwald ripening involves detachment and migration of metal atoms from one metal nanoparticle into the other metal nanoparticle, which results in the growth of larger metal nanoparticles at the expense of smaller metal nanoparticles.[23] Particle migration, on the other hand, involves diffusion and coalescence of metal nanoparticles on the support surface.[24] In both cases, the average particle size increases and the fraction of geometrically accessible metal decreases, which results in the deactivation of the catalyst and possible changes of selectivity. Many factors including the size of the metal nanoparticle, support materials and distribution of metal nanoparticles can affect the rate of sintering.[25, 26]

To combat the issues of thermal deactivation of supported metal catalysts, several strategies have been proposed including modifying the metal nanoparticles by alloying,[21] modifying the surface of supported metal catalysts by overcoating,[27-29] and using nanostructured support materials to immobilize metal nanoparticles.[21, 30, 31] By incorporating a second metal with higher melting point, the thermal deactivation of the metal nanoparticles can be reduced. For example, a previous report shows that the thermal stability of Pt nanoparticles is significantly improved by alloying Pt nanoparticles with Rh, which has a melting point ~200°C higher than Pt.[21] A second oxide layer, deposited onto the surface of supported metal catalysts via the Atomic Layer Deposition (ALD) or the Sol-gel based method, can restrain the diffusion and migration of metal nanoparticles or adatoms on the support surface, therefore enhancing the thermal stability of supported metal catalysts.[27, 28, 32] Stair's group at Northwestern University used ALD deposited Al_2O_3 overcoat to enhance the thermal stability of supported Pd catalysts up to 675°C.[28] Campbell's group at University of Washington also reported improved thermal stability of supported Pt catalysts after selective deposition of SiO_2 overcoat on the surface.[27]

Porous support materials, such as mesoporous silica and carbon nanotubes, can be used to enhance the thermal stability of supported metal catalysts by confining nanoparticles inside the pores.[21, 30, 32] For instance, Datye's group at University of New Mexico demonstrated that the thermal stability of Au nanoparticles was improved by embedding the Au nanoparticles inside a mesoporous Silica structure.[33-35] Though all these strategies show improved thermal stability of metal nanoparticles, the use of specialized metal nanoparticle syntheses (e.g. ligand-assisted colloidal synthesis) or deposition methods (e.g. ALD) limits the application of these methods in high volume production of industrial-relevant catalysts. Moreover, use of bulk porous support materials or direct surface deposition of a second oxide introduces the possibility that some of the active metal surface may be covered, negating some of the benefits of the smaller particle sizes. Therefore, the catalysis community is continuously searching for new strategies to prepare highly dispersed thermally stable supported metal catalysts.

1.2 Methods for Synthesizing Supported Metal Catalysts

As mentioned above, highly dispersed supported metal catalysts are generally favored in the catalysis community given that they have higher portion of surface metal atoms, which allows accessibility for the reactants.[8, 10] Among various catalyst preparation methods, photodeposition, wetness impregnation, metal complex grafting and strong electrostatic adsorption (SEA) are utilized in this study to prepare highly dispersed supported metal catalysts.

Incipient wetness impregnation is a commonly used technique in chemical industry to prepare heterogeneous catalysts.[13] Typically, the metal precursor is first dissolved in an aqueous or organic solvent with the volume determined by the pore volume of the support materials, the concentration of the metal precursor is calculated so that the deposited metal precursor can give the desired loading of metals on the supports. Once the prepared solution wets the support and totally fills the pores, the solvent is removed by air drying, heat treatment or vacuum assisted drying. Care should be taken in this process as the solvent removal rate will affect the final dispersion of metal precursor on the support.[13] After the solvent is removed, the as-prepared catalyst needs further calcination or reduction treatment before it is used in reactions (the process is illustrated in figure 1.2.1). Though wetness impregnation is a scalable synthesis method and can be used to synthesize many different supported metal catalysts, it lacks control of the dispersion of metals on the support.

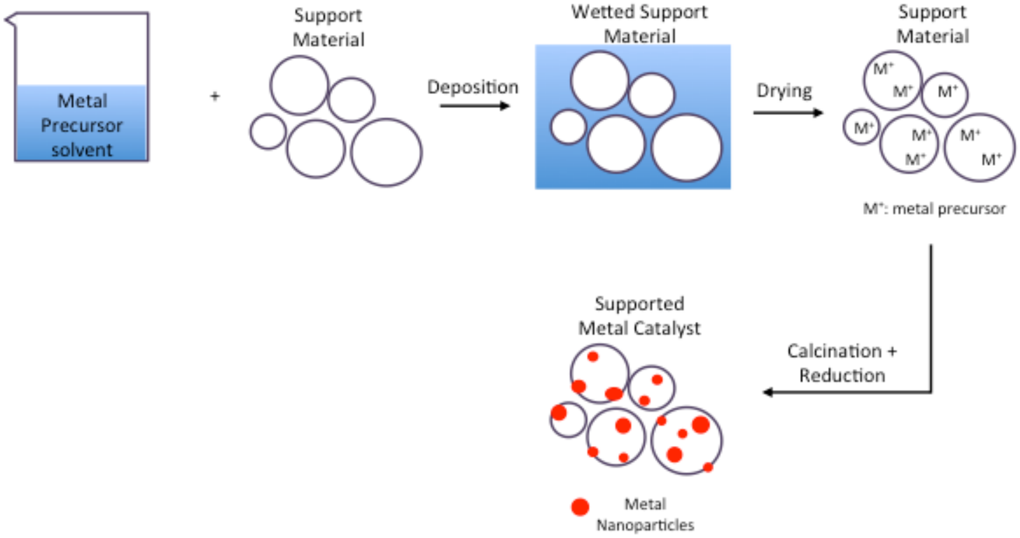

Figure 1.2.1. A schematic drawing demonstrates the incipient wetness impregnation process for preparing a supported metal catalyst.

The metal complex grafting approach is a method to prepare highly dispersed supported metal catalyst and to facilitate strong binding between metals and the support material.[13, 36] In a typical grafting experiment, selected organometallic compounds in gaseous or liquideous form are deposited onto the support surface and react with the surface functional groups (ex. hydroxyl groups) to form chemical bonds. Depending on the types of reactions, the organics can be removed by post treatments such as calcination (the reaction mechanism is illustrated in figure 1.2.2). One big advantage of using metal complex grafting technique is that the structure of the active site can be easily tuned by changing the size and the geometry of the organometallic compound.[13] However, the use of highly reactive organometallic compounds poses challenges to the experiment setup (ex. inert gas environment), which limits its use in the scale-up productions of supported metal catalysts.

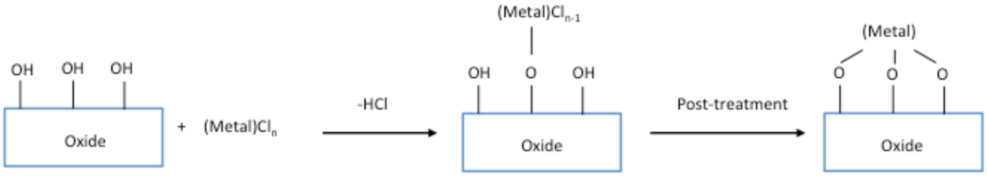

Figure 1.2.2. A schematic drawing illustrates grafting metal complexes containing chlorine groups onto an oxide support.

Photodeposition is a metal nanoparticle deposition technique that reduces and deposits metal ions (ex. Pt, Ag and Au) onto photoactive semiconductor support materials (ex. TiO_2) when illuminated with light.[37, 38] During the photodeposition process, photons first excite electrons of a semiconductor support material, moving them from the valence band into the conduction band. Then, the photon-excited electrons transfer from the support material to the surface-bound metal ions, initiating cycles of electron transfer and ion reduction that can grow metal nanoparticles on the surface of support material (the mechanism is illustrated in figure 1.2.3).[37] Photodeposition is a facile synthesis approach to deposit metal nanoparticles onto photoactive support materials, and typical post treatments in catalysts preparation, including calcination and reduction, are not required in this approach, therefore shortening the catalyst preparation time.[37] However, the use of a photoactive support material in photodeposition limits its use in preparing many widely used supported metal catalysts.

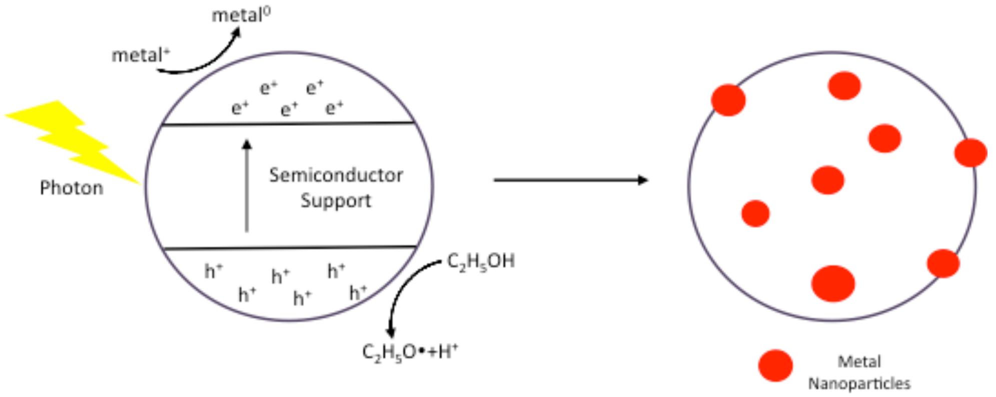

Figure 1.2.3. A schematic drawing illustrates photodepositing metal nanoparticles onto a semiconductor support material using ethanol as a sacrificial reagent.

Strong Electrostatic Adsorption (SEA) is another approach to synthesize highly dispersed supported metal catalysts. An oxide surface has hydroxyls that can be deprontonated or prontonated depending on the pH of the solution environment. The pH at which the surface hydroxyl groups remain neutral is defined as the Isoelectric Point (IEP). Above the IEP, the predominate surface species are -O^-, while the predominate surface species are –OH^{2+} below the IEP. In both scenarios, metal anion or cation complexes can be deposited onto the oxide surface through electrostatic interaction.[13, 39] In a typical SEA experiment, a support material is dispersed in a pH adjusted aqueous solvent containing the metal precursor ions. Then the mixture is shaken, filtered and dried followed by necessary post treatments to produce the desired catalyst. The amount of metal ions adsorbed is determined by the surface hydroxyl group density, the solution pH, and the size of the precursor ion.[13, 39] Theoretically the maximum density of adsorbed metal complexes corresponds to a monolayer of adsorbed metal complexes, therefore limiting the maximum loading of metals on the support.[13]

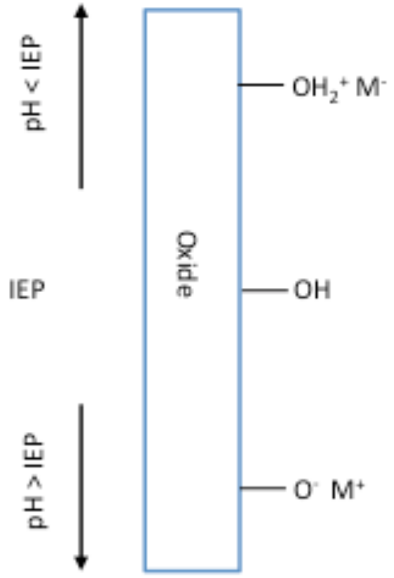

Figure 1.2.4. A schematic drawing illustrates electrostatic interaction between metal ions and the surface hydroxyl groups.

1.3 Oxide Overcoating Methods

Oxide overcoating is utilized to modify the surface of support materials to improve the dispersion and thermal stability of metal nanoparticles also to tune the catalytic behaviors of supported metal catalysts. Among different types of overcoating methods, sol-gel deposition and ALD are the two commonly used oxide overcoating methods in catalysis field.

Sol-gel deposition, by its definition, is a process that involves generation of a colloidal suspension, which later is converted to a layer of solid material onto the support. There are six major steps involved in a sol-gel deposition process including hydrolysis and condensation of a metal alkoxide precursor to form the colloidal, gelation and aging of the as-formed colloidal to develop cross-links, finally drying and optional thermal treatment of the cross-linked colloidal to remove volatile species and to form a dense solid layer of overcoat.[40] In this study, a sol-gel based SiO_2 deposition process was utilized to deposit SiO_2 overcoat onto various oxide supports. In a typical SiO_2 deposition process, one cycle of SiO_2 deposition on the support is achieved by hydrolysis of Tetraethyl orthosilicate (TEOS) through a base catalyzed reaction followed by subsequent formation of SiO_2 on the support surface. More SiO_2 can be deposited onto the support by adding more TEOS precursor to initiate another cycle of deposition process. In the end, the coated support is filtered and dried followed by necessary post treatments.[41, 42] There are many advantages associated with using sol-gel deposition to overcoat the support including mild reaction environment, no requirement of specialized instrument and control of overcoat properties through post treatments.[40] Several research groups have used sol-gel overcoating approach to modify the support surface for stabilizing metal nanoparticles. For example, Dai's group at Oak Ridge National Lab has reported generating sinter resistant Au nanoparticles on the TiO_2 support with sol-gel deposited Al_2O_3. [43]Campbell's group also reported that Pt nanoparticles on TiO_2 fiber support modified with sol-gel coated SiO_2 show improved thermal stability up to 700°C.[27]

ALD is another process that can overcoat the support by atomic precision. In a typical ALD process, a volatile precursor is introduced into the chemical reaction chamber containing the support first. Once the precursor molecules saturate the support surface, the excess is purged away. Then the second precursor is introduced into the chamber to react with the pre-adsorbed molecules and form a layer of overcoat on the support surface. The whole process can be repeated to give desired overcoat thickness. The self-limiting aspect of ALD makes it a suitable process to deposit conformal overcoat on high aspect ratio structures.[44, 45] However, the slow reaction time limited by gas phase diffusion of reactant molecules and limited selection of precursors hinder the broad application of ALD in modifying the catalyst support surface.

ALD of a second oxide onto the supported metal catalyst has been reported to stabilize metal nanoparticles against sintering in harsh reaction environment (ex. Elevated temperature). Stair's group at Northwestern University reported using ALD Al_2O_3 overcoat to stabilize supported Pd metal nanoparticles in methanol decomposition at 270 °C.[29] Dumestic's group at University of Wisconsin demonstrated using ALD Al_2O_3 overcoat to stabilize supported Cu catalyst in liquid-phase reaction.[46] ALD of a second oxide overcoat can also tune the catalytic behavior of the catalyst by preferentially blocking the unwanted reaction sites. For example, Stair's group at Northwestern University has reported using ALD Al_2O_3 to cover the edge and corner Pd atoms thus inhibit the unwanted C-C bond cleavage reaction in the oxidative dehydrogenation of ethane reaction.[29]

1.4 **Tools for Characterizing Supported Metal Catalysts**

Studying the structure of the as-synthesized supported metal catalysts is critical to understand the structure-performance relationship of the supported metal catalysts.[18] Given that the size of a metal nanoparticles is usually in nanometer range and the morphology of many widely used support materials is complex, characterizing a supported metal catalyst can be challenging thus requires the use of both physical and chemical characterization tools. In my research, physical characterization tools including Thermal Gravitational Analysis (TGA), N_2 physisorption, X-ray Diffraction (XRD), Transmission Electron Microscope (TEM), X-ray Photoemission Spectroscopy (XPS), Inductively Coupled Plasma Atomic Emission Spectroscopy (ICP-AES) and Extended X-ray Absorption Fine Structure (EXAFS) were used to understand the structure of both metal nanoparticles and the support. In the meantime, chemical characterization tools including CO-chemisorption and CO-Fourier Transform Infrared Spectroscopy (CO-FTIR) were used to better understand the dispersion and the structure of the metal nanoparticles.

TGA is a type of thermal analysis, which can measure the weight change of a material as a function of increasing temperature.[47] In my research, TGA was used to quantify the mass of template molecules (Calixarene) grafted on a support by decomposing the templates in oxidative environment with temperature increasing from room temperature up to 1073K. Since Calixarene decomposes at ~573K with the presence of oxygen, the majority of the mass loss of a support between 573K and 1073K belongs to the loss of templates.[41]

N_2 physisorption is a technique to understand the surface area and porosity of a support material by measuring the adsorbed N_2 volume at different N_2 equilibrium pressure at the boiling temperature of N_2 (77K). The relative pressure changes during the N_2 adsorption and desorption is measured in a typical N_2 physisorption experiment, then different adsorption theories are applied to calculate the surface area and other physical properties.[48] One commonly used theory is Brunauer–Emmett–Teller (BET) theory, which assumes multilayer adsorption of gas molecules on a sample surface and no interaction between different layers of gas molecules. To calculate BET surface area, the monolayer adsorbed N_2 volume (vm) is first estimated using the following equations:

$$\frac{1}{v[\left(\frac{p0}{p}\right)-1]} = \frac{c-1}{vm*c} * \left(\frac{p}{p0}\right) + \frac{1}{vm*c} \ [1]$$

$$c = \exp\left(\frac{E1-El}{RT}\right)[2]$$

Where p and p0 represent the equilibrium pressure and saturation pressure, v is the total adsorbed gas quantity and c is the BET constant. C is calculated using E1 and El, which stand for heat of adsorption for the first layer of N_2 molecules and heat of adsorption for the second and more layers of N_2 molecules. Once vm is calculated, the BET surface area (S) is calculated using the following equation:

$$S = \frac{(vm*N*s)}{V} \quad [3]$$

Where N stands for Avogadro's number, s is the cross section of the adsorbing species and V is the molar volume of the gas.[49] N_2 physisorption is used to measure the surface area and the porosity of as-synthesized support materials.

XRD is a technique that can determine the crystal structure of a crystalline material. In a typical XRD experiment, X-rays is first generated after a target material (ex. Cu) is hit by the electrons originated from a cathode, then the X-ray is directed onto the sample surface and the reflected X-ray signals will be recorded by a detector. When the reflected X-ray has constructive interference, a peak in intensity occurs. XRD is used to identify the crystal structure of the as-synthesized catalysts.[50]

TEM is a technique that uses the electrons to interact with the specimen to form images. Under imaging condition, electrons are first generated from a filament on the top of the microscope, then a condenser lens converges the electron beam onto the sample. Once the electron beam transmits through the sample, the underneath objective lens diverges the beam and the image is formed on a fluorescent screen on the bottom of the microscope. Given the resolution of modern TEM is below 1nm, TEM is widely used in the catalysis community to characterize the morphology of many supported metal catalysts, which have metal nanoparticles with sizes below 10nm.[50]In particular, the dimension and size information of the supports and metal nanoparticles can be collected from the TEM images, and the metal particle size distribution for individual catalyst can be computed.

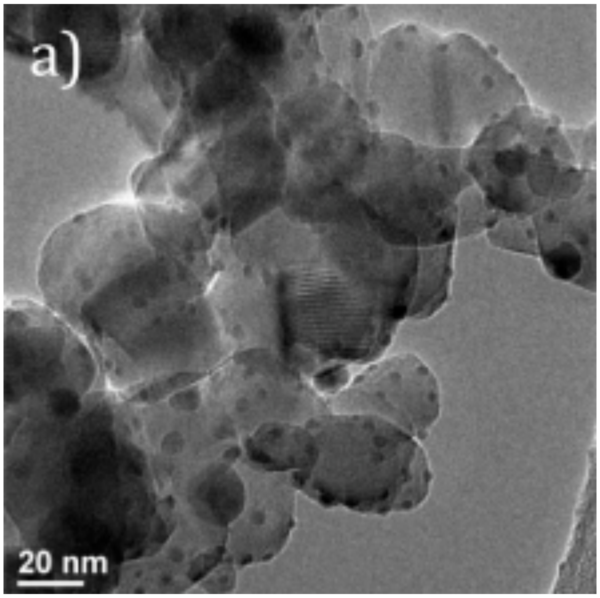

Figure 1.4.1 A TEM image of TiO_2 supported Ag shows the Ag nanoparticles (darker particles) supported on the TiO_2 support (chain like particles)

XPS is a technique that can analyze the surface chemistry of a material. In a typical XPS experiment, a sample is first irradiated with a beam of X-rays under ultra high vacuum condition, simultaneously the kinetic energy and number of emitted photoelectrons are counted and analyzed. The measured energies and intensities of the electrons are used to identify the elements existing on the surface and their chemical states. XPS can be used to identify the elements existing on the surface of the supported metal catalysts and study their oxidation states.[50]

ICP-AES is a technique that can detect the trace elements in a solvent. In a typical ICP-AES experiment, the ions in a sample solvent are excited by the inductive coupled plasma and emit electromagnetic radiation at wavelengths characteristic of a specific element, the intensity and the wavelength of the radiation are recorded and analyzed to give the element and concentration information. ICP-AES can be used to quantify the loading of metals on the supports.[51]

EXAFS is part of the X-ray Absorption Spectroscopy (XAS) technique that can measure the chemical state and local binding environment of existing elements in a sample. In a typical XAS experiment, a thin piece of sample is radiated with X-rays having a narrow energy window, the intensity of transmitted X-rays is recorded when the X-ray energy is increased. During this process, if the incident X-ray energy matches the binding energy of a electron in an atom in the sample, the X-ray is absorbed thus causes a drop in the energy intensity of the transmitted X-ray, this change in energy intensity is defined as an absorption edge. The excited photoelectrons from an atom have wave like behaviors and the neighboring atoms can cause back-scattered electron waves, oscillations in the XAS spectra are observed when back-scattered electron waves interfere with the forward-propagating electron wave. Useful structural information such as binding distance between atoms can be extracted by analyzing the oscillations.[50] In this study, EXAFS experiment was completed in Argonne National Lab using the X-rays from the synchrotron source to estimate the average particle size of the highly dispersed Ag nanoparticles (<5nm) on an oxide support.

Besides the physical characterization tools, chemical characterization tools were also used in my research to study the dispersion and accessibility of metal atoms in the particles to the reactant molecules. CO chemisorption is a technique that measures the number of metal surface atoms for a few metal elements including Pt and Pd. In a typical CO chemisorption experiment, the CO molecules are dosed repeatedly into an air-free reactor containing a reduced sample material at room temperature. The quantity of exhausted CO molecules are measured, and the quantity of chemically adsorbed CO molecules is calculated as the difference between the total amount of CO molecules dosed into the chamber and the total amount of CO molecules exhausted. The quantity of surface metal atoms can be calculated if an adsorption ratio between

CO molecules and metal atoms is assumed. Finally, the dispersion of metal nanoparticles can be calculated using the following equation:[52, 53]

$$D = \frac{moles\ of\ the\ surface\ metal\ atoms}{total\ moles\ of\ the\ metal\ atoms\ on\ a\ support} \quad [4]$$

CO-FTIR, on the other hand, is a technique that tells the oxidation states and coordination states of the surface metal atoms. Similar to the process of the CO chemisorption experiment, CO molecules are first dosed onto the surface of a reduced sample inside an air free chamber, then the excess CO molecules are purged away. After the purge, IR illuminates the sample surface with the presence of chemically adsorbed CO molecules and the reflected IR signals are collected. The collected signals are further analyzed and processed by Fourier transformation to reveal the vibrational modes of CO molecules. Each peak in the IR spectrum refers to a type of binding mode between CO molecules and the surface metal atoms thus revealing the coordination information of the metal atoms on the support.[54]

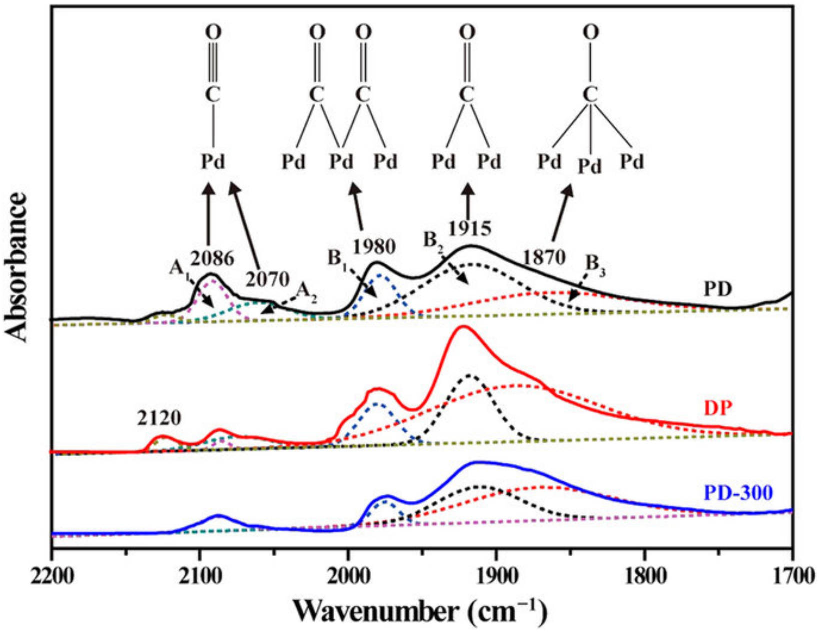

Figure 1.4.2. CO-FTIR characterization of TiO_2 supported Pd reveals the coordination information of Pd atoms on the support.[55]

1.5 Probe reactions for supported metal catalysts

The kinetic data of as-synthesized samples is obtained from the probe reaction for comparing the catalytic performance of different samples. Among different ways of calculating reaction rates, the turn over frequency (TOF) is a commonly used parameter to evaluate the reactivity of a sample. TOF reveals the specific reactivity of a catalytic site for a specific reaction under defined reaction condition, it can be calculated using the equation below:[56]

$$\mathrm{TOF}=\frac{volumetric\ rate\ of\ reaction}{moles\ of\ active\ sites/volume} \quad [5]$$

For many reactions catalyzed by supported metal catalysts, the TOF measures the intrinsic reactivity of the metal active site rather than the whole catalyst, therefore giving more meaningful reactivity comparison between metal nanoparticles sitting on different supports.

In this study, both ethylene and propylene hydrogenation reactions were used to study the catalytic activities of Pt nanoparticles on various supports. These two reactions are structure insensitive reactions, which are not expected to exhibit dependency of turn over rate on particle size.[57] In both reactions, alkene molecules first chemically adsorb onto a Pt nanoparticle surface then the double bond in the molecules dissociate. After that, the adsorbed alkene can react with a nearby dissociated H_2 molecule to form alkanes, which later desorb from the metal surface.[58, 59]

Chapter 2

Photodepositing Ag onto Nanostructured SiO_2 Partially Overcoated TiO_2

2.1 Introduction

Photodeposition has been reported as a rapid method to synthesize supported metal nanoparticles such as Au or Ag on a semiconductor oxide support, typically TiO_2.[37] Under UV illumination (365nm), electrons in the TiO_2 valence band move to the conduction band where they can reduce adsorbed metal ions. Typically, ethanol is employed as the sacrificial reductant. The photodeposition method features very short synthesis times (<100 s) and can offer good control of particle sizes in the base case (~5 nm),[37] although particle sizes are very sensitive to illumination time, precursor concentration, and other factors. Here, Ag/TiO_2 catalysts are synthesized by selective photodeposition. In addition to photocatalysis applications, TiO_2 is an important oxide support for many heterogeneous catalyst applications due to its strong interaction with metal nanoparticles that gives unique catalytic activities.[60, 61] Ag nanoparticles have antimicrobial properties,[62] are benchmark catalysts for ethylene oxide synthesis,[63] and have been investigated extensively in reactions such as selective hydrogenation[64] and NOx reduction.[65]

Here, TiO_2 particles are partially overcoated (masked) with thin layers of SiO_2 and are used as a support for Ag nanoparticle photoreduction (Scheme 1). The resulting Ag nanoparticles are characterized by transmission electron microscopy (TEM) and Extended X-ray Absorption Fine Structure (EXAFS) analysis. This route is demonstrated as a novel method to synthesize well-separated, supported metal nanoparticles that are smaller, more homogeneous in size, and have better resistance to thermal growth than particles grown on unmodified TiO_2 supports or other controls. To the best of our knowledge, this concept of backfilling metal nanoparticles into a partially-masked support is a novel approach to the controlled growth of supported metal catalysts with enhanced sintering resistance Experiments.

2.2 Experiments

Synthesis

TiO_2 was decorated with calixarenes by a modification of a previously reported procedure.[66] TiO_2 (4g, 20-30 nm primary particle size, 71 m^2/g BET surface area, Degussa Evonik P25) was heated at 110°C under dynamic vacuum overnight to remove residual water. The dried particles were suspended in a solution of t-butylcalix[4]arene ('calixarene', $C_{44}H_{56}O_4$, >99%, Sigma-Aldrich) in 200 mL toluene and heated to reflux overnight. The mass of added calixarene was varied to control the final calixarene surface loading. See Scheme 1 for the details of materials syntheses. The calixarene-TiO_2 was washed with ~200 mL toluene and ~200 mL hexane, then vacuum dried overnight.

TiO_2 was coated with SiO_2 using base-catalyzed condensation of limiting amounts of tetraethyl orthosilicate (TEOS). TiO_2 (~1g, modified or unmodified with calixarenes) was dispersed in 128 mL ethanol (200 proof), 6.4 mL NH_4OH (28-30 wt%, aqueous) were added and sonicated for 30 min, ~0.1 mL TEOS (reagent grade, 98%, Sigma-Aldrich) was added, and the mixture was shaken for 1 h. This constitutes one cycle of SiO_2 coating on TiO_2. The coating was repeated for up to 8 cycles by repeated addition of NH_4OH and TEOS. After the final cycle, the materials were vacuum dried, heated in air (20°C/min to 325°C, hold 1 h), then treated in O_3 (HG 1500 ozone generator, Ozone Solutions Inc.) at 110°C for 2h to generate supports S1, S1a, S2, S3, and S4. Sample details are given in Table 1 and Scheme 1. Support materials for control samples, including those without calixarene templates or SiO_2 overcoats, received identical post-treatment.

Modifying a method from a previous report,[37] Ag was photodeposited by the following method. Approximately 50mg TiO_2 or the supports S1-S4 were dispersed in 1000 mL ethanol (190 proof, 95% ethanol 5% H_2O), sonicated for 10 min, then $AgNO_3$ (ACS grade, 99.0%, Sigma-Aldrich) was dissolved into the suspension with stirring to reach 0.5 mM unless otherwise noted, and the mixture was purged with N_2 for 30 mins to remove dissolved O_2. A UV light probe (365nm, 1.2 W/cm^2 UV Pen-ray) was inserted into the stirred suspension via a quartz sheath (see Figure 2.2.1) and illuminated for 5-120s. The resulting Ag-containing materials were filtered and washed with ~200 mL ethanol (190 proof), then air dried. Samples of Ag deposited on unmodified TiO_2 are denoted as T1-T4, while Ag deposited on the modified samples are denoted as N1-N4. Selected materials were heated with a ramp of 20°C/min to 450°C and held 2 h under He and are denoted, for example, sN1.

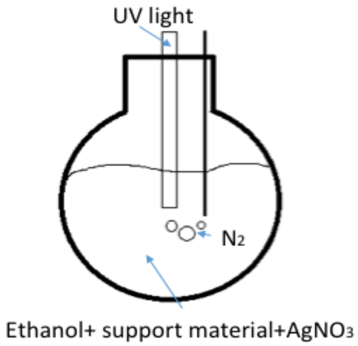

Figure 2.2.1. Schematic drawing of setup for photodeposition of Ag on the support material.

Characterization

N_2 physisorption was carried out on a Micrometrics ASAP 2020 and surface areas calculated using the Brunauer–Emmett–Teller (BET) method, while micropore volumes were calculated from t-plots. Materials were vacuum dried at ~180 °C overnight before N_2 physisorption. Thermogravimetric analysis was carried out using a TA Instruments Q500 under 90/10 O_2/N_2 flow. Template molecule decomposition begins above 300°C and constitutes the primary mass loss between 300°C and 800°C. The template surface density in calixarene.nm^{-2} was calculated by dividing the fractional mass loss between 300°C and 800°C by the molecular weight of the combusting calixarene fragment (649 g/mol) and the specific surface area of the original TiO_2 support (71 m^2/g). Diffuse reflectance UV-visible spectra were acquired in a Shimadzu UV-3600 and a Harrick Praying Mantis. Ag loading was determined using a Varian Vista MPX ICP-OES with sample digestion in HF/HNO_3. Transmission electron microscopy (TEM) was performed using a JEOL 2100 Fast TEM operated at 200 kV. Samples were prepared by dispersing in ethanol, sonicating, then letting a drop air-dry onto grids. Ag nanoparticle sizes are given as number- and volume-weighted averages. Volume average particle diameter (d_V) is calculated using equation 1:

$$d_V = \left(\frac{\sum d_i^6}{\sum d_i^3}\right)^{1/3} \qquad (eq. 1)$$

where d_i are individual nanoparticle diameters assuming spherical geometries for nanoparticles observed in TEM. The volume-weighted average better accounts for rare, large particles, and compares more directly from estimates of particle size from EXAFS fitting, which is sensitive to all atoms in the sample.

Benzyl alcohol photooxidation with ambient O_2 was used to probe the residual exposed TiO_2 surface after SiO_2 deposition. Following a prior report,[67] 8 mL of 5 mM benzyl alcohol and 8 mM dodecane internal standard in freshly distilled acetonitrile was added to a quartz test-tube containing approximately 10 mg of catalyst powder. Illumination was provided by the same UV light probe as above. The products were determined by a Shimadzu 2010 GC/FID system with a TR-1 capillary column, and compared to authentic standards of benzyl alcohol and benzaldehyde.

X-ray absorption spectra were acquired at the Ag K-edge (25.514 keV) on the bending magnet beam line of the Materials Research Collaborative Access Team (MRCAT) at the Advanced Photon Source, Argonne National Laboratory. Transmission step-scan mode was used to collect the data. A water-cooled, double-crystal Si(111) monochromator, detuned by approximately 50% for reducing harmonic reflections, was used to select photon energy. The ionization chamber was optimized to obtain maximum current with linear response ($\sim 10^{10}$ photons detected/s), 10% adsorption in the incident ion chamber and 70% adsorption in the transmission X-ray detector. Energy calibration was completed using the spectrum of Ag foil that was acquired simultaneously with each sample measurement. WINXAS 3.1 was used to fit the data based on standard data reduction techniques. Standard methods were used to obtain the normalized, energy-calibrated absorption spectra. The edge energy was calculated from the maximum of the first peak in the first derivative of the XANES spectrum. Ag foil was assumed to have 12 Ag-Ag interactions at 2.89 Å and was used to measure backscattering amplitudes. A least square fit in R-space of the k^2-weighted Fourier Transformation (FT) was used to obtain the EXAFS parameters. The Debye-Waller factor ($\Delta\sigma^2$) was unchanged for all fits. Approximately 35 mg of sample were pressed into a six-well, cylindrical sample holder, forming self-supporting wafers. For spectrum acquisition, the sample holder was placed in a quartz tube (1-in. OD, 10-in. length) sealed with Kapton windows by two Ultra-Torr fittings and, in turn, housed in a ceramic tube furnace. Ball valves were welded to each Ultra-Torr fitting and functioned as the gas inlet and outlet. The temperature of the catalyst sample holder was monitored by an Omega K-type thermocouple. A Matheson PUR-Gas Triple Purifier Cartridge was used to remove the oxygen and moisture in gas inlet. Samples were reduced at 3.5% H_2/He at 473K and cooled to room temperature for measurement under 3.5% H_2/He.

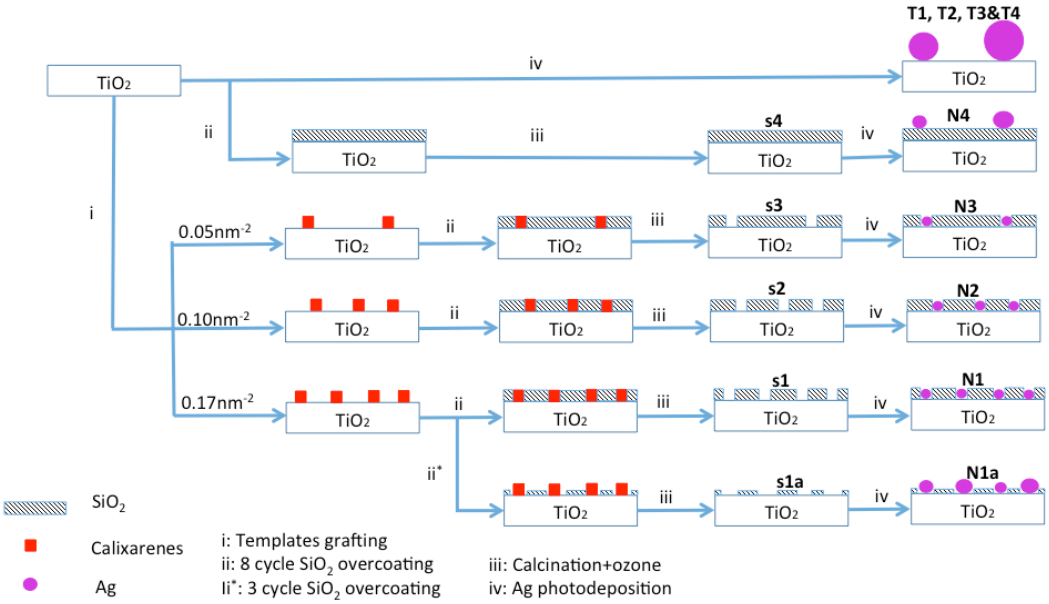

Scheme 2.2.1. Preparation of supports and subsequent photodeposition of Ag nanoparticles. (i) Deposition of 0.17 (S1), 0.10 (S2), or 0.05 (S3) calixarene.nm^{-2} from toluene at reflux. (ii) Deposition of 3 cycles (S1a) or 8 cycles SiO_2 (S1, S2, S3, S4). (iii) Thermal and ozone treatments. (iv) Photodeposition of Ag. Samples T1-T4 varied the deposition conditions; see text. Samples N1-N4 used a 30 s deposition time and 0.5 mM $AgNO_3$ solutions.

2.3 Results and Discussion

Support Preparation

Some of us have previously developed a method to create 1-2 nm diameter voids by grafting calixarene and other templates onto TiO_2, followed by deposition of Al_2O_3 by atomic layer deposition (ALD) and template removal, with analogy to materials S1-S3 of Scheme 1.[68] These thin, void-containing Al_2O_3 layers acted as a size-selective sieving layer on the surface of a photocatalytically active TiO_2 particle, which was capable of selectively oxidizing or reducing the smaller of two alcohols or nitroarenes in a mixture.[68]

Here, the use of a molecular template is similarly intended to ensure that SiO_2 deposition does not completely cover the TiO_2 surface. While the materials in this manuscript might also be produced from partial overcoating of TiO_2 with Al_2O_3 by templated ALD, the use of wet-chemical deposition of TEOS enables this method to be used widely, without the need for specialized equipment or air-sensitive reagents. Figure 2.3.1 a) shows that 8 cycles of TEOS deposition followed by heat treatment at 325°C for 1h gives ~2 nm conformal overcoats by TEM, or ~0.2 nm of SiO_2 deposition per cycle. Some of us have previously used benzyl alcohol photooxidation as a probe reaction for accessible TiO_2 surfaces.[67] Figure 2b) shows that after 8 cycles of SiO_2 deposition, the initial rate of benzyl alcohol photoxidation decreases to less than 1 % of the value on bare TiO_2. Thus, 8 cycles of SiO_2 deposition was taken as the base case to completely block off the TiO_2 surface, except for areas uncovered by template removal.

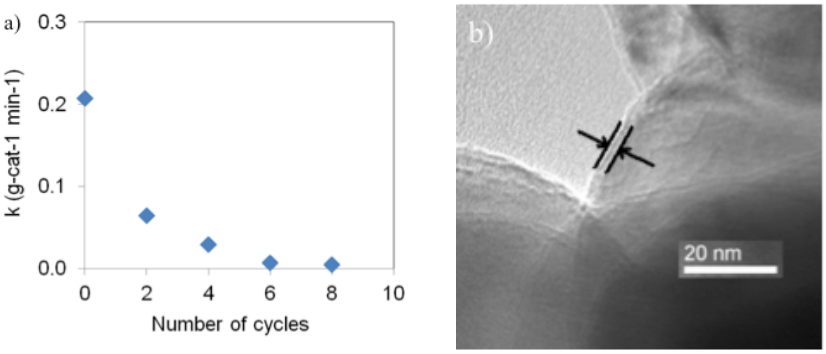

Figure 2.3.1. a) Photooxidation rate of Benzyl alcohol versus number of cycles of SiO2 overcoat is shown over TiO2 samples with 0-8 cycles of SiO2 overcoat, b) TEM image of TiO2 (Anatase, Sigma Aldrich, 12.5m^2/g) coated with 8 cycles of SiO_2.

Calixarene-TiO_2 materials were synthesized at surface densities of ~0.17 nm^{-2} (S1), 0.10 nm^{-2} (S2) and ~0.05 nm^{-2} (S3). As given in the experimental, surface densities are average values derived from molar loadings and the specific surface areas of the supports. See Figure 2.3.2 for TGA curves used to calculate these loadings. Using a simplified assumption of a cylindrical footprint, the templates cover approximately 50%, 30% and 15% of the TiO_2 surface, respectively. These values are taken as the number densities of exposed domains, and the total fraction of exposed TiO_2,[68] that are expected after SiO_2 deposition and oxidative template removal. Equating the template number density to the number density of exposed domains requires the assumption that individual template molecules are well dispersed and are evenly surrounded by the SiO_2 overcoat. Direct observation of the templates or the resulting uncovered domains remains a challenge, but prior evidence from synchrotron SAXS suggested domain sizes comparable to template dimensions.[68] Moreover, the marked difference in the behavior of deposited Ag nanoparticles, discussed later, itself argues against the presence of large domains of uncovered TiO_2, as would arise from substantial clustering of the original template molecules. Looking ahead in the manuscript, Figures 8 show that the 8 cycles of SiO_2 deposition used for materials S1-S3 resulted in SiO_2 layers of similar thickness as for deposition on bare TiO_2. Calixarene templates were removed by heating to 325°C in air, followed by O_3 treatment. UV-visible spectroscopy (Figure 2.3.3) shows that the calixarene-TiO_2 materials with and without SiO_2 overcoating have calixarene-based LMCT features above 400 nm, while the heat treated materials (S1-S4) only absorb below 400 nm and are indistinguishable from TiO_2, indicating effective removal of calixarene molecules on the TiO_2 surface after ozone and calcination procedures.

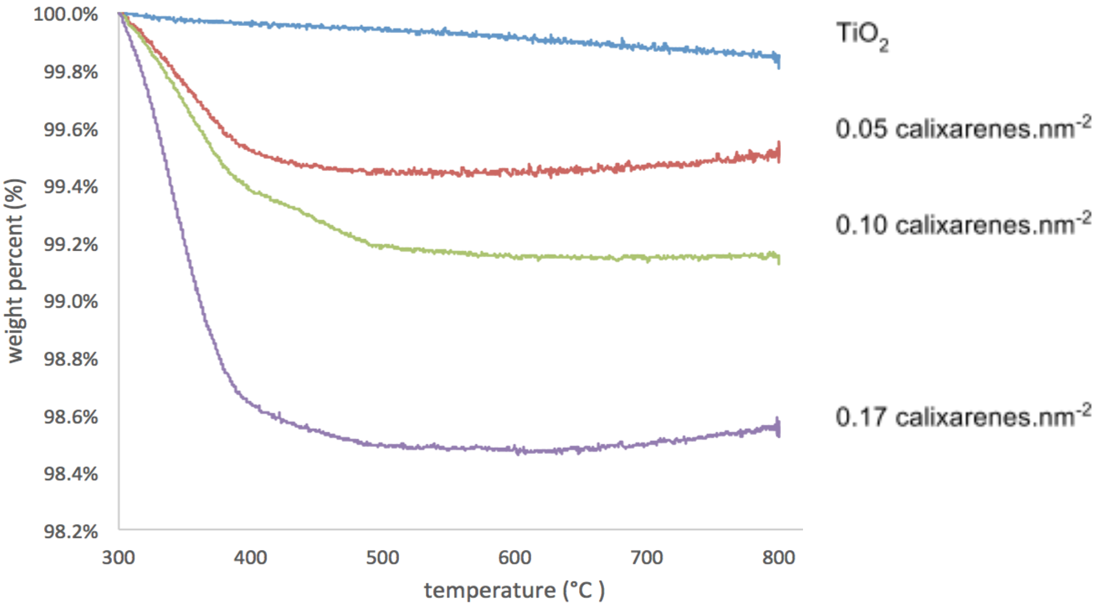

Figure 2.3.2. Thermogravimetric analyses for unmodified TiO_2, and TiO_2 grafted with three loadings of calixarene in the synthesis solution. From the mass losses, there are 0.05, 0.10 and 0.17 calixarenes per nm^2 of TiO_2 surface.

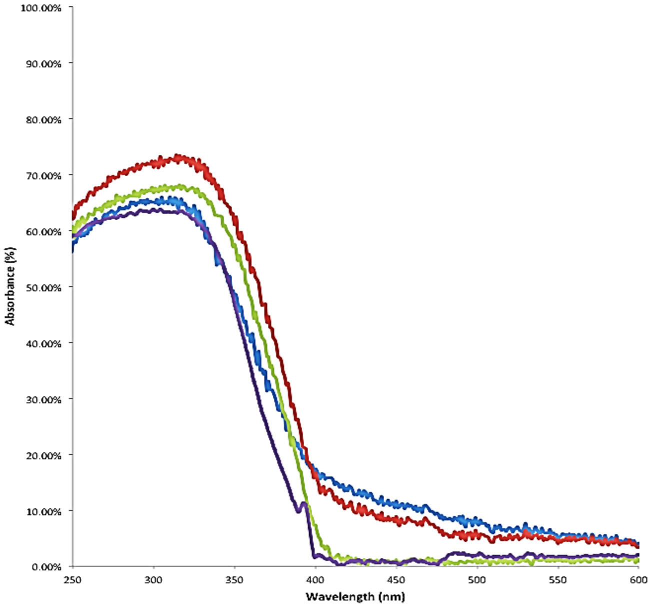

Figure 2.3.3. Kubelka-munk pseudo-absorbance for UV-visible spectroscopy of 0.17 calixarene.nm^{-2} on TiO_2, (blue), and 8 cycles of SiO_2 on the same sample (red), showing characteristic ligand-to-metal charge transfer bands above 400 nm, derived from calixarene-TiO_2 interactions. These bands are removed in the heat-treated material S1 (green) to give a spectrum indistinguishable from bare TiO_2 (purple).

The bare TiO_2 has a BET surface area of 71 m^2/g, while materials S4 and S1 have BET surface areas of 75 m^2/g and 86 m^2/g, respectively. While no significant changes are observed in the pore size distribution (BJH) of larger pores, the micropore volume of the materials is 0 cm^3/g, $17x10^{-4}$ cm^3/g, and $86x10^{-4}$ cm^3/g for the bare TiO_2, support S4 and support S1. Similarly, the micropore surface areas increase from 0 to 4 to 17 m^2/g (t-plot; see Figures 2.3.4 and 2.3.5). SiO_2 overcoating of TiO_2 without a template results in no significant change to the surface area or micropore volume, within measurement uncertainity, while the use of a template increases both metrics.

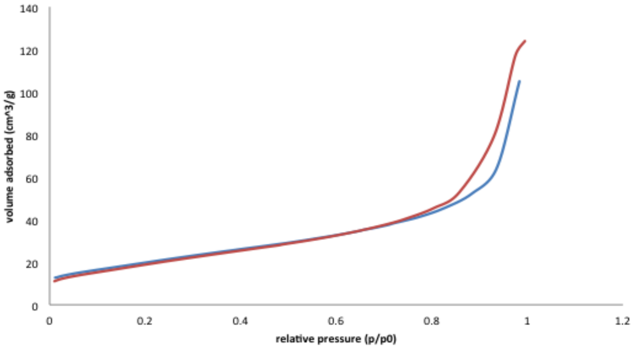

TiO_2:

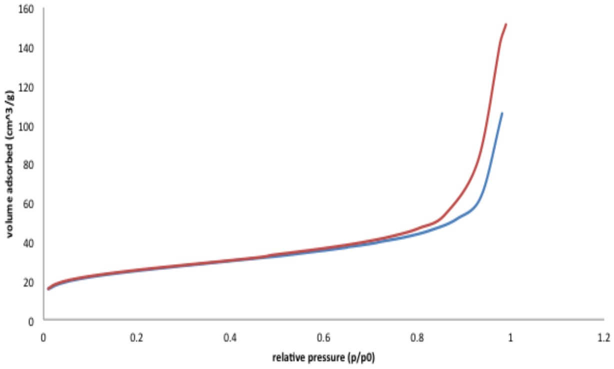

S1:

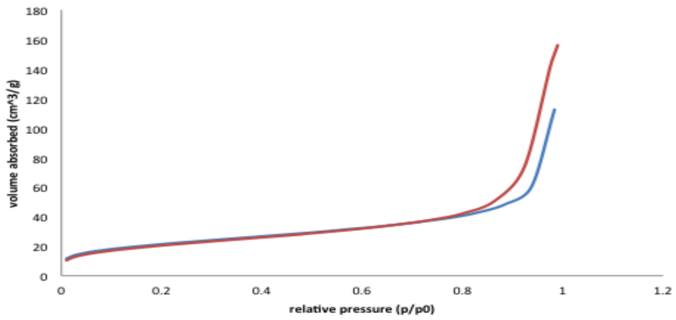

S4:

Figure 2.3.4. N_2 physisorption isotherms for representative supports. The increase in micropore surface area and volume for support S1 (see main text) is evident from its larger N_2 uptake at the lowest pressures.

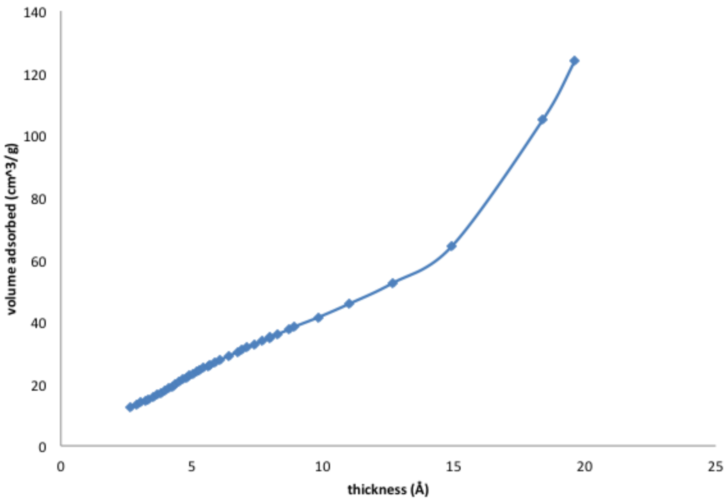

TiO_2:

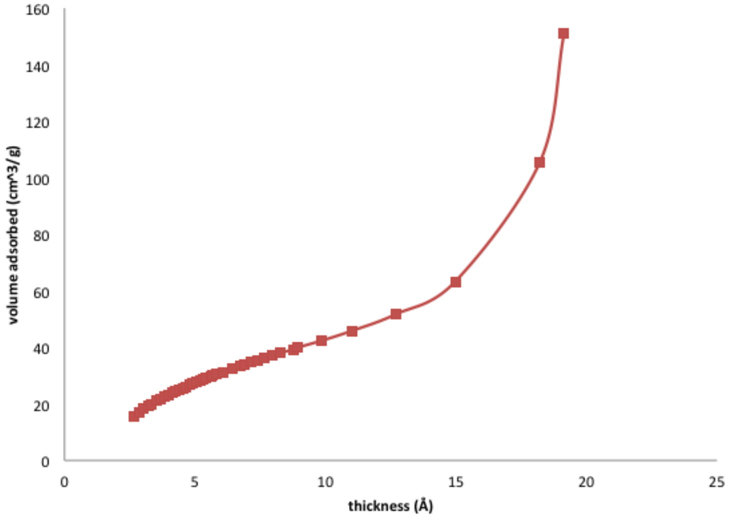

S1:

S4:

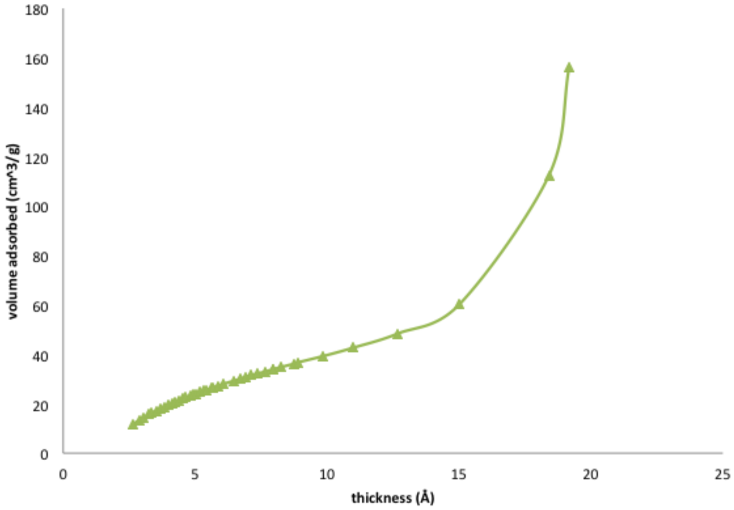

Figure 2.3.5. T-plots from N2 physisorption on unmodified TiO_2, and supports S1 and S4.

Conditions for Ag photodeposition onto TiO_2

Preliminary experiments were first conducted to study selectivity of the photodeposition method and the effect of UV illumination time and $AgNO_3$ concentration on the size of Ag nanoparticles deposited on bare TiO_2. TEM shows that well-dispersed, small Ag nanoparticles were generated on TiO_2 (Figure 2.3.6 a-d), while attempted deposition on SiO_2 resulted only in very large particles of Ag (>20 nm, Figure 2.3.6 e). Since SiO_2 is not a photoactive oxide like TiO_2, the primary mechanism for nanoparticle formation is non-catalytic nucleation in solution, as suggested by a previous study.[69] Continued Ag reduction then preferentially occurs on those few nuclei. Therefore, photodeposition is shown to be feasible for selectively generating Ag nanoparticles onto exposed TiO_2 domains, but not on the SiO_2 overcoat. Table 2.3.1 shows that increasing UV illumination time generally increases total Ag loading, Ag nanoparticle size, and the breadth of the particle size distribution. The increase in breadth of the particle size distribution is particularly significant. The loadings and number-average sizes of materials

T1 and T2 are the same within error, but the volume- average size of the latter is significantly larger, indicating the continued growth of a small number of larger particles. Unsurprisingly, decreasing the $AgNO_3$ concentration decreases the Ag nanoparticle size and size distribution, at the expense of loading, as is typically the case for metal deposition.

To generate reasonable Ag loadings, an illumination time of 30 s and 0.5 mM $AgNO_3$ (1.0 wt%, material T2) was selected as the base case for further experimentation. We note that photodeposition in general gives nanoparticle sizes and dispersions comparable to more established synthesis for small, well-dispersed nanoparticles, such as incipient wetness impregnation (Figure 2.3.6 f).

Table 2.3.1 Properties of Ag photodeposited on TiO_2.

Samples	AgNO3 concentration (mM)	UV illumination time (s)	TEM particle size by number average (nm)	TEM particle size by volume average (nm)	Ag loading (%)
1a	0.5	30	4.7 ± 2.7	9.8	1.00%
TiO2_2	0.5	5	5.1±1.8	7.4	1.10%
TiO2_3	0.5	120	7.1±3.3	13.4	3.00%
TiO2_4	0.006	30	2.4±0.6	2.8	0.40%

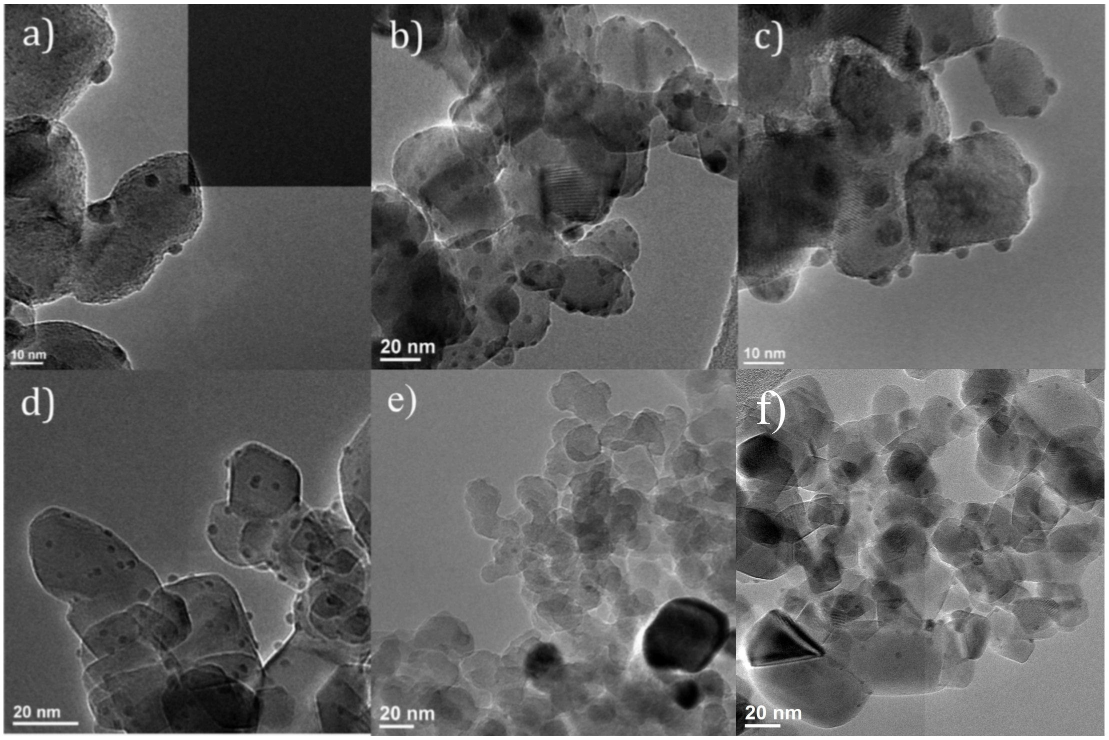

Figure 2.3.6. Representative TEM images of a) sample T1; b) sample T2 c) sample T3 and d) sample T4; the synthesis conditions for each sample is listed in Table 1, e) Ag photoreduced on SiO_2 and f) Ag wetness impregnated onto SiO_2.

Selective Ag Photodeposition

Using the chosen base-case conditions of reference sample T2, Ag was photoreduced onto the modified TiO_2 materials. Representative images are shown in Figure 2.3.7 and a summary of results is given in Table 2.3.2. Ag particle size distributions for each sample are listed in Figure 2.3.8. Ag-containing materials N1, N2, and N3, derived from supports S1, S2, and S3 all have number-average particle diameters less than 3.5 nm, while reference material T2 had an average diameter of 4.7 nm. Perhaps more importantly, the Ag size distributions on N1, N2, and N3 are all significantly narrower than that of the reference T2, and as such, the volume average nanoparticle sizes of N1, N2, N3 are significantly smaller than that of T2. Ag loadings for samples N1, N2, and N3 are all ~50% higher than on T2, making the improved nanoparticle size distributions all the more remarkable. These results indicate that the SiO_2 overcoats are able to effectively control nanoparticle sizes while actually enhancing Ag photodeposition.

Table 2.3.2. Properties of Ag photodeposited on SiO_2-TiO_2.

Sample	TEM particle diameter (nm)		EXAFS analysis		Ag (wt%)[a]	average particle separation (nm)[b]	average template separation (nm)[c]
	number average	volume average	coordination number[a]	particle size (nm)[a]			
T2	4.7 ± 2.7	9.8	10.8	7±1	1.0%	74	n/a
sT2[d]	n/d	n/d	11.6	>9	1.0%	n/d	n/a
N1	2.9 ± 0.6	3.5	9.6	5±1	1.5%	30	2
sN1	3.3 ± 0.7	3.8	8.7	4±0.5	1.5%	36	2
N2	3.5 ± 0.8	4.1	n/d	n/d	1.7%	37	3
N3	3.4 ± 0.6	3.8	n/d	n/d	1.6%	36	4
N4	3.8 ± 1.0	5.1	8.0	3±0.5	1.5%	44	n/a
sN4	3.9 ± 0.9	4.5	8.9	4±0.5	1.5%	46	n/a
N1a	2.6 ± 1.9	7.8	n/d	n/d	1.3%	27	2

[a] Fitted Ag-Ag coordination number and ICP-AES have approx. 10% uncertainty. Particle sizes from EXAFS calculated from Ag-Ag coordination numbers, with uncertainty consistent with previous reports.[39]

[b], $(Dp)^{-1/2}$, where Dp = average Ag nanoparticles per nm^2, calculated from the Ag wt% and the number-average particle size. The Ag density within a nanoparticle is assumed, for these purposes, not to deviate from the bulk value.

[c], $(Dt)^{-1/2}$, where Dt = template surface density, calculated from TGA as given in the experimental.

[b] Less than 10 Ag nanoparticles observed. Severe aggregation.

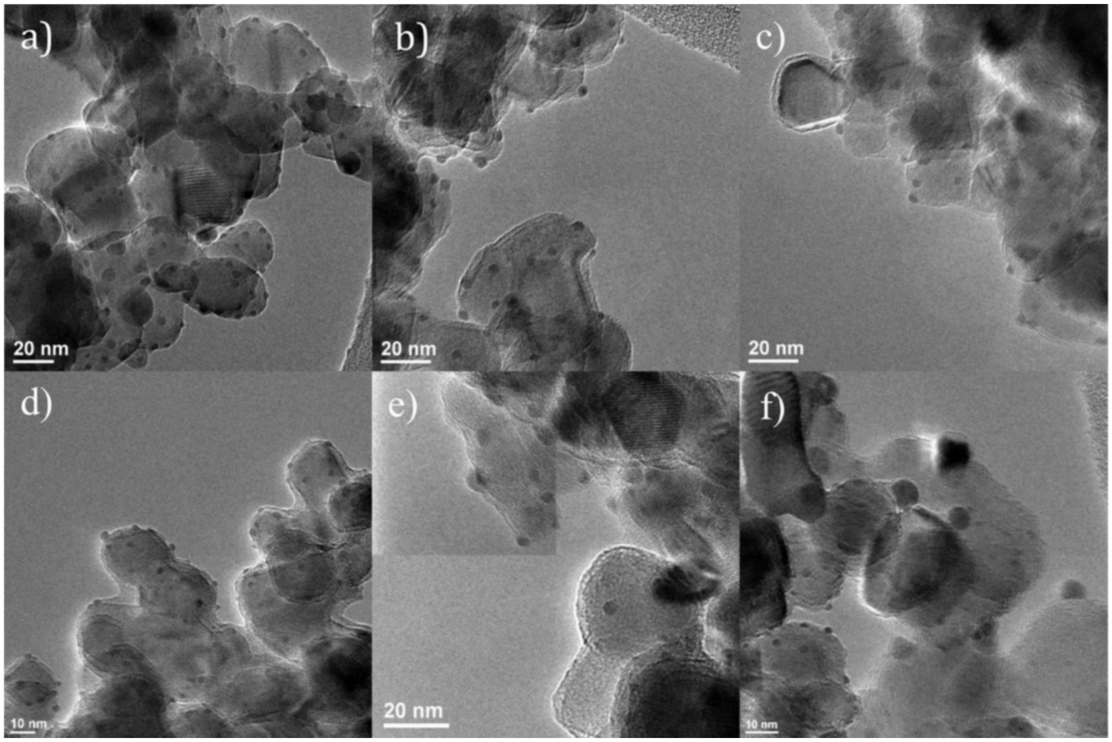

Figure 2.3.7. Representative TEM images of (a) sample T2, (b) sample N3, (c) sample N2, (d) sample N1, (e) sample N4, and (f) sample N1a.

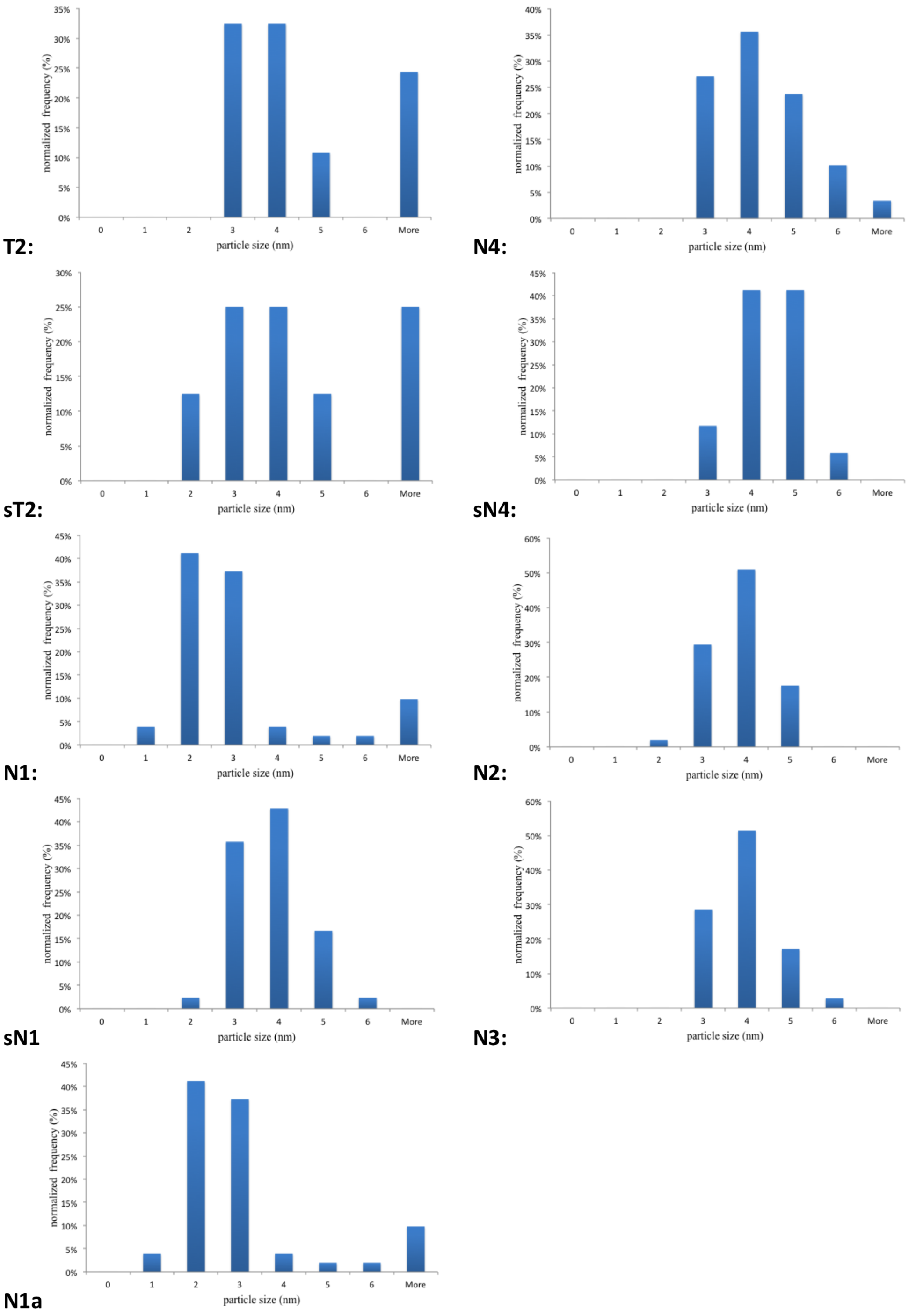

Figure 2.3.8. Binned nanoparticle diameter distributions for the materials in this study. Note the substantial decrease in large nanoparticles when using the partial overcoat method, especially after a sintering treatment.

Two interesting corollaries to these experiments are the nanoparticle size distributions for materials N1a and N4 derived from support S1a and S4, which used 0.17 templates.nm^{-2} with 3 cycles SiO_2, and no template with 8 cycles SiO_2, respectively. Support S4 behaved comparable to the supports with the template. In contrast, support S1a, which used a thinner SiO_2 layer known to not completely mask the surface, gave a lower Ag loading than for the other overcoated materials and much worse control over Ag nanoparticle sizes. While the number-average nanoparticle size was quite good, the distribution was large, resulting in a large volume-average Ag nanoparticle size. Overall, the amount of deposited SiO_2 appears to be more important than the template density. Insufficient coating with SiO_2 likely leaves large patches of TiO_2 exposed, leading to poor nanoparticle control. In contrast, both molecular templates and pinhole defects in a dense, but still relatively thin, SiO_2 overcoat helps limit the space available for Ag nanoparticle growth.

EXAFS analysis of Ag nanoparticle sizes (Table 2.3.2) was also carried out on representative materials N1, N4, and T2. Because average particle sizes derived from EXAFS report on all Ag atoms in a sample, deviations from the TEM estimates (volume-average sizes) can indicate the existence of either many very small (<1 nm) or a few large Ag nanoparticles that may be missed in microscopy. Size distributions from the two techniques are equal within error for materials N1 and T2, but the EXAFS-estimated particle sizes for material N4 are lower than the values obtained from TEM, corroborating the hypothesis above that very small nanoparticles may be nucleating in pinhole cracks in the SiO_2 overcoat of this material.

Examining the data in Table 2.3.2 shows a trend of Ag loading increasing with the amount of SiO_2 deposition, either from increased cycles or amounts of added template. This suggests that Ag loading is controlled by adsorption of Ag^+ on the SiO_2 surface. It has been previously reported that SiO_2 coating on TiO_2 leads to improved suspension of TiO_2 in water and improves adsorption of molecules.[38] The latter should be particularly pronounced for the adsorption of positive Ag^+ on the negatively-charged SiO_2 surfaces. Table 2.3.2 also shows that the average spacing between nanoparticles is much greater than that of the added template molecules. While Ag^+ adsorption may be generally enhanced by the entire SiO_2 surface, it appears that nucleation of Ag nanoparticles occurs at <1% of the exposed TiO_2 domains.

Observations of Sintering Behaviors

The thermal stability of Ag nanoparticles on T2, N1, N4, and control samples of Ag/TiO_2 prepared by incipient wetness impregnation was tested by heating to 450°C for 3 h in He. See representative TEM images in Figure 2.3.9. For sample sT2, Ag on bare TiO_2, very few, very large Ag particles (>10 nm) were observed by TEM (Table 2.3.2) after the heat treatment. Likewise, Ag/TiO_2 by incipient wetness impregnation resulted in severe aggregation by TEM (Figure 2.3.9). In contrast, samples sN1 and sN4 derived from photodeposition on SiO_2-overcoated materials, gave Ag nanoparticle sizes that remained under 5 nm and particle size distributions unchanged within uncertainty from the as-synthesized samples.

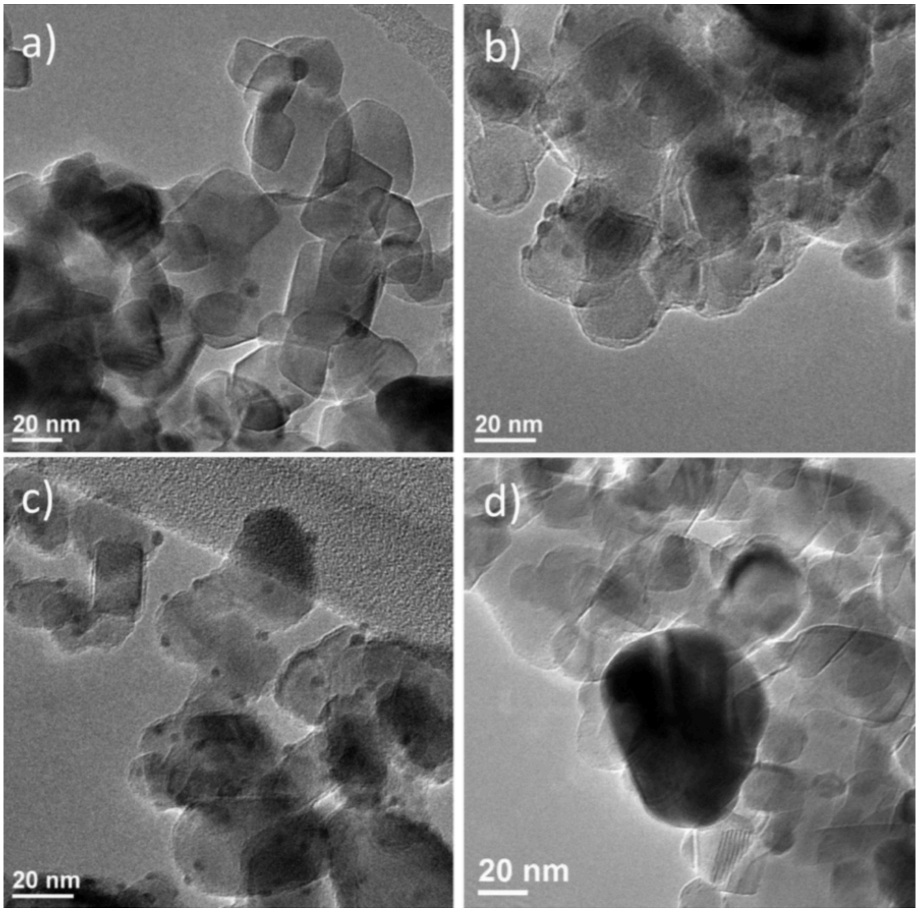

Figure 2.3.9. Representative TEM images of heat-treated samples: (a) sT2, (b) sN4, (c) sN1, and (d) control Ag/TiO_2 from incipient wetness impregnation.

EXAFS is especially useful as a corroborating technique here since the small number of Ag nanoparticles in sample sT2 did not allow meaningful size distributions to be calculated. EXAFS analysis confirms that the majority of the Ag atoms in sT2 are present in large particles, with a fitted Ag-Ag coordination number of 11.6 approaching the limit of 12.0 for bulk metal. Correlations between coordination number and nanoparticle size break down at this point,[70] but it is clear that the Ag nanoparticles are at least 9 nm in size. In contrast, samples N1 and N4 show no change in particle sizes with heat treatment beyond the uncertainties of the TEM and EXAFS analyses. Interestingly, sample sN4 uniquely showed a significant number of relatively large (>4 nm) Ag nanoparticles on the TEM grid instead of the oxide particle. These must have arisen from TEM sample preparation, but indicates that Ag nanoparticles are becoming detached from the SiO_2 surface during sintering of N4. No such behavior was observed for any other sample.

The inability to extract meaningful particle size distributions from the most heavily sintered samples sT2 and the control Ag/TiO_2 from incipient wetness impregnation limits our ability to speculate on the mechanisms of sintering and their prevention. However, materials N1 and N4 show no change in the particle size distribution after heat treatment, within uncertainty, which would seem to rule out Ostwald ripening as a significant contributor. Others have found that particle aggregation and coalescence played a major role in sintering behavior, and that it could be inhibited by barriers between metal nanoparticles. Analysis of particle-particle separation distributions, such as by electron tomography[25, 71], could be employed to support this.

Earlier experiments have also shown enhanced stability of related, but inverted systems. For example, Au deposited on small TiO_2 domains supported on SiO_2 showed resistance to Au aggregration[72]. It has also previously been demonstrated that overcoating SiO_2 onto pre-formed nanoparticles on TiO_2 improved their sintering resistance.[27] Both of these experimental approaches are quite distinct from ours, but mechanisms for enhanced stability may be shared. As proposed in these references, the SiO_2-TiO_2 interfaces surrounding the exposed TiO_2 domains are proposed to be strong binding sites for Ag nanoparticles. Ag nanoparticles interact weakly with the SiO_2 domains themselves, providing an energetic barrier that the Ag nanoparticles would need to cross in order for two particles to aggregate. This method of stabilization would suggest that Ag particles wholly or partially outside the TiO_2 domains would be relatively destabilized, leading to stabilization of those on the TiO_2 domains. In the limit, this could even result in re-dispersion of Ag nanoparticles onto empty TiO_2 domains with increasing temperature.

2.4 Conclusion and Future work

This work provides another example of the viability of using photoreduction to deposit small Ag nanoparticles on the surface of TiO_2. In general, TEM and EXAFS analyses demonstrate that photodeposition is a very rapid method to create relatively small (<10 nm) supported metal nanoparticles. Mere seconds are needed from start to finish, whereas hours are needed to equilibrate, calcine, and reduce catalysts synthesized by traditional methods. However, one must be aware of the possibility of photon attenuation and related effects during synthesis. Here, we minimize these effects by the use of effective stirring and dilute suspensions of a non-porous support, but this could complicate the scaleup of this methodology to industrial quantities. The deposition conditions used here may also not be optimized for other metals or support morphologies. The most significant fundamental limitation of photodeposition of Ag is a rapid increase in the breadth of the particle size distribution with increasing illumination time, which may in part be due to enhanced rates of reduction at the metal, as opposed to the TiO_2 surface,[73] or to plasmon resonance enhancement at the developing nanoparticles.[74] These materials are not stable with respect to sintering at high temperature, but this is a trait shared by all such metal nanoparticles supported on TiO_2.

This work further demonstrates the novel use of SiO_2 overcoats to control the Ag nanoparticle size to the range most useful for catalysts (<5 nm) and to impart thermal stability. First, a simple, wet-chemical method is demonstrated to generate conformal, thin (~2nm) SiO_2 overcoats with coverage easily controlled by the number of SiO2 deposition cycles. While some of the authors cited here use relatively thin shells,[43] many encapsulation methods generate much thicker oxide shells or isolate a single metal nanoparticle in each oxide shell.[32] We show that Ag photodeposited on a full SiO_2 shell over TiO_2 helps limit the size of the resulting Ag nanoparticles, but we also observed that these particles are easily detached from the surface after thermal treatments. In contrast, partial SiO_2 overcoats made possible by use of a molecular template, result in smaller Ag nanoparticles, a narrower particle size distribution, and resistance against thermal sintering. The number of cycles of SiO_2 coating is seen to be important in controlling the Ag nanoparticle size distribution, with less control afforded if less SiO_2 is added than would be required to completely fill the residual TiO_2 surface between templates. As was introduced above, direct observation of the templates or the resulting partially-exposed oxide domains remains challenging, but the unique success of materials like N1 in stabilizing Ag nanoparticles is itself consistent with our picture of the templating and oxide overcoating process.

Overall, a new catalyst synthesis strategy is proposed, which consists of first, applying a partial inert oxide overcoat on existing oxide support and second, backfilling with metal nanoparticles. This has been shown to both control growth the initial synthesis of metal particles and to enhance their thermal stability. This method of nanoparticle stabilization does not require a physical blocking of the Ag surface, eliminating the potential for diffusional limitations when working in the condensed phase with larger molecules or a loss in active surface area, as could be present in other methods of stabilization via encapsulation. Additional experiments are underway to understand the mechanisms of size control and to further expand the scope of this synthesis technique.

The facile photodeposition of Ag onto TiO_2 also finds use in developing the antimicrobial glass coating. Collaborators in Prof. Kim Gray's lab at Northwestern University have demonstrated that the Ag loaded TiO_2 (Anatase 100 nm) preserves the bacteria killing capability even without UV illumination. Figure 2.3.10. shows the bacteria killing percentage with and without UV illumination. Under UV illumination, Ag loaded TiO_2 (AA100) shows 54% Ecoli killing in 30 minutes, which is comparable to the bacteria killing performance of pure anatase TiO_2 (25 nm or 100 nm). In dark condition, while other coatings show negligible bacteria killing performance, the Ag loaded TiO_2 (AA100) still have 41% Ecoli bacteria killed.

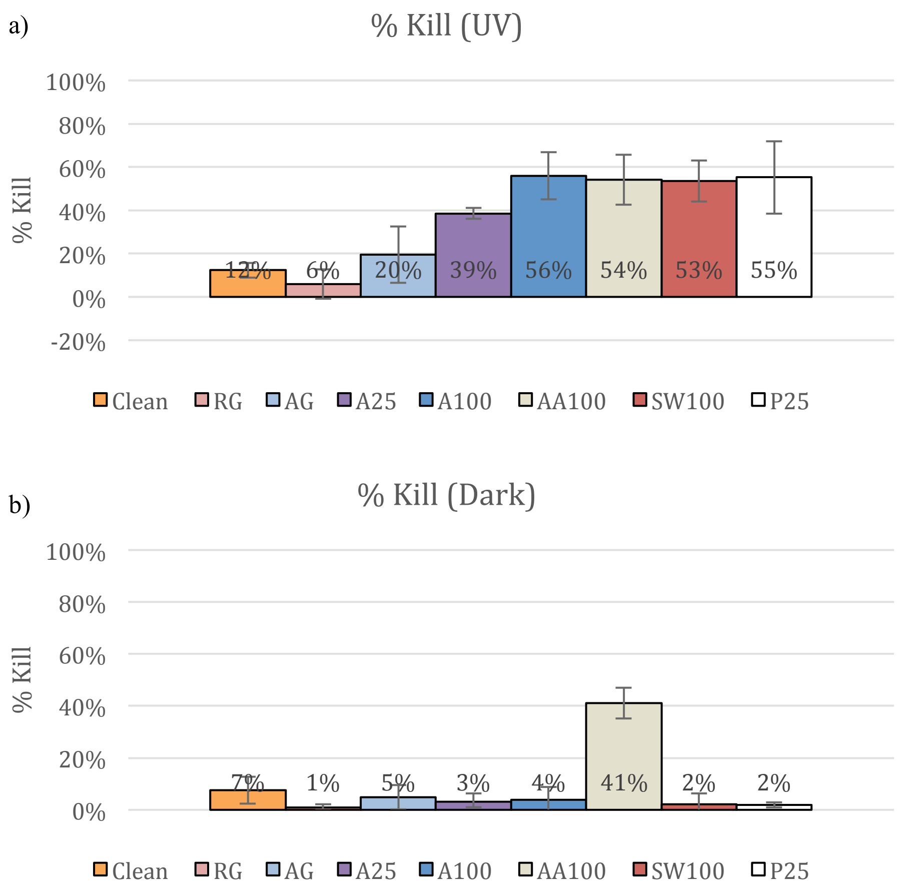

Figure 2.3.10. Bacteria killing performance of different TiO_2 materials a) under UV illumination, b) in dark, samples (**Clean**: sample without cleaning, **RG**: regular Gorilla glass, **AG**: anti-microbial glass, **A25**: Anatase 25 nm, **A100**: Anatase 100 nm, **AA100**: Ag-Anatase 100, **SW100**: Single Wall Carbon Nanotubes loaded Anatase 100 nm).

Bacteria killing experiment: A microscope slide coated with TiO_2 was placed in a small petri-dish filled with a bacterial suspension (10^8 CFU/ml, the Ecoli ATCC 25922 bacterial). The small petri-dish was covered with UV transparent film to minimize the evaporation. The covered petri-dish was shaken at 300 rpm while exposing to the UV light for 30 minutes. After reaction, the Baclight reagents were added into the suspension and the mixture was incubated for 20 seconds in the dark. Afterwards, the coverslip was mounted on a slide and the fluorescence images were recorded using a microscope. Finally the number of bacteria in the image was quantified using Matlab.

Chapter 3

Wetness Impregnation of Pt onto SiO_2 Partially Overcoated TiO_2

3.1 Introduction

Here, we report a scalable, wet-chemistry synthesis method to generate metal catalysts with enhanced thermal stability using supported Pt/TiO_2 as a sample system. Supported Pt catalysts are workhorse catalysts in applications including water-gas shift,[75],[76] aromatics hydrogenation,[77],[78],[79] and the oxygen reduction reaction in fuel cells.[80],[81] TiO_2 particles were first overcoated with a thin SiO_2 layer (<2 nm) using an optimized Stöber method based on our group's previously reported procedure[82] , and then used as supports for synthesizing Pt catalysts by wetness impregnation of H_2PtCl_6. Base-catalyzed sol-gel methods are widely used for large scale production of metal oxides,[83] [13]and wetness impregnation is one of the most commonly applied methods for the synthesis of supported metal catalysts.

We have previously reported on the size-controlled synthesis of Ag nanoparticles by exploiting photocatalytic deposition onto the exposed TiO_2 domains of a similar, partially-masked SiO_2-TiO_2 material. The current study is not nearly as restricted in scope, and demonstrates that conventional catalyst preparation methods (e.g. wetness impregnation) also result in improved metal dispersion. Both transmission electron microscopy (TEM) and CO chemisorption show that the size and stability of the supported Pt nanoparticles are tuned by the amount of the SiO_2 overcoat and whether an organic template is used to deliberately leave voids in the SiO_2 layer. We also demonstrate for the first time that the Pt nanoparticles supported on the modified TiO_2 preserve the specific activity of Pt on unmodified TiO_2 using an ethylene hydrogenation probe reaction. This reaction was run under deliberately coking conditions to demonstrate the accessibility of the Pt surface in the modified materials, and to probe the resistance of the nanoparticles to sintering under the conditions of catalyst regeneration.

3.2 Experiments

Catalyst preparation

Organic templates were grafted onto TiO_2 by adapting previously reported procedures.[82],[84],[68] TiO_2 (4 g, 20-30 nm primary crystallite size, ~71 m^2/g BET surface area, Degussa P25) was dried under dynamic vacuum overnight at 110 °C. Then, the TiO_2 was dispersed in a solution of p-*tert*-butylcalix[4]arene ('calixarene', 50 mg, $C_{44}H_{56}O_4$, Sigma Aldrich) in 200 ml toluene and heated to reflux overnight, then filtered, washed with 200 ml toluene and 200 ml hexane, and dried under dynamic vacuum.

TiO_2 was coated with SiO_2 using a modified version of the base-catalyzed sol-gel synthesis method some of us reported earlier.[82] TiO_2 (~1 g, modified or unmodified with calixarene) was dispersed in a solution of 182 mL ethanol (200proof) and 27 ml NH_4OH (28-30wt%) and sonicated for ~30 min. Then, 0.1 ml of tetraethyl orthosilicate (TEOS, 98%, reagent grade, Sigma Aldrich) was added, and the suspension was shaken for at least 1 hr. The cycles of sonication and TEOS addition were carried out a total of 1-4 times. Continuous, slow addition of TEOS could be a route to further optimization of the synthesis. After the final cycle, the coated material was filtered and treated under ozone (HG 1500 ozone generator, Ozone Solutions Inc.) at 110 °C for at least 3 hours to remove any surface organics or the template molecule. Although not done here, calcination in air could presumably also be used to remove the template, instead of ozone.

Pt was deposited onto TiO_2 supports using incipient wetness impregnation following previously reported procedures.[85] 0.8 g TiO_2 support was dried under dynamic vacuum at 110 °C overnight to remove surface water then impregnated with 2 ml aq. H_2PtCl_6 precursor (~40 mmol, water purified using a Barnstead Nanopure system) and agitated for 48hrs, then air dried for ~48 hours, calcined in air for 4 hours at 400 °C with a heating rate of 5 °C/min, then reduced in H_2 for 10 hours at 450 °C with a heating rate of 5 °C/min under He until the hold temperature was reached. Scheme 1 illustrates the steps to synthesize samples Pt/TiO_2, Pt/2C, Pt/2CT, Pt/4C and Pt/4CT, indicating two or four cycles ('C') of silica deposition, with or without templates ('T'). Some reduced samples were subjected to a second, extended calcination in air at 500 °C for 5 hours with heating rate of 10 °C/min to give samples Pt/TiO_2-S, Pt/2C-S, Pt/2CT-S, Pt/4C-S, Pt/4CT-S.

Scheme 3.2.1. Procedure for grafting templates, coating the supports, and depositing Pt[a]

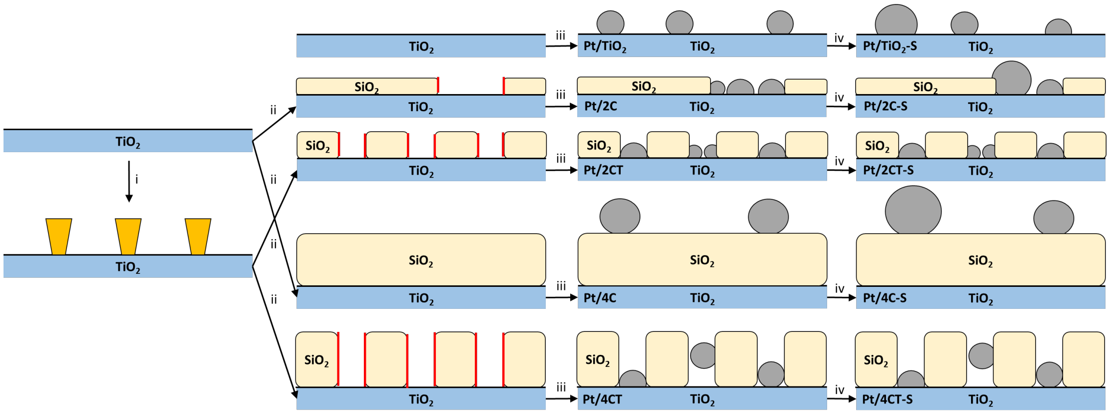

[a] Synthesis steps: i. Grafting calixarene template, ii. Overcoating support with SiO_2 by TEOS condensation, iii. Incipient wetness impregnation and reduction of H_2PtCl_6, iv. Additional heat treatment at 500 °C in air. Red lines indicate new surface area added by overcoat.

Catalysts Characterization

Samples were dried under dynamic vacuum at 110 °C overnight before N_2 physisorption using a Micrometrics ASAP 2010 with specific surface areas calculated using the Brunauer–Emmett–Teller (BET) method. Thermogravimetric analysis (TGA) was carried out using a TA Instruments Q500 under 90%/10% O_2/N_2. Mass loss between 300 °C and 800 °C is assigned to the combustion of the grafted calixarene template and used to calculate the template loading. Pt loading was determined using a Thermo iCap7600 ICP-OES with sample digestion in a mixture of HF and aqua regia (33 vol% of 70 wt% HNO_3 with 66 vol% of 37 wt% HCl, both Fisher Chemical Inc.). TEM was performed using a JEOL 2100 fast transmission electron microscope at 200 kV. TEM samples were prepared by dispersing the sample in ethanol, sonicating, then placing one drop on the grid and air-drying. Pulse CO chemisorption was performed using an AMI 200 chemisorption analyzer (Altamira Inc.). Samples were first loaded into a quartz U-tube, reduced in 5% H_2/Ar at 200 °C for 60 minutes, cooled to room temperature under He, then dosed 30 times with 5% CO/He to saturate the Pt surface. The effluent CO was monitored by a thermal conductivity detector (TCD) normalized to known CO flows, and the amount of chemisorbed CO was calculated from the sum of the differences in area between the early pulses and the pulses after saturation was reached. A CO:$Pt_{surface}$ of 1:1 was assumed, and the dispersion of Pt is the ratio of surface Pt to total Pt. Isoelectric point (IEP) measurements are completed by first suspending 15 mg of sample material in 15 mL H_2O (Barnstead Nanopure system) followed by sonication. After that, the pH of the mixture was adjusted using NH_4OH or HNO_3 and the mixture was shaken overnight at room temperature. The final pH for each mixture was measured followed by zeta potential measurement using a Zetasizer (Malvern Instrument

Ltd, Nano ZS). The zeta potential vs. pH curves for different samples were plotted to estimate the IEPs of each sample.

Catalyst examination

Ethylene hydrogenation used 25 mg total sample, consisting of a mixture of the catalyst and pure TiO_2 as a diluent. A control consisted of a 50 mg mixture of Pt/SiO_2 (0.5 wt%, Micromeritics) diluted with SiO_2. To maintain similar, differential conversion (<10%), the catalysts were diluted with TiO_2 at a mass ratio between 1:200 and 1:1600 at levels in proportion to their Pt dispersion. TiO_2 was used as diluent so that the same amount of TiO_2 was present in each catalyst bed in spite of the different dilution ratios required to maintain isoconversion. The catalyst bed was supported on quartz wool in a quartz tube reactor. The reactor was purged with argon at 25 °C for 5 min first to remove residual air. 3% ethylene (25 mL/min, Airgas, balance Ar), Ar (50 mL/min, Airgas, 99.999%) and 10% H_2 (50 mL/min, Airgas, balance Ar) were delivered using mass flow controllers (Altamira Instruments). The reactor was heated at 2.0 °C/min to 80 °C. In some cases, the catalyst was regenerated following a run by heating the reactor at ~12 °C/min to 450 °C in Ar (50 ml/min), then 10% O_2/He (50 ml/min) for 2 hours at 450 °C, and finally cooling down the reactor to 80 °C in Ar (50 ml/min). Products were identified and quantified online by an Agilent 7890A GC system equipped with a flame ionization detector (FID) using a GS-GasPro column (30m x 60 mm x 0.32 μm). Data were collected every 4 minutes for up to 15 hours time-on-stream. Ethane and unreacted ethylene were the only species observed and the mass balance for all runs exceeded 90%.

3.3 Results and Discussion

Characterization of support structure

The morphology of the oxide support was examined as a function of 1-4 cycles of SiO_2 overcoating and added template. As determined by TGA (Figure 3.3.1), calixarene-TiO_2 materials possessed a template surface density of ~0.16 nm^{-2}. Given a calixarene cross-sectional area of ~1.5 nm^2, the template molecules cover approximately half the support surface, in accordance with maximum grafting density observed elsewhere.[82,68] We previously demonstrated the use of different molecules to template the surface and selectively expose the TiO_2 support surface after second oxide deposition.[68] Depending on the application, other templates may have a more appropriate size or handling characteristics. Cost is likely to be a relatively minor issue due to the low loadings of the template used (~1 wt% vs TiO_2).

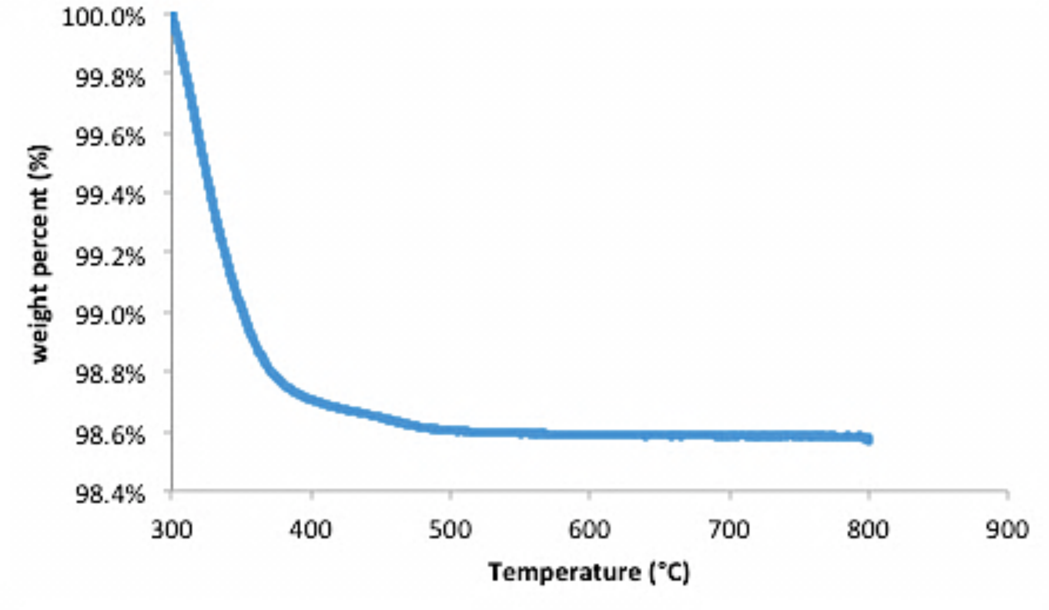

Figure 3.3.1. TGA curve for mass loss of calixarene loaded TiO_2 between 300 °C and 800 °C.

Under the conditions described in the experimental, SiO_2 deposition is conformal around each TiO_2 particle. Figure 3.3.2a is a representative TEM of material 4C, which shows that 4 cycles of SiO_2 deposition (total of 2.5 mmol TEOS added per g TiO_2, or ~5 Si atoms per original Ti-OH group) generates a ~1-2 nm conformal coat on TiO_2 surfaces without added template molecules. No separate amorphous SiO_2 domains are observed in the TEM images.

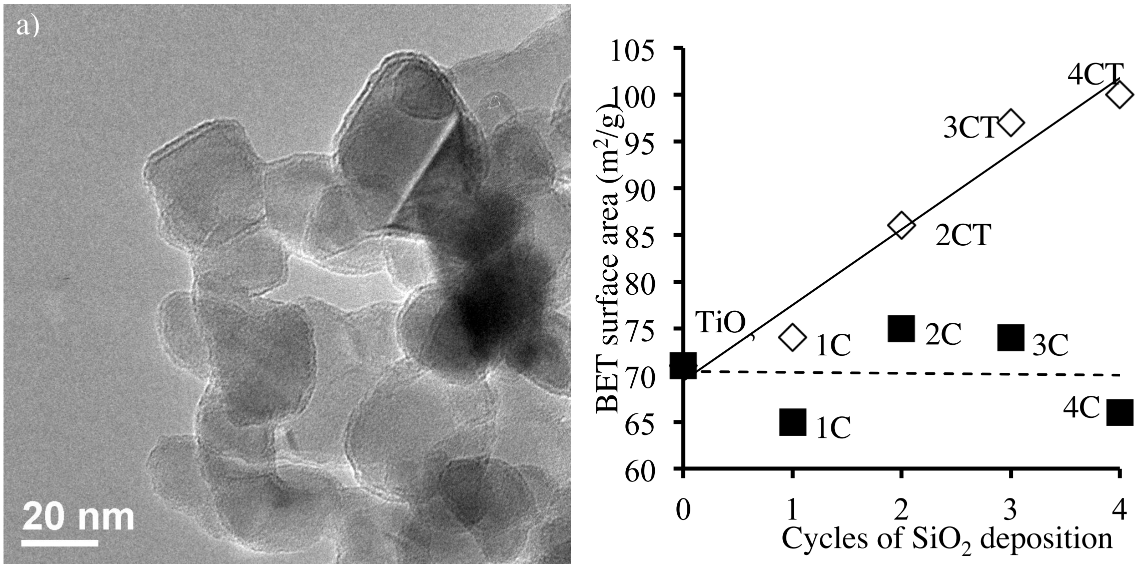

Figure 3.3.2. a) TEM image of TiO_2 surface after 4 cycles of SiO_2 deposition illustrates a 1.6 nm, uniform SiO_2 coat generated by controlled deposition of TEOS. b) Plot shows support BET surface area as a function of the number of SiO_2 overcoating cycles, with templates (◊) and without templates (■).

Figure 3.3.2b shows the relationship between the BET surface area of the modified supports and cycles of SiO_2 overcoating. N_2 adsorption isotherms are included in Figure 3.3.3. In the absence of added template, the BET surface area does not increase significantly or systematically between 1 and 4 cycles (up to 2.5 mmol TEOS/g TiO_2), as expected for thin conformal coats on a non-porous particle. In contrast, the BET surface area continuously increases from 71 m^2/g (unmodified TiO_2) to 100 m^2/g (sample 4CT) when 4 cycles of SiO_2 are deposited on the template-modified TiO_2 support. The differences observed in BET surface area lead to the conclusion that the templates on the TiO_2 surface help create defects in the overcoat, as intended. These defects expose the underlying TiO_2 as well as additional SiO_2, consistent with our previous findings.[82] This additional surface area is marked in red in Scheme 3.3.1. In addition to BET plots, isoelectric point measurements of supports TiO_2, 2C and 4C (Figure 3.3.4) show a decreasing isoelectric point with increasing amounts of SiO_2 deposition, indicating that increasing amounts of the total surface of the material are SiO_2, rather than TiO_2.

a) N_2 adsorption and desorption isotherm of TiO_2

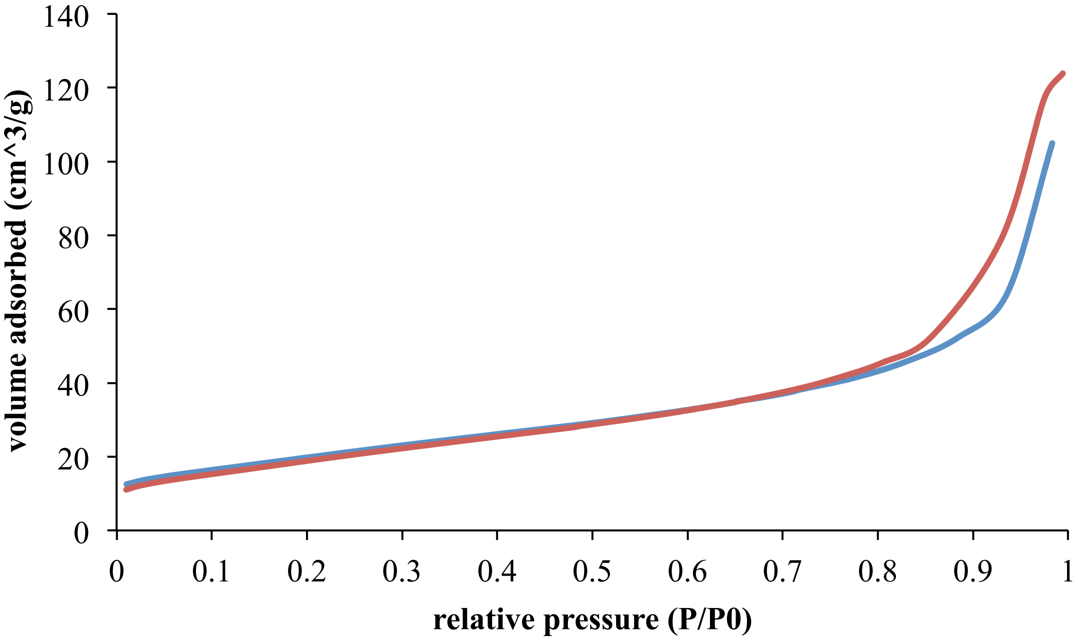

b) N_2 adsorption and desorption isotherm of material 1C

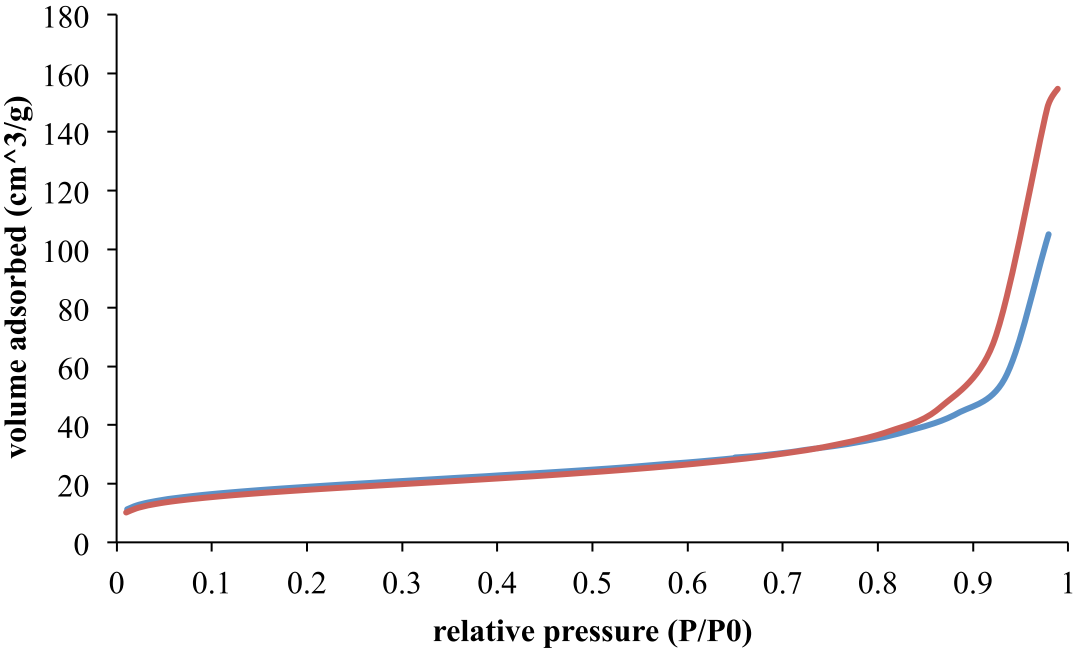

c) N_2 adsorption and desorption isotherm of material 1CT

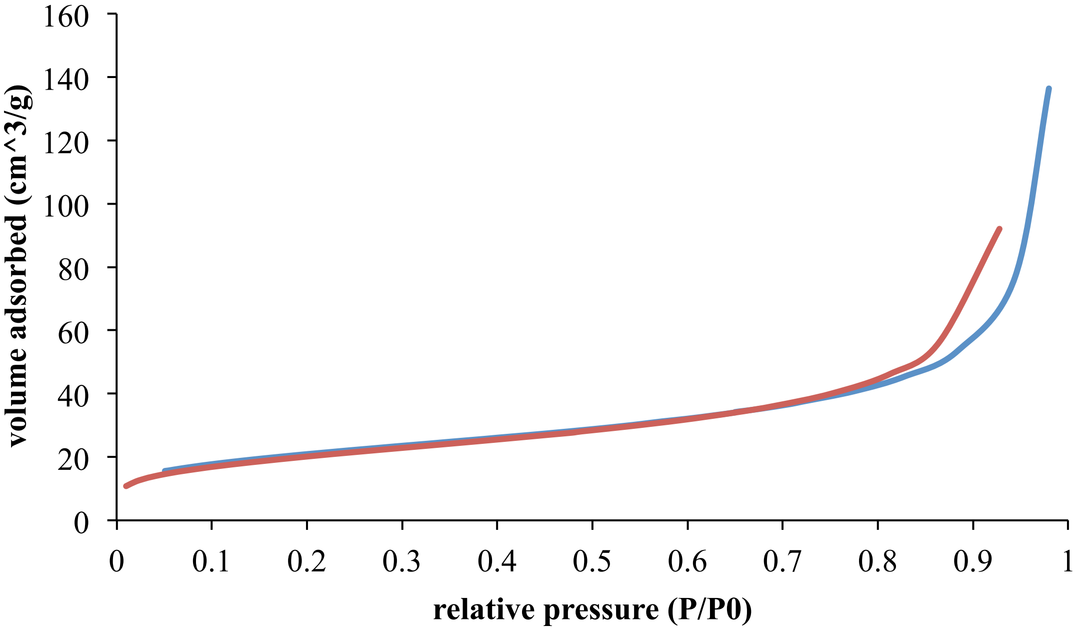

d) N_2 adsorption and desorption isotherm of material 2C

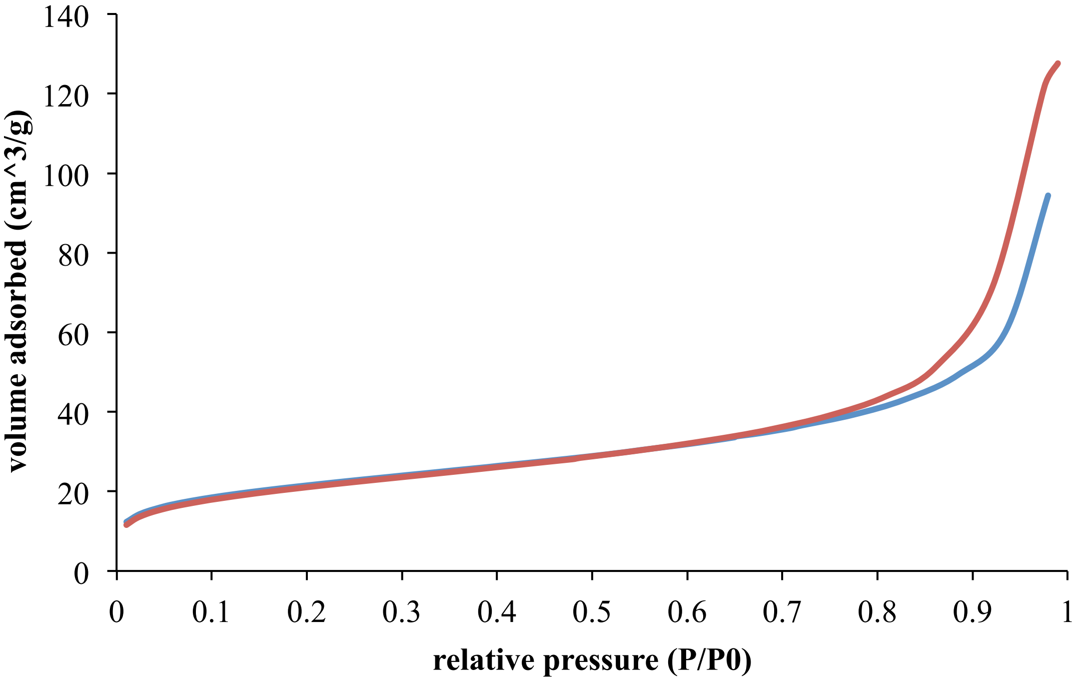

e) N_2 adsorption and desorption isotherm of material 2CT

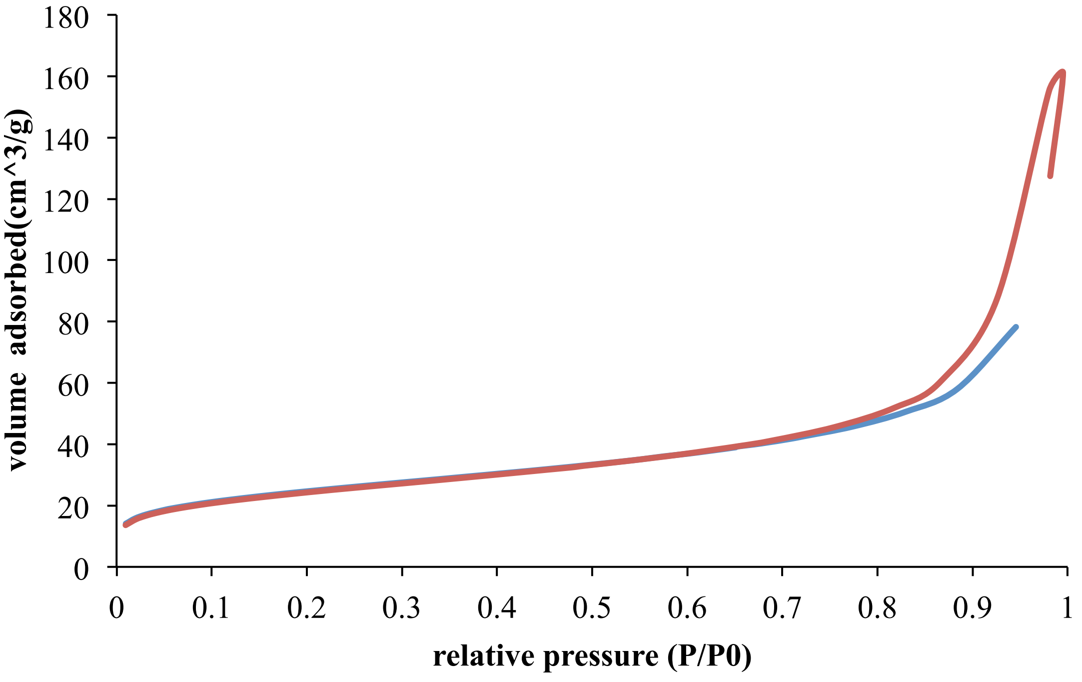

f) N_2 adsorption and desorption isotherm of material 3C

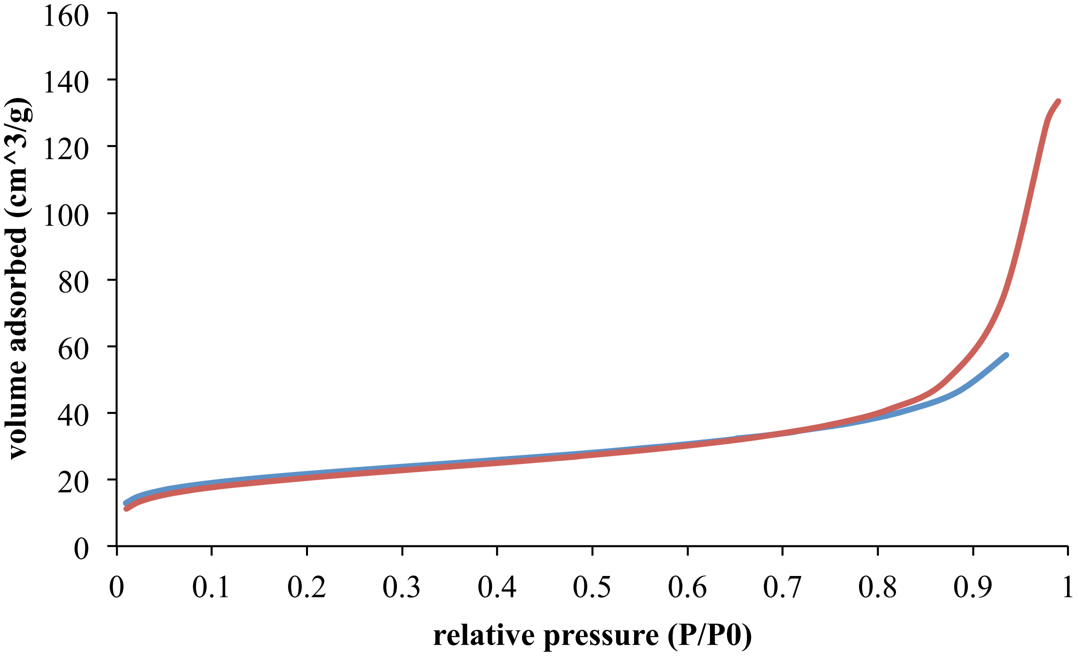

g) N_2 adsorption and desorption isotherm of material 3CT

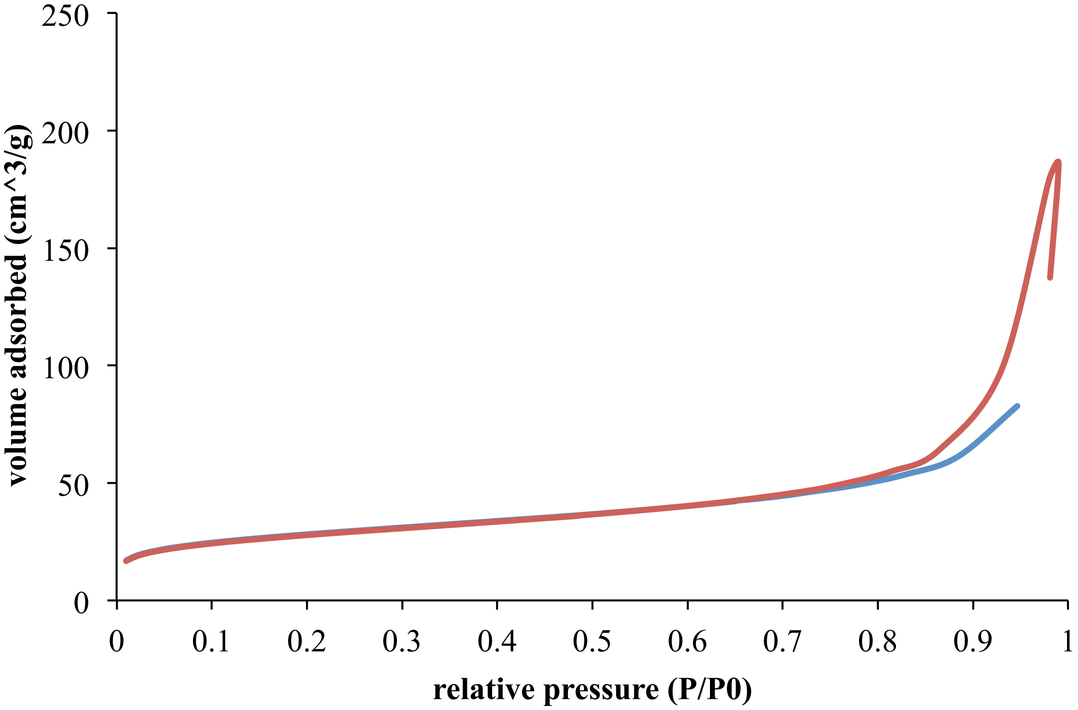

h) N_2 adsorption and desorption isotherm of material 4C

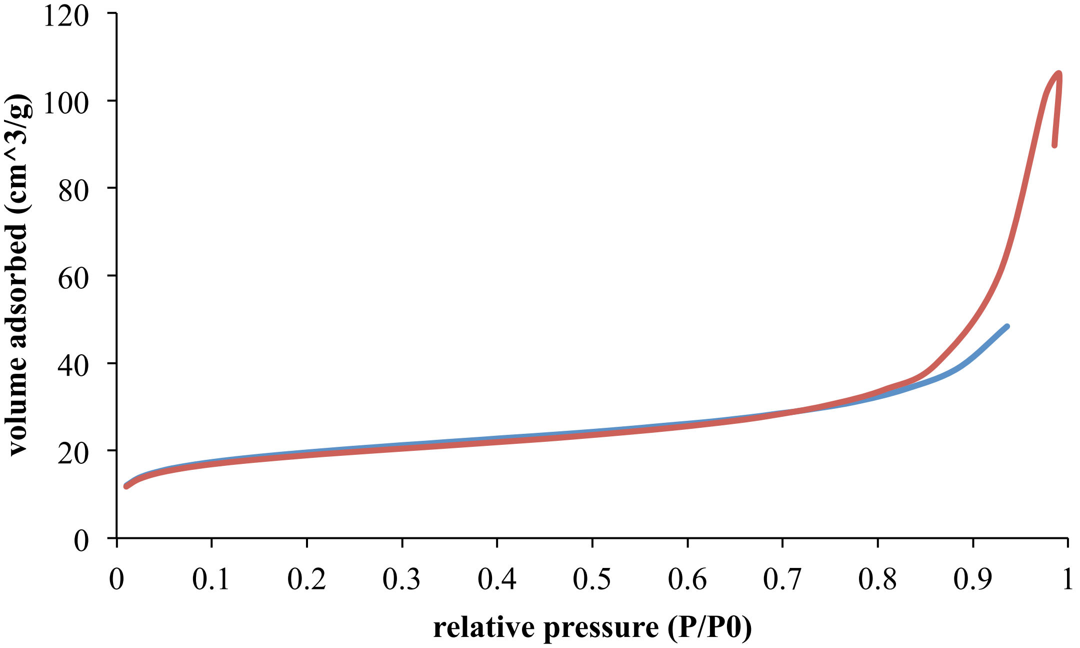

i) N_2 adsorption and desorption isotherm of material 4CT

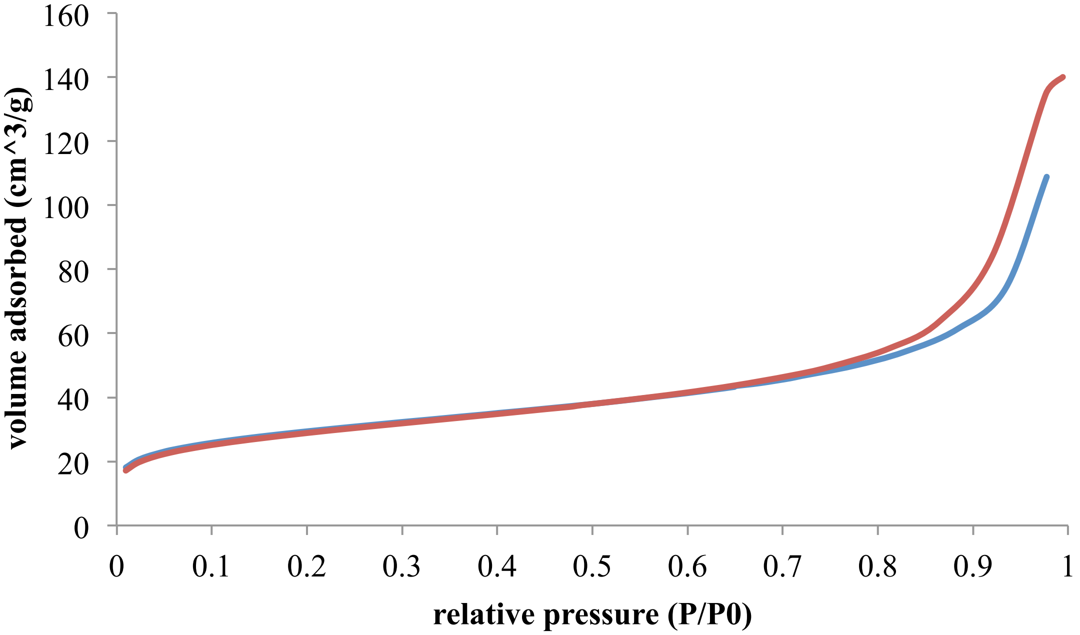

Figure 3.3.3. N_2 adsorption and desorption isotherms for support materials a) TiO_2 b) 1C, c) 1CT, d) 2C, e) 2CT, f) 3C, g) 3CT, h) 4C, i) 4CT (blue curve indicates adsorption isotherm and the red curve indicates desorption isotherm

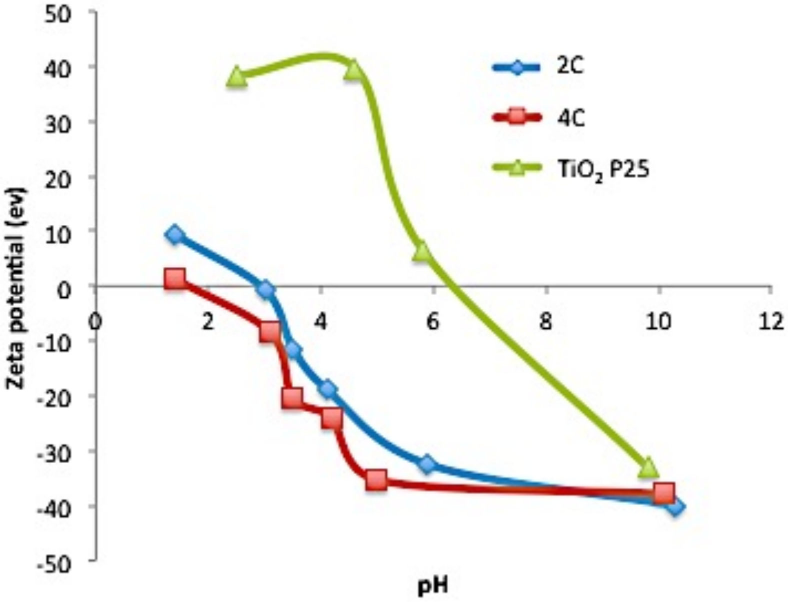

Figure 3.3.4. Zeta potential vs. measured solution pH for TiO_2 and materials 2C and 4C.

Characterization of Platinum morphology

All experimental materials were synthesized with 1.50±0.25 wt% Pt. Representative TEM micrographs of supported Pt materials are shown in Figure 3.3.5, and a summary of characterization results is given in Table 1. Pt particle size distributions for each sample are given in Supporting Information Figure 3.3.6. As synthesized, Pt on unmodified TiO_2 has average particle size of ~1.3 nm (TEM) and a CO chemisorption-derived dispersion of ~30%. Materials with 2 cycles SiO_2 with or without an additional template (Pt/2C and Pt/2CT) show slightly decreased average particle sizes, but the change is not significant given the particle size distributions. In contrast, dispersion increased significantly to > 45%. This high dispersion could be caused either by the presence of small Pt nanoclusters <1 nm that are missed in the TEM imaging, or by a flattened Pt particle morphology. Both scenarios would be caused by stronger interactions between Pt and the oxide support. It has previously been shown that adding oxides with a high cohesive energy, such as TiO_2 or ZrO_2, onto SiO_2 particles improves metal nanoparticle dispersion relative to that on the parent SiO_2.[86] These experiments show that materials with the reversed composition, where the SiO_2 overcoat is expected to be incomplete due to the low amount of added SiO_2 and/or to the presence of the templates, similarly leads to exposed SiO_2-TiO_2 interfaces that stabilize the Pt nanoparticles.

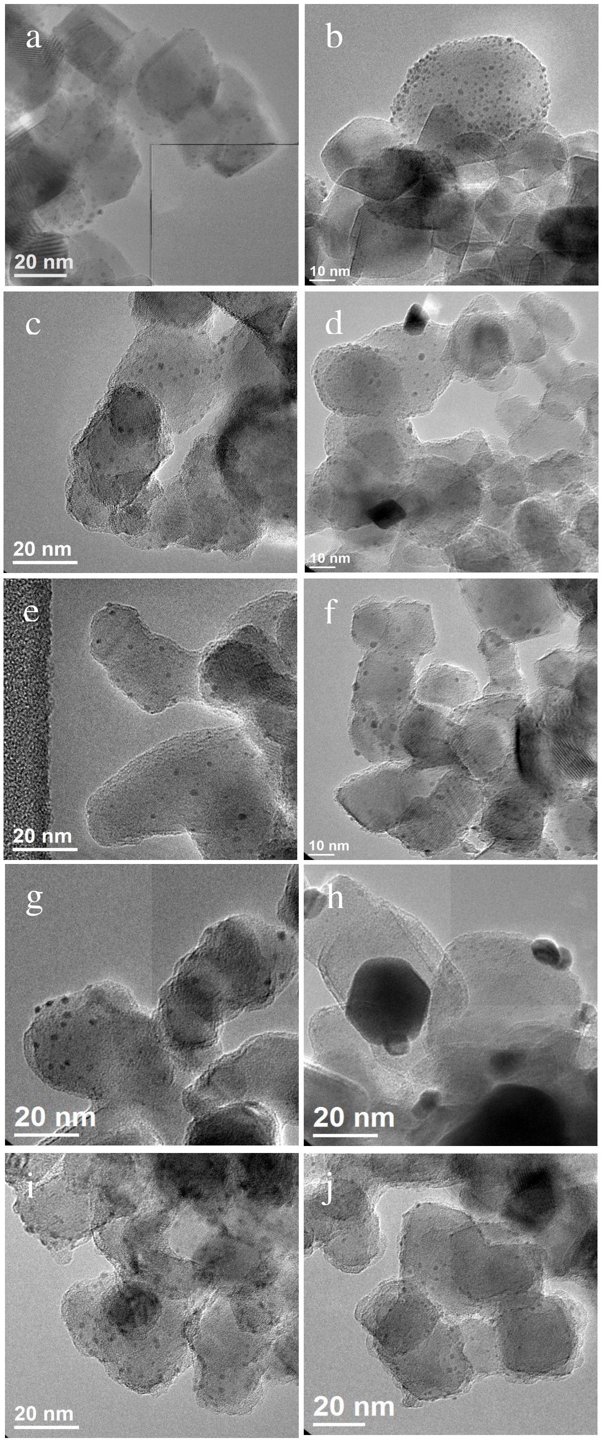

Figure 3.3.5. Representative TEM of as-synthesized catalysts a) Pt/TiO_2, b) Pt/2C, c) Pt/2CT, d) Pt/4C, e) Pt/4CT, and catalysts after additional heat treatment f) Pt/TiO_2-S, g) Pt/2C-S, h) Pt/2CT-S, i) Pt/4C-S and j) Pt/4CT-S.

a) Pt/TiO$_2$ (322 particles, blue) and Pt/TiO$_2$-S (122 particles, red)

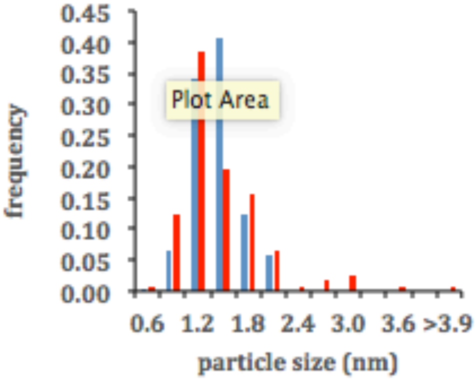

b) Pt/2C (246 particles, blue) and Pt/2C-S (189 particles, red)

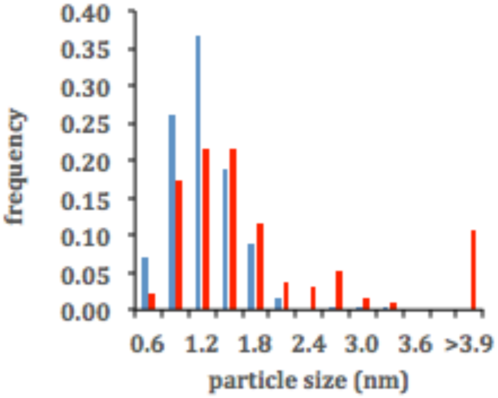

c) Pt/2CT (201 particles) and Pt/2CT -S (182 particles)

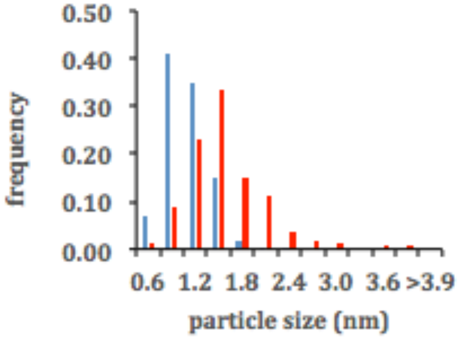

d) Pt/4C (121 particles, blue) and Pt/4C-S (76 particles, red)

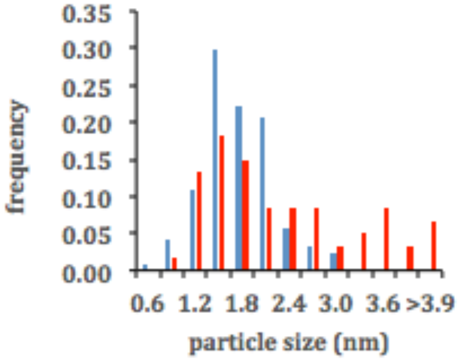

e) Pt/4CT (317 particles, blue) and
Pt/4CT-S (133 particles, red)

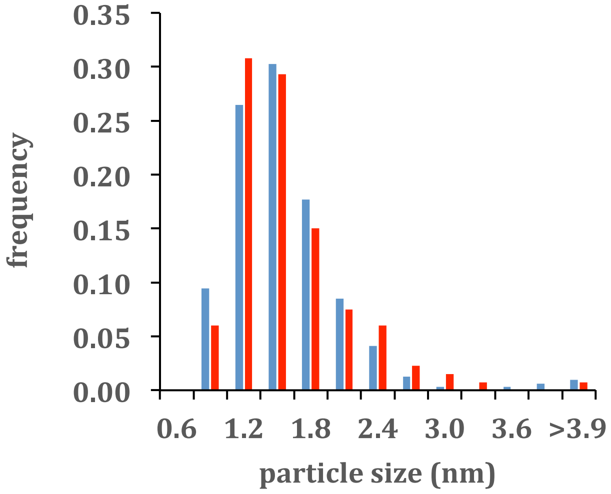

Figure 3.3.6. Pt nanoparticle size distributions from TEM images corresponding to Figure 2 of the main text. Samples a) Pt/TiO_2 and and Pt/TiO_2-S, b) Pt/2C and Pt/2C-S, c) Pt/2CT and Pt/2CT -S , d) Pt/4C and Pt/4C-S, and e) Pt/4CT and Pt/4CT-S. (Blue bars for particle size distribution of as-synthesized samples and red bars for particle size distribution of sintered samples)

After additional heat treatment at 500 °C for 5 hours in air, the Pt nanoparticle size distributions become broader for these three materials, and give slightly larger average particle sizes (for particle size distributions, see Figure 6). The dispersion of Pt nanoparticles on Pt/TiO_2 and Pt/2C decreases to ~20% and 30%, respectively, indicating a morphological change or the sintering of smaller clusters with extended heating. For Pt/TiO_2, the Pt particles become unevenly distributed on different TiO_2 grains, further attesting to the inhomogeneous distribution of Pt particles on the unmodified TiO_2 surface. In contrast, the dispersion of Pt nanoparticles on Pt/2CT remains above 45%. This gives an overall picture of Pt nanoparticles stabilized at the numerous SiO_2-TiO_2 interfaces present in materials Pt/2CT-S (Scheme 1). Increasing the SiO_2 thickness by using 4 cycles overcoating increases the Pt particle size and decreases the dispersion to as low as 11% (sample Pt/4C). This is consistent with a change towards larger and more spherical Pt nanoparticles due to the weak interaction between Pt and the SiO_2 surface that now is expected to coat the entire surface. For material Pt/4CT with 4 cycles SiO_2 coating over templates, the dispersion and particle sizes recover to values similar to that with the unmodified TiO_2. Although this material has the highest specific surface area of any sample, much of that will be from SiO_2 surfaces that are not ideal for achieving high Pt dispersion, rather than predominately the SiO_2-TiO_2 interfaces exposed in material Pt/2CT. After extended heating, the Pt particles grow further on 4-cycle material Pt/4C-S, and the dispersion remains low. However, Pt dispersion and particle sizes remain constant for material Pt/4CT-S, with 4 cycles SiO_2 over templates. This result parallels the stability of the analogous 2-cycle material Pt/2CT-S.

Overall, TEM and CO chemisorption make it clear that the use of thin SiO_2 overcoats, particularly those synthesized in conjunction with organic templates that create ample TiO_2-SiO_2 interface, and help stabilize highly dispersed Pt nanoparticles, even after extended heat treatment.

Table 3.3.1. Summary of Pt morphology and ethylene hydrogenation turnover frequencies (TOFs)

Sample	wt% Pt	Pt size (TEM, nm)[a]	dispersion Pt (%)[b]	Ethylene TOF (mol $\text{mol}_{\text{Pt.surf}}^{-1}$ sec^{-1})[b]	
				Initial[c]	8 hr
Pt/TiO_2	1.74	1.3±0.3	33	36	18
Pt/TiO_2-S[e]		1.4±0.6	20	35	20
Pt/2C	1.37	1.1±0.4	49	39	19
Pt/2C-S[e]		1.9±1.9[d]	32	42	23
Pt/2CT	1.31	1.0±0.3	48	49	22
Pt/2CT-S[e]		1.4±0.5	46	23	12
Pt/4CT	1.82	1.4±0.6	33	44	11
Pt/4CT-S[e]		1.4±0.5	35	35	14
Pt/4C	1.73	1.6±0.4	11	29	11
Pt/4C-S[e]		5.2±8.8[d]	15	26	11
Pt/SiO_2	0.5	n/a	32	20	10

[a] TEM particle size is measured as the longest width of a particle.

[b] Pt dispersion and $\text{mol}_{\text{Pt.surf}}$ determined from CO chemisorption; ethylene consumption TOF ±12% based on repeated runs of samples Pt/2C and Pt/2CT.

[c] Extrapolated to zero time from decay of TOFs between 1 and 15 hour.

[d] Sample contains significant amount of large Pt nanoparticles (>5 nm), therefore creating very large standard deviation in the average particle size calculation. When the large nanoparticles are excluded, the average TEM particle sizes for Pt/2C-S and Pt/4C-S are 1.7±1.5 and 2.1±1.0 nm, respectively.

[e] Sample names ending in "-S" indicate additional heating in air at 500 °C to encourage sintering.

Study of Ethylene hydrogenation reaction

In addition to sintering with time on stream, sintering during high-temperature regeneration cycles used to remove coke can be a significant problem for catalyst stability.[87] Thus, the supported Pt catalysts were examined using ethylene hydrogenation under intentionally deactivating conditions as a probe reaction to test resilience to coking and regeneration. Importantly, if the experimental catalysts are stabilized by a physical entrapment in a microporous surface, it would be expected to coke much more rapidly than the Pt/TiO_2 control. In contrast, similar coking behavior amongst the catalysts will indicate that the Pt remains exposed on the surface and that stabilization is based on the energetics of the interaction between the Pt nanoparticle and the modified surface. Two representative plots of TOF vs. time on stream are given in Figure 3.3.7a, and Table 3.3.1 summarizes turnover frequencies (TOFs) of ethylene consumption after 8 hours time on stream and extrapolated to initial time. The catalysts, including controls, generally deactivate ~55±10% over 8 hours under the conditions studied, and plots of conversion vs. time on stream in Figure 3.3.8 show that representative catalysts regain their activities after a short oxidative regeneration, indicating the loss of activity is indeed due to deposition of heavy byproducts.

Figure 3.3.7b shows that sample Pt/2C, with two cycles SiO_2 deposition and no template present, gives very similar TOFs to Pt/TiO_2 under all conditions. As a point of comparison, both give 8-hr TOFs of 20 ± 2 s^{-1} before or after additional calcination. Absolute rates change, but in accordance with changes in dispersion measured by CO chemisorption. Likewise, sample Pt/4C, with four cycles SiO_2 deposition and no template present, gives very similar TOFs to Pt/SiO_2 under all conditions. Here, both give 8-hr TOFs of 11 ± 1 s^{-1} before or after additional calcination. These limiting behaviors lead us to construct the illustrations in Scheme 3.2.1, where the Pt nanoparticles of Pt/4C are effectively on a SiO_2 surface, while the Pt nanoparticles of Pt/4CT are primarily located on the residual TiO_2 surface. These rates are consistent with our previous studies over related oxides,[82] which demonstrated that a ~2 nm thick SiO_2 overcoat effectively passivated the TiO_2 surface towards photoreduction of Ag, while a thinner coat retained the activity of the original TiO_2 surface.

Without over-interpreting the small relative differences in TOF, materials Pt/2CT and Pt/4CT, where the oxide coats were synthesized with a template, appear to straddle these two limiting behaviors. The initial TOFs over both as-synthesized materials resemble that of Pt/TiO_2. 2CT tracks the behavior of Pt/TiO_2 with time-on-stream, but loses half its specific activity upon calcination, whereupon it displays the lower TOF of Pt/SiO_2. In contrast, the TOFs of 4CT are similar to those of Pt/TiO_2 at initial time, but its TOF decreases with time-on-stream towards the slower rates of Pt/SiO_2. These behaviors again lead to the illustrations of Scheme 1, where the Pt nanoparticles are present at TiO_2-SiO_2 interfaces of different morphology and can display reactivity indicative of either support, depending on prior treatment and reaction conditions.

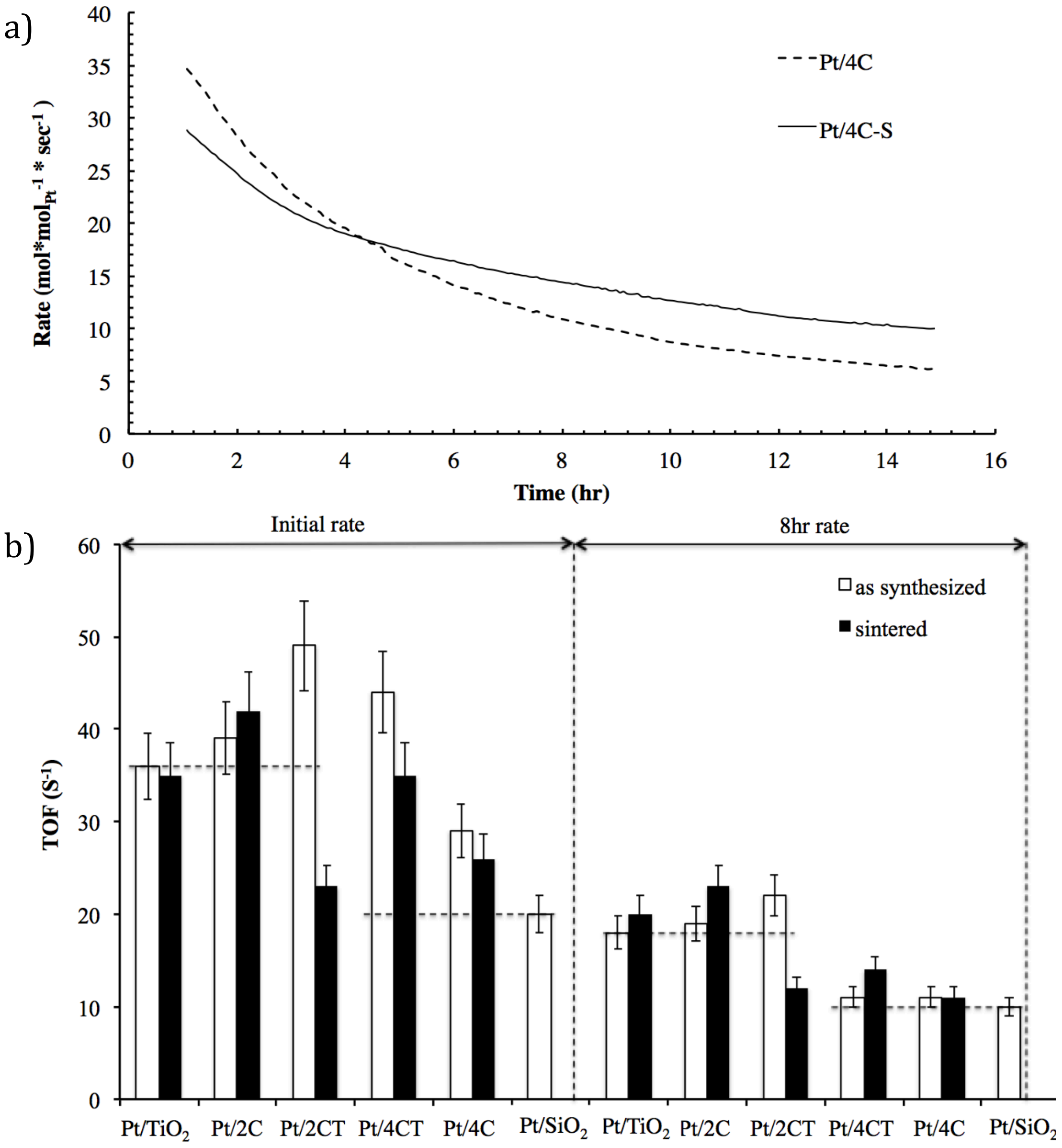

Figure 3.3.7. a) Representative plot of TOF (s^{-1}) vs. time on stream for samples Pt/4CT and Pt/4CT-S, b) Plots of initial and 8hr TOF of samples before and after deliberate heat treatment.

a) Pt/TiO$_2$

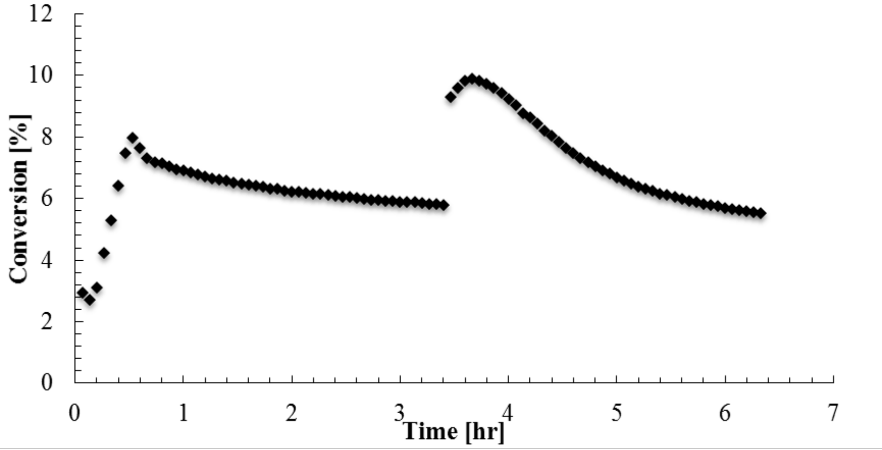

b) Pt/2C

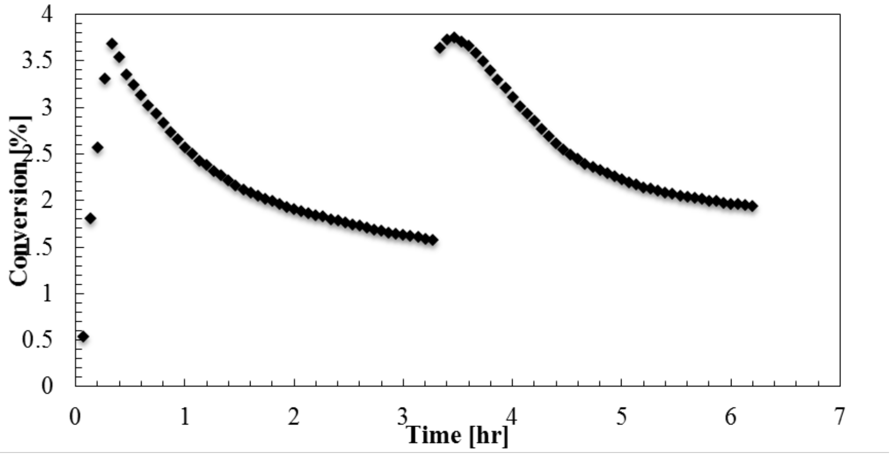

c) Pt/2CT

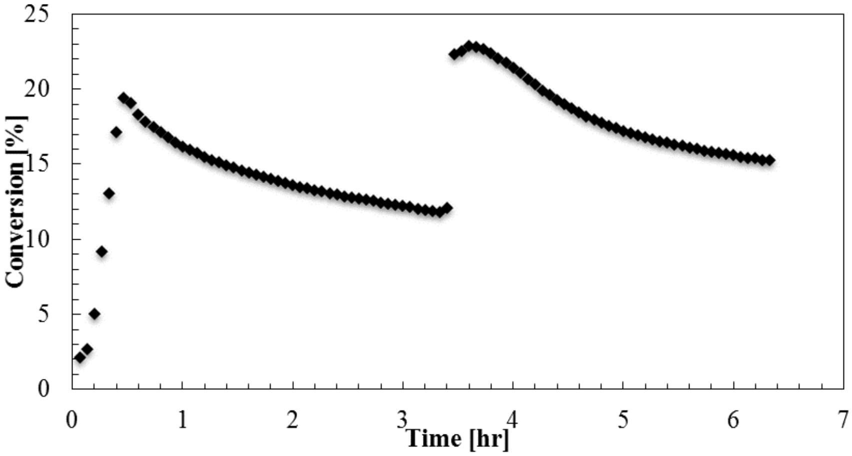

Figure 3.3.8. Conversion vs. time plots for ethylene hydrogenation at 80°C of a) Pt/TiO_2, b) Pt/2C, c) Pt/2CT. Samples are regenerated in O_2 at 450°C after approximately 3.5 h TOS. The recovery of conversion indicates that deactivation during reaction is primarily by coking or accumulation of other heavy species.

Overall, ethylene hydrogenation reveals that the nature of the SiO_2 overcoat, as determined by templates and amount of SiO_2 deposited, plays a significant role in determining the reactivity of the supported Pt nanoparticles. At 80 °C, the TOFs of these materials are as expected and generally fall between the limiting rates of Pt/TiO_2 and Pt/SiO_2. Qualitatively, the similar coking behavior observed across the set of materials also indicates that the Pt nanoparticles sit exposed on the modified TiO_2 surfaces, rather than buried in micropores or completely overcoated. However, because of the higher Pt dispersion and stability on the partially over-coated materials 2C, 2CT, and 4CT, these materials showed (Figure 3.3.9) 30-100% improvements in hydrogenation rate per total mass of Pt, relative to Pt/TiO_2.

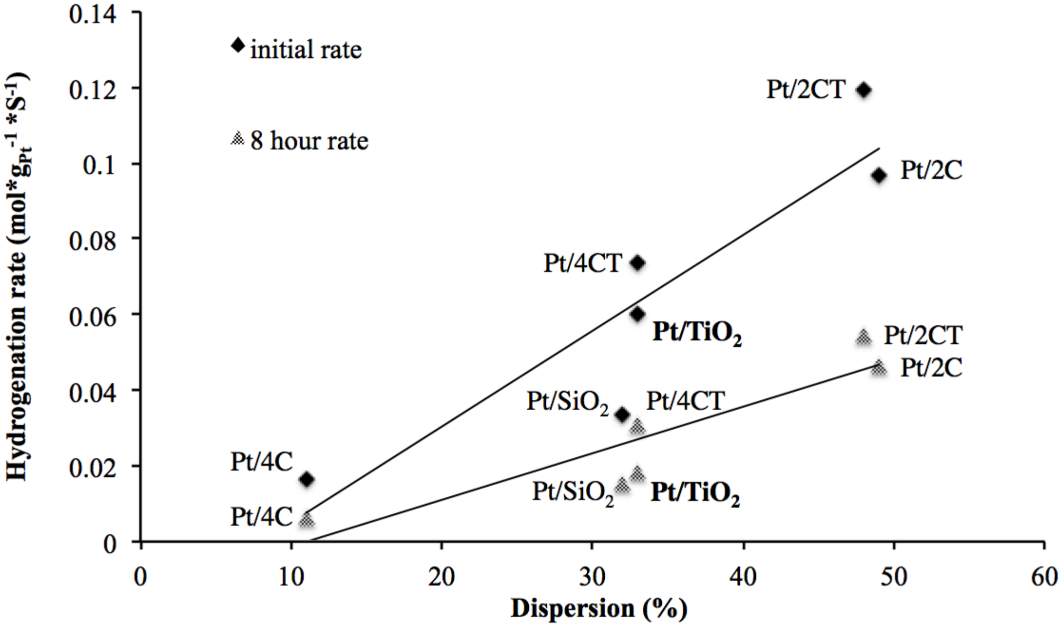

Figure 3.3.9. Summary of initial and 8-hour ethlyene consumption rate vs. Pt dispersion for ethylene hydrogenation at 80 °C catalyzed by samples Pt/TiO$_2$, Pt/2C, Pt/2CS, Pt/4C, Pt/4CS and Pt/SiO$_2$, highlighting the performace gains afforded by partial overcoating. Full data are also given in Table 3.3.2.

Table 3.3.2. Summary of absolute ethylene hydrogenation rates for all samples.

Samples	**Conversion at 8hr**	**Dispersion (%)**	**Hydrogenation rate [mol*total g_{Pt}^{-1} *s^{-1}]**	
			Initial	8hr
Pt/TiO_2	4.3%	33	0.060	0.031
Pt/TiO_2 -S	3.6%	20	0.036	0.021
Pt/2C	5.4%	49	0.097	0.046
Pt/2C-S	3.7%	32	0.068	0.037
Pt/2CT	6.7%	48	0.120	0.054
Pt/2CT-S	3.6%	46	0.055	0.029
Pt/4CT	2.6%	33	0.074	0.018
Pt/4CT-S	3.3%	35	0.063	0.026
Pt/4C	4.3%	11	0.016	0.006
Pt/4C-S	2.2%	15	0.020	0.008
Pt/SiO_2	2.0%	32	0.033	0.016

Adding thin SiO_2 overcoats to TiO_2 powders has been shown here to significantly impact the oxide surface morphology and chemistry, and subsequently to change the catalytic stability and reactivity of supported Pt nanoparticles. Continuing previous work by some of us, we show that adding repeated cycles of limiting amounts of TEOS under basic conditions is able to build up a 1-2 nm conformal film of SiO_2 on a pre-existing support particle. Since it requires no specialized equipment or precursors, this method can be utilized in scale-up synthesis of catalysts. Previously depositing an organic template onto the original TiO_2 support ensures that voids are left in the SiO_2 film. This greatly increases the total surface area after template removal, and ensures small domains of TiO_2 remain uncovered. In the latter case, samples 2C, 2CT, and 4CT all have incomplete SiO_2 films and thus display TiO_2–SiO_2 interfaces, either due to the use of limiting TEOS or the presence of surface templates. As summarized in Figure 3.3.9, this very simple material pretreatment of the original TiO_2 support can significantly improve the catalytic behavior of these particles by improving the Pt dispersion as synthesized and especially after heat treatments representative of these needed to clear coke deposits from a deactivated catalyst. The benefits of the improved stability using the templated supports 2CT and 4CT are expected to become more pronounced with extended regeneration experiments and times on stream more typical of industrial application, as well as reactions requiring higher temperatures such as alkane dehydrogenation.

3.4 Conclusion

This concept of simply ‘backfilling’ metals by impregnation onto a partially overcoated, conventional oxide support exploits the well-known stability of metal nanoparticles on supports like TiO_2 and the corresponding tendency to aggregate on supports like SiO_2. The nanostructure of the partially overcoated supports used here thus creates an energetic barrier for nanoparticles to cross from one TiO_2 domain to another or to grow beyond a certain size, which may be further accentuated by particularly strong interactions with Pt at the TiO_2-SiO_2 interface. Rather than the one-off development of a new supported Pt catalyst, the significance of this study is that proper nanostructuring of a mixed oxide support can create a surface that better stabilizes metal nanoparticles than either of the components. The net result is a novel and scalable preparation strategy for generating highly dispersed metal nanoparticles and enhancing their thermal stability under conditions characteristic of catalyst regeneration. These modifications preserve or improve the catalytic activity of the original catalyst, and the catalyst properties may be further manipulated by tuning the amount of SiO_2 deposited and the use of molecular templates. Further study is underway to expand the scope of this synthesis strategy to different oxide combinations, templates, metals, and catalytic probe reactions.

Chapter 4

Strong Electrostatic Adsorption of Pt onto SiO_2 partially Overcoated Al_2O_3

4.1 Introduction

Supported atomically dispersed metal catalysts can maximize the efficiency of precious metal use in catalyst synthesis and reduce the overall material cost. Meanwhile, atomically dispersed metal atoms show unusual catalytic behaviors in certain reactions compared to the metal atoms in the nanoparticle form.[88-90] Therefore, catalysis community is interested in developing various strategies for preparing supported atomically dispersed metal catalysts.[89, 91-93] For example, Flytzani-Stephanopoulos's group at Tufts University reported using a zeolite support with the addition of Alkaline ions to stabilize mononuclear Au species, and the resulted material is active for water-gas-shift (WGS) reaction at 200°C.[92] The same group also reported using NaCN to etch the as-synthesized TiO_2 supported Au catalyst to prepare atomically dispersed Au catalyst.[91] Nanfeng's group at Xiamen University reported using photochemical synthesis route to deposit atomically dispersed Pd on TiO_2 nanosheets.[93] In summary, most of the previous reported procedures rely on either using special support material or requiring extensive post treatments, therefore limiting their broad applications in scale up synthesis of many different supported atomically dispersed metal catalysts.

Here, we report using Strong Electrostatic Adsorption (SEA) method to prepare highly dispersed Al_2O_3 supported Pt catalyst partially overcoated with SiO_2. SEA relies on the electrostatic interaction between metal precursor ions and the support surface to deposit metal precursor ions. An oxide surface has hydroxyl groups that can deprotonate or protonate depending on whether the solution pH is below or above the isoelectric point (IEP) of the oxide, and IEP is at which the hydroxyl groups of the oxide surface are neutral. When the solution pH is below the IEP of the oxide, the surface hydroxyl groups protonate and the surface becomes positively charged, thus metal anions can be adsorbed. When the pH is above the IEP of the oxide, the surface hydroxyl groups deprotonate and the surface become negatively charged, thus metal cations can be adsorbed. The IEP of support material Al_2O_3 is approximately pH 9 and the IEP of the overcoat material SiO_2 is around pH 2. When the pH of metal precursor solution is in between 2 and 9, the support material becomes positively charged while the overcoat material becomes negatively charged, therefore allowing selective adsorption of Pt anions onto the support domain not the overcoat domain. [13, 39, 94]

SEA has been reported before to deposit highly dispersed Noble metal nanoparticles onto various supports with particle size well below 1nm.[16, 94, 95] We have previously demonstrated that the use of a SiO_2 partial overcoat on the TiO_2 support improves the dispersion and thermal stability of Pt nanoclusters (<2nm) while the catalytic activity (Ethlyene hydrogenation) of the Pt is still preserved (chapter 3). In this study, the hypothesis is that the partial overcoat helps isolate the metal precursor ions from each other during the SEA process (demonstrated in scheme 4.2.1), therefore allowing deposition of atomically dispersed metal atoms onto the support surface. Specifically, Al_2O_3 nanoparticles were first overcoated with a thin layer of SiO_2 (<5nm) using a Stöber method modified from our group's previous research.[42] Then H_2PtCl_6 precursor was deposited onto the support via SEA method adapted from previous reports.[15, 39, 94]

Compared to the previously reported strategies, the combined use of SEA and partial overcoat approach in our study allows the preparation of many different supported highly dispersed, potentially atomically dispersed metal catalysts and suits the requirements of catalyst production at larger scale.

4.2 Experiment

Support Modification

Calixarene Grafting: Calixarene grafting procedure was adapted from previous methods.[41, 42] In a typical experiment, 5g of Al_2O_3 (Alfa Aesar, Nanophase NanoArc, 40-50nm particle size, 37m^2/g by BET, 70% α phase and 30% ϒ phase) and 100mg of 4-tert-butylCalix[4]arene ("Calixarene", Sigma Aldrich, 95%) were boiled in ~100 ml refluxed toluene solvent at 110°C for 4 hours to reach theoretical loading of 0.5 groups/nm^2. Then the Calixarene grafted Al_2O_3 was vacuum filtered and washed with 200 ml of toluene and 200 ml of hexane followed by vacuum drying for at least 12 hours.

SiO_2 overcoating: SiO_2 was overcoated onto the unmodified and the modified Al_2O_3 supports using a previously reported procedure.[42] Bare Al_2O_3 or Calixarene grafted Al_2O_3 (5g) was dispersed in a mixture of ethanol (64ml, 200 proof, Fisher Scientific) and NH_4OH (9.7 ml, base catalyst, 28-30 wt%, Macron Fine Chemicals) and then sonicated for 30 minutes. Afterward, 209 ul of TEOS (GC grade; ≥99%; Sigma-Aldrich) was added, and the mixture was shaken for 1 hour to have the first cycle of SiO_2 deposited. The subsequent deposition cycle consists of sonicating the mixture for 30 minutes before deposition, since

the hydroxyl density on the SiO_2 overcoat is lower than the Al_2O_3 support, only 160 ul of TEOS was added for the later cycles followed by shaking for 1hr. After the coating process, the as-made materials were vacuum filtered and air dried for 12 hrs. Then the materials were heat treated at 650°C for 4 hours with heating rate of 3.5°C/min.[42] (Supports synthesized are illustrated in scheme 4.2.1)

IEP measurement: Stock solutions with different pHs (1-10) of the support material in nanopure water were prepared first (9.8 mM),[96] the pH was adjusted with HNO_3 or NH_4OH. Then the solutions were shaken for 1hour to reach equilibrium and the pHs of solutions were re-measured. Afterwards, the zeta potentials of the as made solution samples were measured using a Malvern Instrument Nano ZS Zetasizer. The zeta potentials Vs. pH curve was plotted for each support material and the data was fitted using sigmoidal function in Matlab®, the IEP was extrapolated as the pH where Zeta potential equals to zero.

Pt adsorption experiment: The Pt adsorption experiment was designed to determine the pH that yields maximum Pt uptake on different support surfaces and was adapted from previously reported procedure.[94] A stock solution (2mM) of $H_2PtCl_6 \bullet 6H_2O$ (Sigma Aldrich) in nanopure water was prepared first. Then the stock solution was split into several units (30ml/unit) with pH adjusted to 1.5, 2, 3, 4 and 5 using HCl or NaOH, since NH_4OH will form complexes with H_2PtCl_6, it should be avoided in Pt adsorption experiment.[94] The pH tuned solution units were shaken for 48 hours before use. Afterwards, for every 100 mg support material, 4 ml pH tuned solution was added and the mixture was shaken for at least 12 hours. Finally the Pt loaded support materials were filtered out and dried for ICP analysis.

Pt SEA: Based on results from Pt adsorption experiment, pH 4 was decided to be the optimal Pt deposition pH. A Pt precursor solution (2mM) was prepared by dissolving $H_2PtCl_6 \bullet 6H_2O$ (Sigma Aldrich) in nanopure water and was tuned to pH 4 using HCl, then the precursor solution was shaken for 48 hours to reach equilibrium. Afterwards, the support (2.2 g) was dispersed in 80 ml pH adjusted precursor, the mixture was sonicated and shaken for 12 hours. The Pt loaded support was vacuum filtered, washed with 100 ml of nanopure water and air dried for 24 hours. Finally the as made material was reduced in 10%H_2/N_2 at 250 °C for 1hr with heating rate of 2.5 °C/min. See scheme 4.2.1 for all the samples synthesized via SEA.

Pt wetness impregnation: Two supports (4c/4ct) were wetness impregnated with H_2PtCl_6 precursor to prepare samples **Pt 4c wi** and **Pt 4ct wi**. A stock solution (0.2ml) of H_2PtCl_6 was made to achieve Pt loading of 0.2wt% on 2g support material. The stock solution was sprayed onto the support material and the precursor loaded support was dried with vacuum assistance for 48 hours to remove the solvent. Finally the samples were reduced at 250 °C for 1hr with heating rate of 2.5 °C/min. See scheme 4.2.1 for all the samples synthesized via wetness impregnation.

Sample Characterization: Samples were dried in vacuum at 110°C for at least 12 hours before N_2 physisorption using a Micrometric ASAP 2010, the surface area was calculated using the Brunauer–Emmett–Teller (BET) method and the micropore area was calculated using the t-plot. Thermogravimetric analysis was performed using a TA Instruments Q500 under 90%/10% O_2/N_2. Mass loss between 300 °C and 800 °C was assigned as the mass of the grafted calixarene molecules. Pt loading was determined using a Thermo iCap7600 ICP-

OES, the sample was digested in a mixture of aqua regia and HF (33 vol% of 70 wt% HNO_3 with 66 vol% of 37 wt% HCl, both Fisher Chemical Inc.). TEM was performed using a JEOL-2100 fast transmission electron microscope, the TEM sample was prepared by dispersing the sample in ethanol, sonicating and drop casting onto a TEM grid followed by air drying. Pulse CO chemisorption was performed using an AMI 200 chemisorption analyzer (Altamira Inc.) Sample was first loaded into a U-shape quart tube, reduced in 5%H_2/Ar at 250 °C for 1 hour, then cool down to room temperature in He, afterwards dosed 30 times with 5% CO/He to saturate the Pt surface. The effluent CO was monitored by a thermal conductive detector (TCD) normalized to CO flows, and the amount of chemisorbed CO was calculated as the sum of differences in area between the early pulses and the later pulses. The amount of surface Pt atoms was calculated using a CO to Pt ratio of 1:1, and the dispersion ratio of Pt was calculated as the ratio between surface Pt atoms and total number of Pt atoms. The sample for CO-FTIR was prepared by diluting a catalyst sample with KBr first. CO-FTIR measurement was performed by treating the sample at 100 °C in Argon for 1 hour, then reducing the sample at 100 °C in 5% H_2/Ar followed by cooling down to room temperature in Ar. The background spectrum was collected first, afterwards CO gas was purged to saturate the Pt surface. Finally the excessive CO was purged away by Ar and FTIR spectrum was collected. The collected signals were converted to Kubelka-Munk units with background signals removed first. The CO peak region of the spectrum was isolated first and was processed using solver function in Excel.

Propylene hydrogenation: With the goal of reaching differential conversion (around 10%), the catalyst samples were all diluted with pure Al_2O_3 at a mass ratio between 1: 255 and

1:330. The diluted catalyst sample was loaded onto quartz wool inside a glass tube reactor. A mixture of 3% ethylene (20 mL/min, Airgas, balance Ar), Ar (100 mL/min, Airgas, 99.999%) and 10% H_2 (100 mL/min, Airgas, balance Ar) was delivered into the reactor and the reaction was studied at 50 °C for 5 hours. In some cases, the catalyst sample after reaction was regenerated at 250 °C in 20% O_2/He for 1 hour by heating the sample under Ar at 5°C/min, finally cooling down to room temperature under Ar. The products from the reactions were monitored using an Agilent 7890A GC system equipped with a flame ionization detector (FID) using a GS-GasPro column (30m x 60 mm x 0.32 μm). Data was collected every 4 minutes for 5 hours. Propylene and propane were the only identified species in the GC chromatogram.

Scheme 4.2.1. Procedures for support modification, sol-gel deposition and Pt deposition

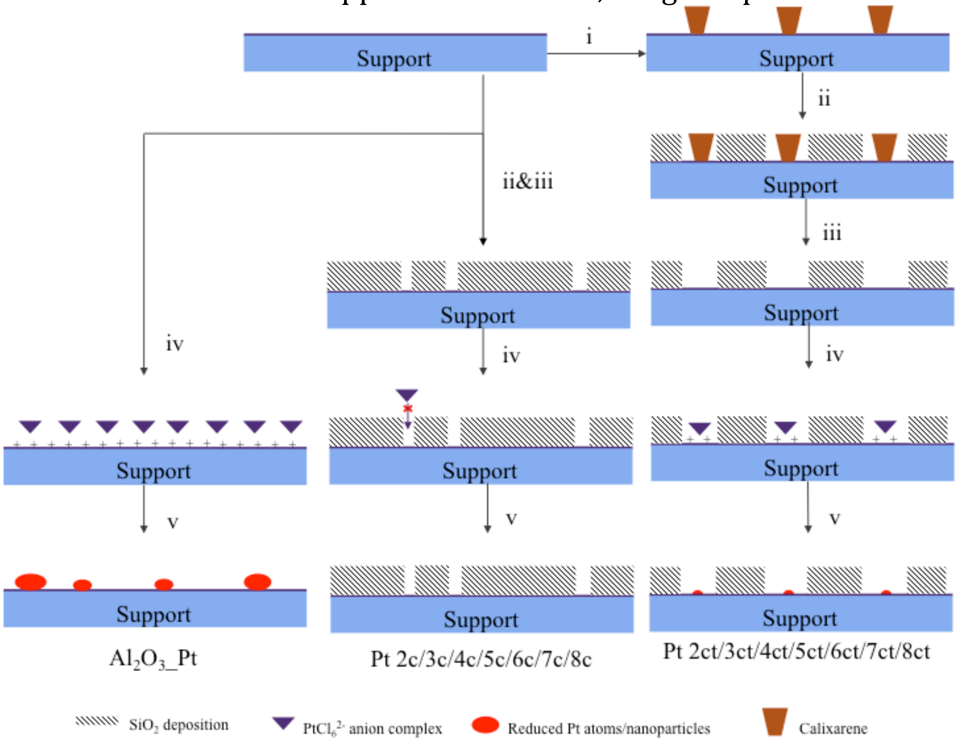

i. Grafting templates in toluene at 110 °C for 4 hours
ii. Overcoating SiO_2 in a base catalyzed sol gel deposition process
iii. Calcination at 650 °C in air for 4 hours
iv. SEA of $PtCl_6^{2-}$ anion complex
v. Reduction at 250 °C

4.3 Results and discussion

Support modification

The TGA result shows the loading of the calixarene molecules on the Al_2O_3 surface after grafting is ~0.3 groups/nm^2, reaching the geometric limit for grafting calixarene on the oxide support surface (figure 4.3.1.).[41, 42] BET surface area of both template and untemplated supports increase when more SiO_2 was deposited onto the surface (all surface area data included in table 4.3.1). While no significant difference in surface area is observed between the templated and untemplated support at each cycle of SiO_2 deposition. The adsorption and desorption isothermal curves in N_2 physisorption experiments for all supports are included in figure 4.3.2. The IEP measurements in figure 4.3.3 show that the IEP of a support continuously decreases from ~pH 9 to ~pH 2 with increased amount of SiO_2 deposited onto the support surface regardless of the presence of templates. The IEP of bare Al_2O_3 support is similar to the historically reported value,[97] and the IEP of the support with 4 cycles of SiO_2 deposition is within the previously reported IEP range of Silica (pH 2-4), indicating most of the support surface is covered by SiO_2 after 4 cycles of SiO_2 deposition (Estimated IEPs of supports are summarized in table 4.3.2).[98-100]

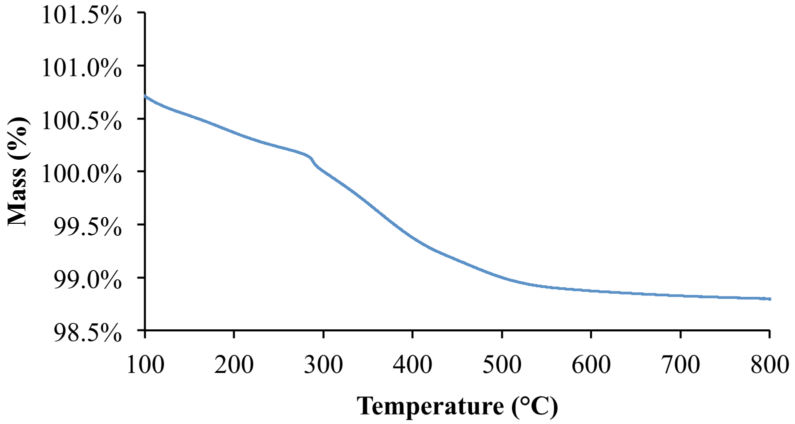

Figure 4.3.1. Mass loss Vs. temperature curve of calixarene grafted Al_2O_3 support in TGA experiment, calixarene starts to decompose at 300 °C.

Table 4.3.1. N_2 Physisorption results of all supports

Samples	BET surface area (m^2/g)	Micropore area (m^2/g)	External area (m^2/g)
Al_2O_3	37	1.8	35.2
Al_2O_3 1c	38.4	3.8	34.6
Al_2O_3 1ct	39.2	4	35.2
Al_2O_3 2c	40.6	4	36.6
Al_2O_3 2ct	40.9	2.6	38.3
Al_2O_3 3c	41.3	4.1	37.2
Al_2O_3 3ct	40.6	2.8	37.8
Al_2O_3 4c	42.8	4.1	38.7
Al_2O_3 4ct	43.8	2.8	41
Al_2O_3 5c	43.5	7.9	35.6
Al_2O_3 5ct	43.2	2.5	40.7
Al_2O_3 6c	43.2	4.9	38.3
Al_2O_3 6ct	41	3.9	37.1
Al_2O_3 7c	45.8	2.5	43.3
Al_2O_3 7ct	50	2.2	47.8
Al_2O_3 8c	45.4	3.2	42.2
Al_2O_3 8ct	49.9	2.2	47.7

a)

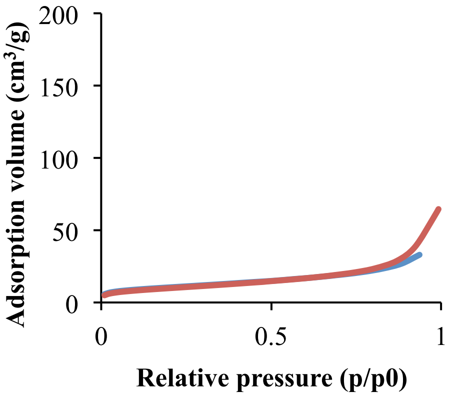
Adsorption volume (cm^3/g)
200
150
100
50
0
0
0.5
1
Relative pressure (p/p0)

b)

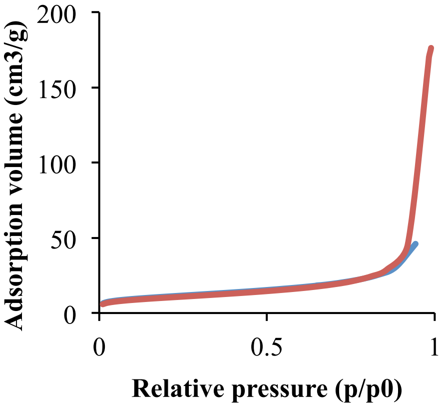
Adsorption volume (cm3/g)
200
150
100
50
0
0
0.5
1
Relative pressure (p/p0)

c)

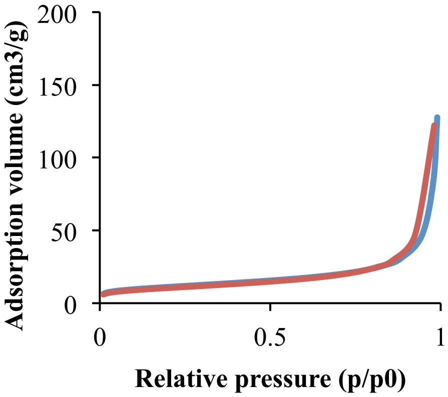
Adsorption volume (cm3/g)
200
150
100
50
0
0
0.5
1
Relative pressure (p/p0)

d)

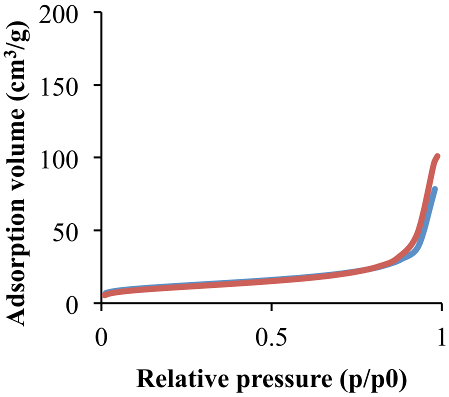
Adsorption volume (cm^3/g)
200
150
100
50
0
0
0.5
1
Relative pressure (p/p0)

e)

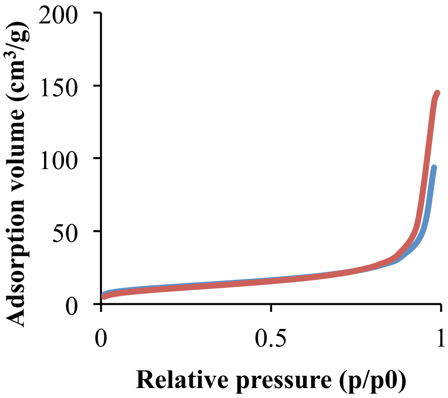
Adsorption volume (cm^3/g)
200
150
100
50
0
0
0.5
1
Relative pressure (p/p0)

f)

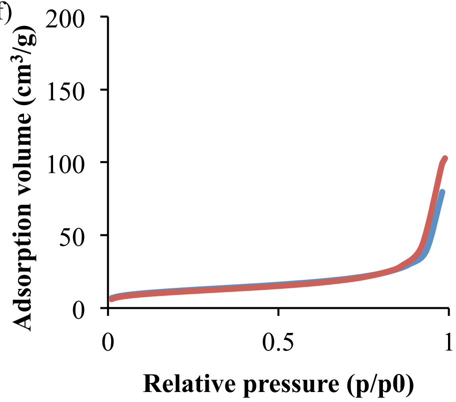
Adsorption volume (cm^3/g)
200
150
100
50
0
0
0.5
1
Relative pressure (p/p0)

g)

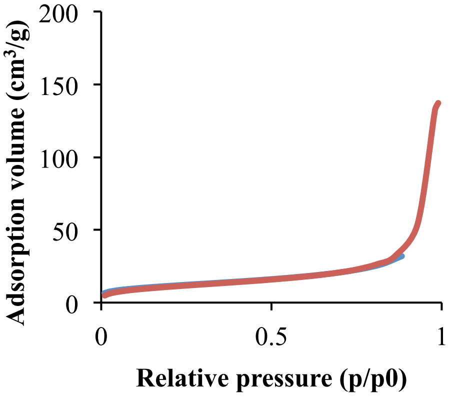
Adsorption volume (cm^3/g)
200
150
100
50
0
0
0.5
1
Relative pressure (p/p0)

h)

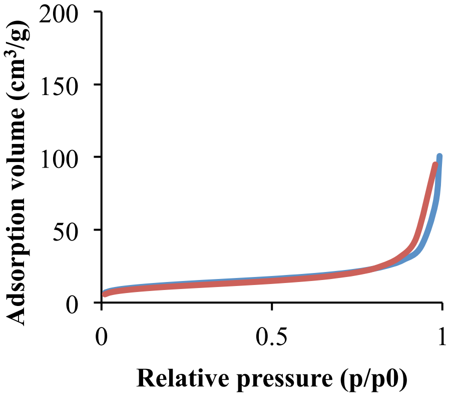
Adsorption volume (cm^3/g)
200
150
100
50
0
0
0.5
1
Relative pressure (p/p0)

i)

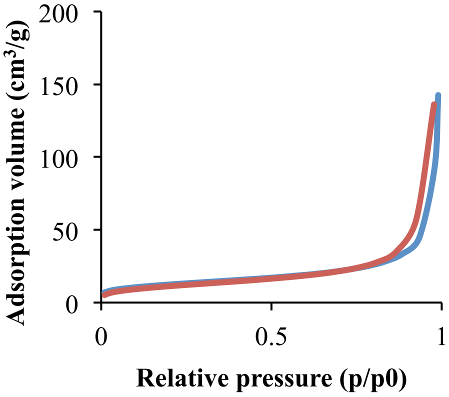
Adsorption volume (cm^3/g)
200
150
100
50
0
0
0.5
1
Relative pressure (p/p0)

j)

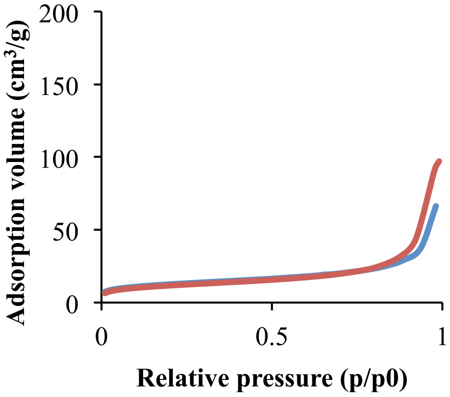
Adsorption volume (cm^3/g)
200
150
100
50
0
0
0.5
1
Relative pressure (p/p0)

k)

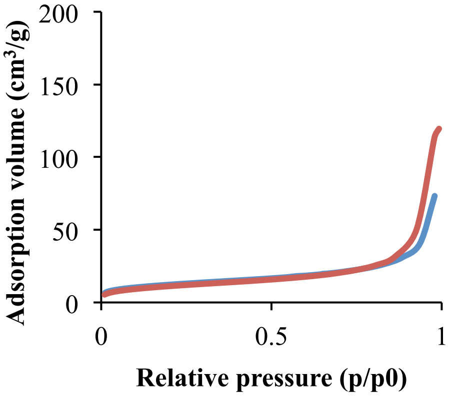
Adsorption volume (cm^3/g)
200
150
100
50
0
0
0.5
1
Relative pressure (p/p0)

l

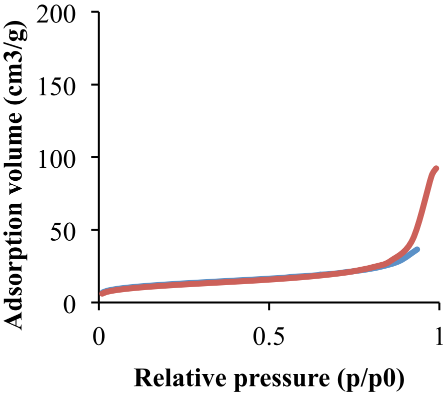
Adsorption volume (cm3/g)
200
150
100
50
0
0
0.5
1
Relative pressure (p/p0)

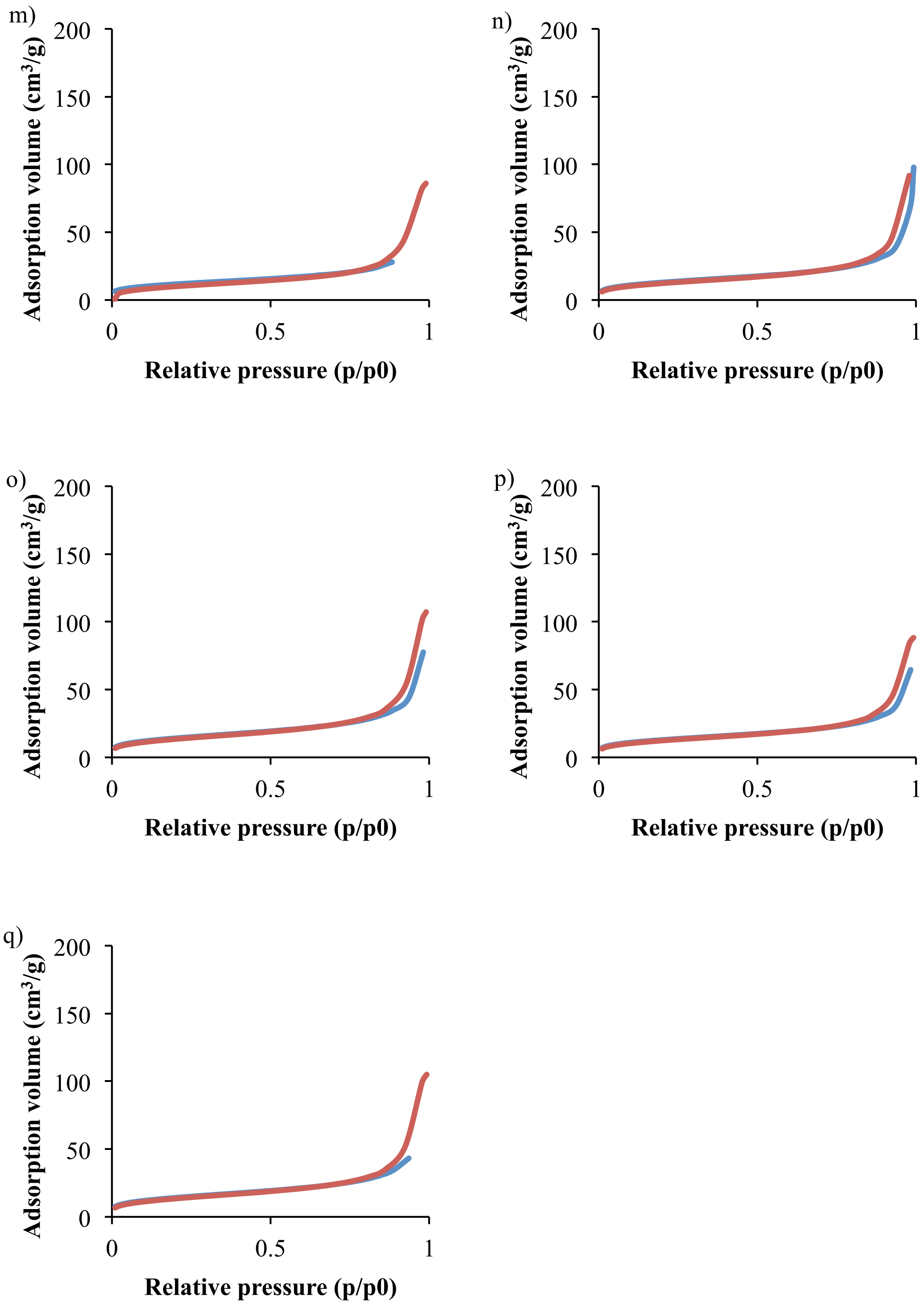

Figure 4.3.2. N_2 Adsorption and desorption isothermal curves for supports unmodified a) Al_2O_3, b) 1c, c) 1ct d) 2c, e) 2ct, f) 3c, g) 3ct, h) 4c, i) 4ct, j) 5c, k) 5ct, l) 6c, m) 6ct, n) 7c, o) 7ct, p) 8c, q) 8ct

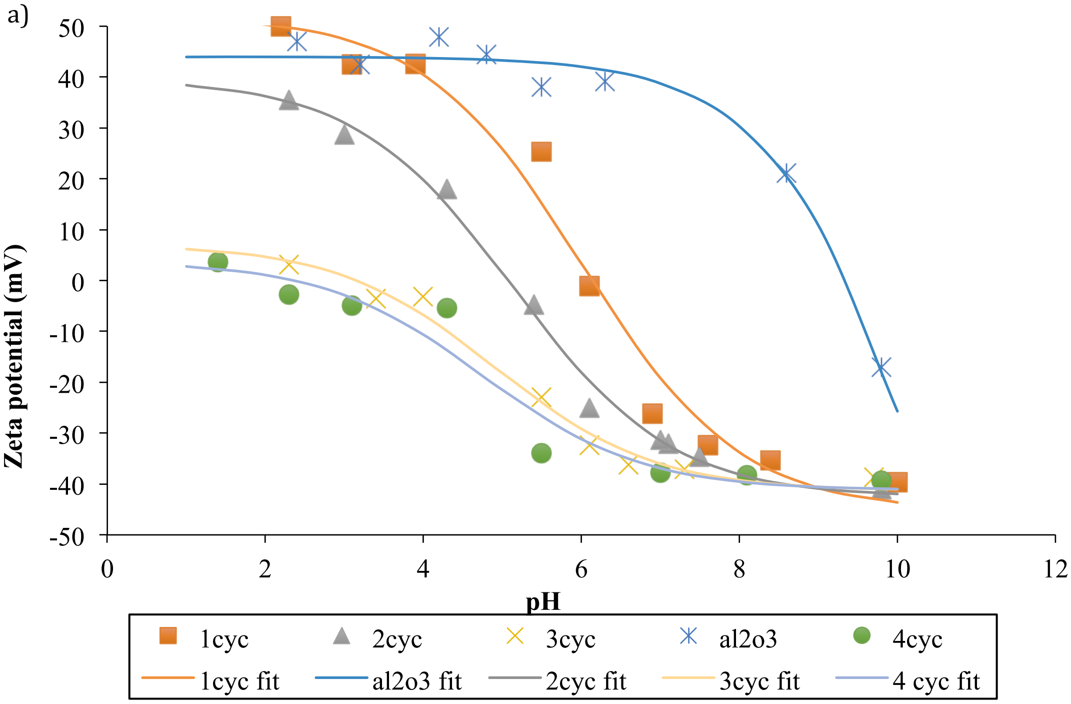
a)
Zeta potential (mV)
50
40
30
20
10
0
-10
-20
-30
-40
-50
0
2
4
6
8
10
12
pH
1cyc
2cyc
3cyc
al2o3
4cyc
1cyc fit
al2o3 fit
2cyc fit
3cyc fit
4 cyc fit

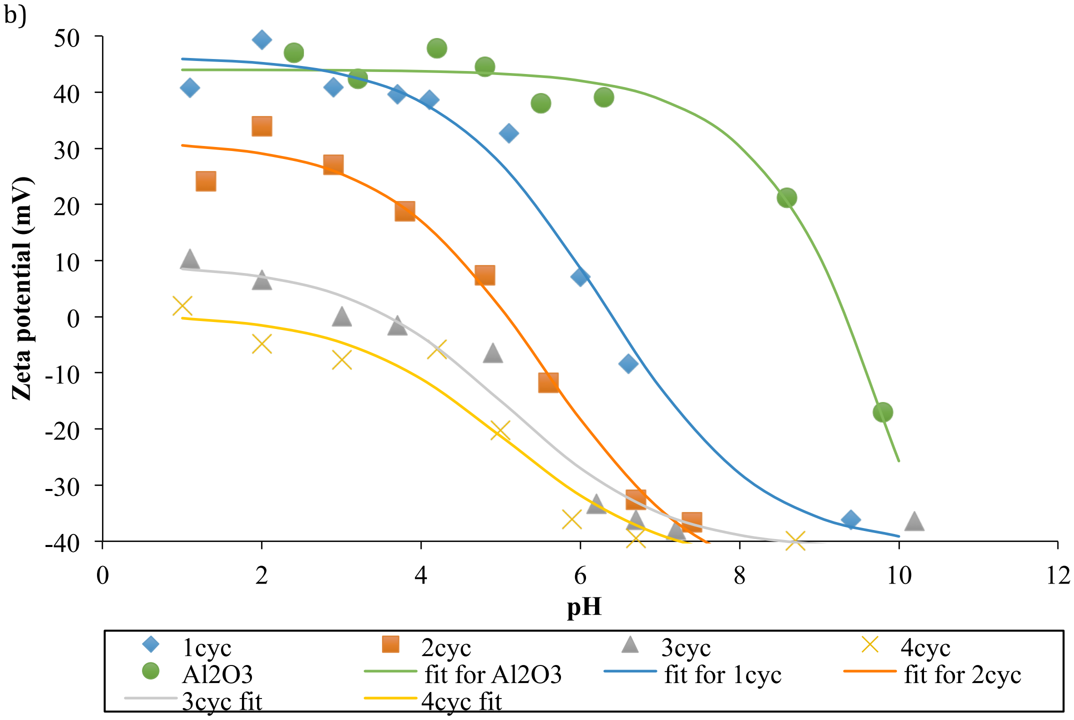

Figure 4.3.3. The Zeta potentials Vs. pH curves for a) Support materials deposited with 1 to 4 cycles of SiO_2 without templates, b) Support materials deposited with 1 to 4 cycles of SiO_2 having templates pre-grafted. Both experimental data and fitted curves (using built-in function in Matlab®) are plotted, the IEP is extrapolated as the pH where the fitted curve crosses zero zeta potential.

Table 4.3.2. Summary of estimated IEPs for supports

Supports	Cycles of SiO2 deposition	IEP
Al_2O_3	0	9.4
Al_2O_3 1c	1	6.1
Al_2O_3 1ct	1	6.4
Al_2O_3 2c	2	5.1
Al_2O_3 2ct	2	5.1
Al_2O_3 3c	3	3.2
Al_2O_3 3ct	3	3.6
Al_2O_3 4c	4	2.4
Al_2O_3 4ct	4	1-2

Pt adsorption experiment

Figure 4.3.4 shows that the amount of Pt adsorbed on the support surface decreases drastically with increasing cycles of SiO_2 deposition. The negatively charged SiO_2 layer causes repulsive interaction with the Pt anion complex and results in less Pt anion complex adsorbed onto the support. Here, precursor solution with pH4 yields sufficient amount of Pt anion adsorption for supports with different cycles of SiO_2 deposition, therefore pH4 is chosen as the pH of precursor solution for future experiments.

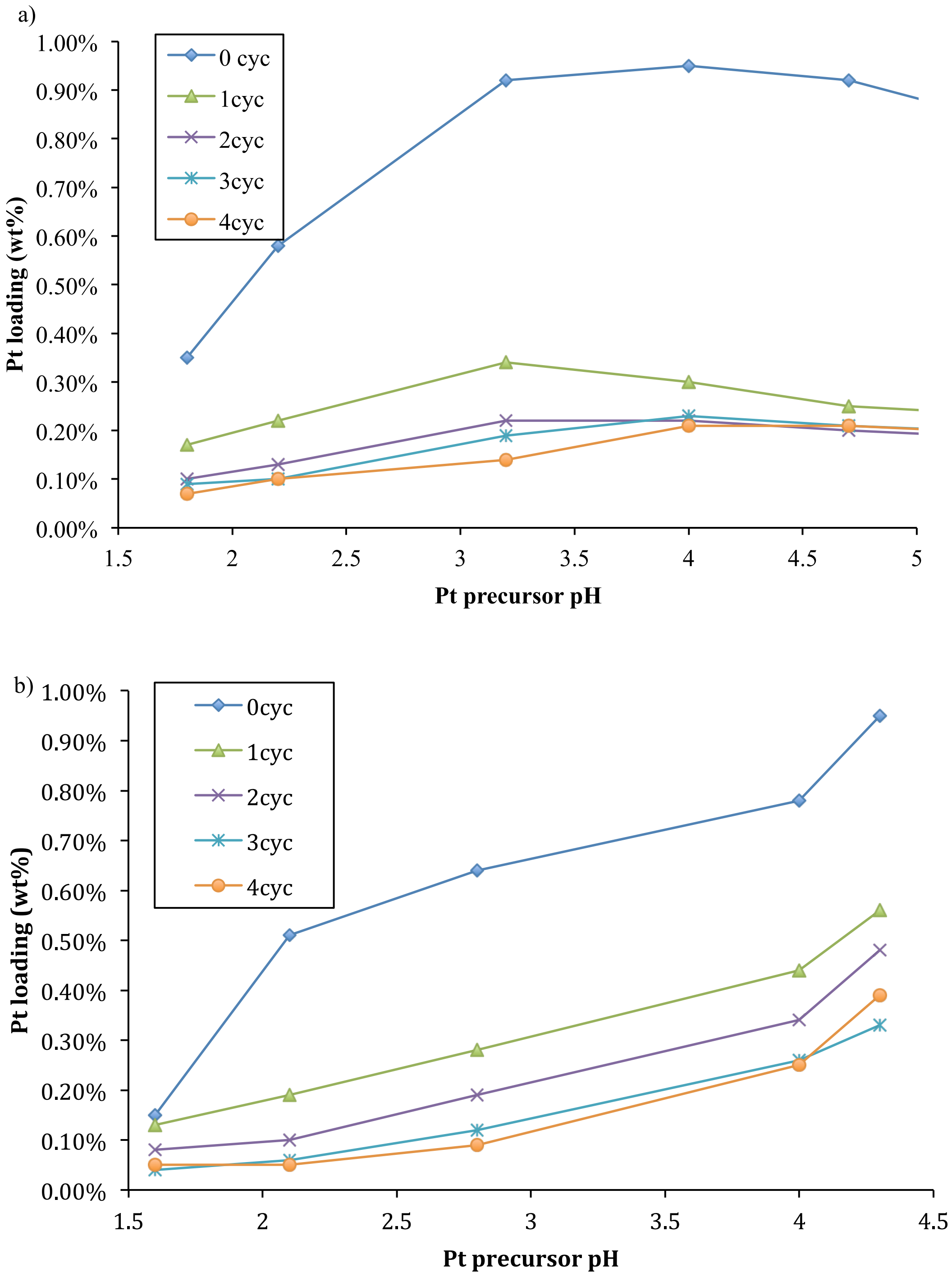

Figure 4.3.4. The Pt loading (wt %) Vs. Pt precursor pH curves for a) Support materials deposited with 1 to 4 cycles of SiO_2 having pre-grafted templates, b) Support materials deposited with 1 to 4 cycles of SiO_2 without templates.

Characterization of supported Pt prepared by SEA

Figure 4.3.5 shows that the Pt loadings decrease from ~1 wt% to ~0.2 wt% for supports with increased cycles of SiO_2 deposition. In particular, significant less amount of Pt was deposited onto the supports without pre-grafted templates at higher SiO_2 deposition cycles. This indicates that the template plays a key role in exposing the underlying support during the SiO_2 overcoating process especially when large amount of SiO_2 is present. For a support without template modification, most of the Al_2O_3 surface is covered with SiO_2 at higher cycles of SiO_2 deposition thus is not available for adsorption of Pt anion complex during the SEA process. While for a support grafted with templates, part of the support surface survives from the overcoating process and is available for Pt adsorption upon removal of templates, therefore can adsorb more Pt ions during the SEA process. No significant number of Pt nanoparticles with size above 1nm can be observed from electron microscope characterization except sample Al_2O_3_Pt suggesting that the Pt atoms are highly dispersed (Representative TEM/STEM images are included in figure 4.3.6). With the assumption that one CO molecule adsorbs onto one surface Pt atom, the CO chemisorption data summarized in table 4.3.3 shows that significant amount of surface Pt atoms are present on the support modified with SiO_2 after Pt deposition process. Nevertheless, the ratios calculated from CO chemisorption further confirm that the Pt atoms on the supports modified with SiO_2 are highly dispersed.

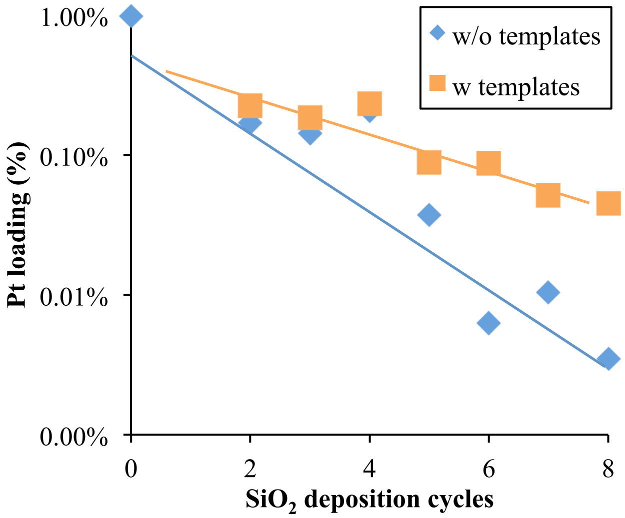

Figure 4.3.5. Pt loading Vs. SiO_2 deposition cycles for all supported Pt samples prepared by SEA approach (Pt on bare Al_2O_3, Pt on Al_2O_3 with 1 to 8 cycles of SiO_2 deposition, Pt on Al_2O_3 with pre-grafted templates and 1 to 8 cycles of SiO_2 deposition (the loading is plotted on logarithmic scale).

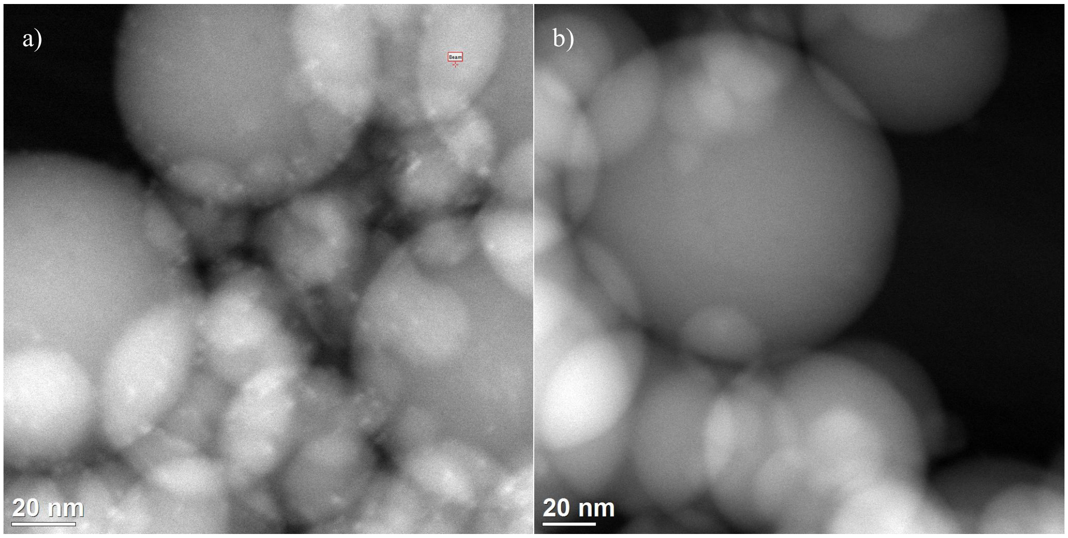

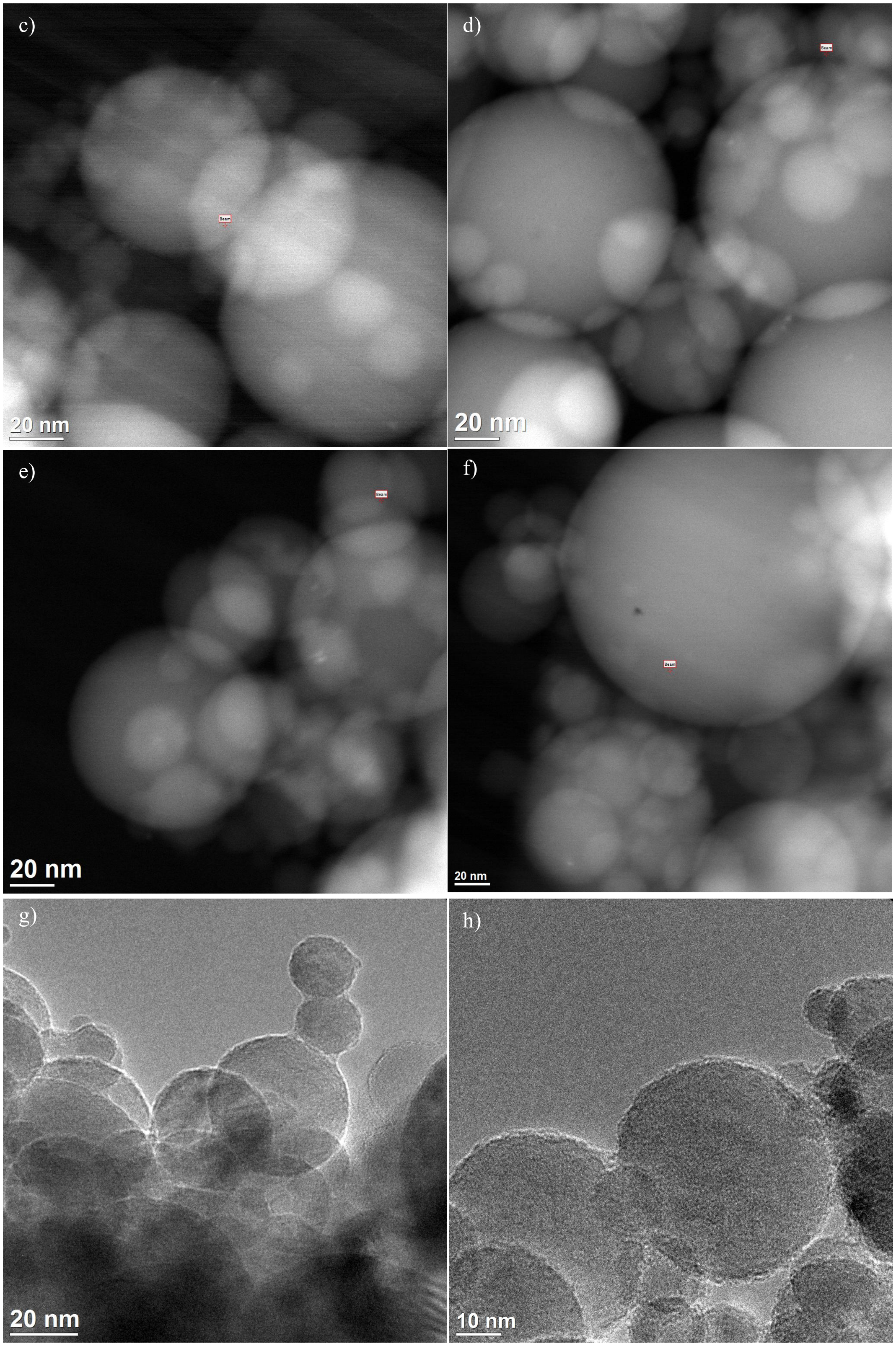
c)
Beam
20 nm
d)
Beam
20 nm
e)
Beam
20 nm
f)
Beam
20 nm
g)
20 nm
h)
10 nm

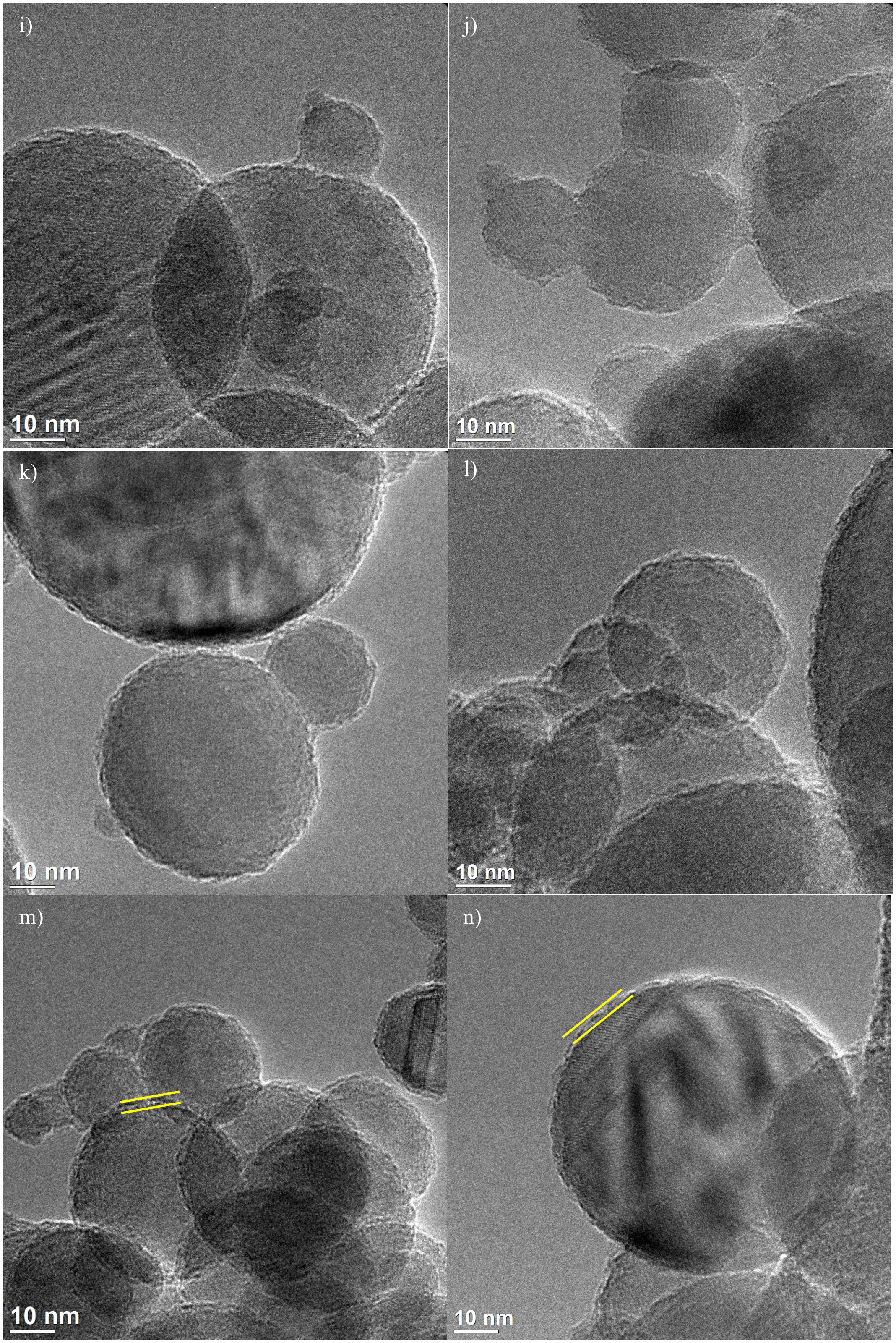
i)
10 nm
j)
10 nm
k)
10 nm
l)
10 nm
m)
10 nm
n)
10 nm

Figure 4.3.6. Representative STEM/TEM images of samples a) Al_2O_3_Pt, b) Pt 2c, c) Pt 2ct, d) Pt 3c, e) Pt 3ct, f) Pt 4c, g) Pt 5c, h) Pt 5ct, i) Pt 6c, j) Pt 6ct, k) Pt 7c, l) Pt 7ct, m) Pt 8c, n) Pt 8ct. The STEM imaging mode is used to characterize highly dispersed small Pt nanoparticles (size ~1nm). TEM images show the uniform SiO_2 overcoat on the AL_2O_3 support surface (highlighted by yellow markers in image m) and n)), which are consistent with the observation in prior work.[42]

Table 4.3.3 Summary of Pt dispersion data from CO chemisorption

Samples	Surface CO to total Pt atoms ratio
Al_2O_3_Pt	75%
Pt 2c	107%
Pt 3c	115%
Pt 4c	106%
Pt 2ct	113%
Pt 3ct	114%
Pt 4ct	97%

Given that the structural information of Pt atoms (<1nm) provided by electron microscope characterization is limited, CO-FTIR is utilized to study the coordination of the Pt atoms on the support. CO-FTIR has been extensively used in prior research to study the coordination of Pt atoms on the support surface post synthesis.[54, 101, 102] The IR peak around 2120 cm^{-1} corresponds to a linear CO molecule adsorbed onto an isolated Pt atom and the peak around 2070 cm^{-1} corresponds to CO adsorbed on a Pt atom in a nanoparticle (figure 4.3.7). IR spectrums in figure 4.3.8 show the existence of isolated Pt atoms in Pt supported on unmodified Al_2O_3 support and Pt supported on Al_2O_3 overcoated with significant amount of SiO_2 deposition (>= 4cycles). The shift of IR peak for samples Pt 2c and Pt 2ct from 2070 cm^{-1} to 2050 cm^{-1} can be attributed to the combined effect of change in coordination of Pt atoms and interaction between Pt atoms with the Al-O-Si interface.[54, 103]

The ratio between isolated Pt atoms and total amount of Pt atoms for each sample is estimated using the the peak intensity of CO peak for the isolated Pt atom (2120 cm^{-1}) and the sum of peak intensities of all CO peaks. Figure 4.3.9 suggests that when the Al_2O_3 surface is pre-grafted with templates then overcoated with increasing cycles of SiO_2, the as deposited Pt atoms tend to form isolated sites on the support surface (the ratios are summarized in table 4.3.4).

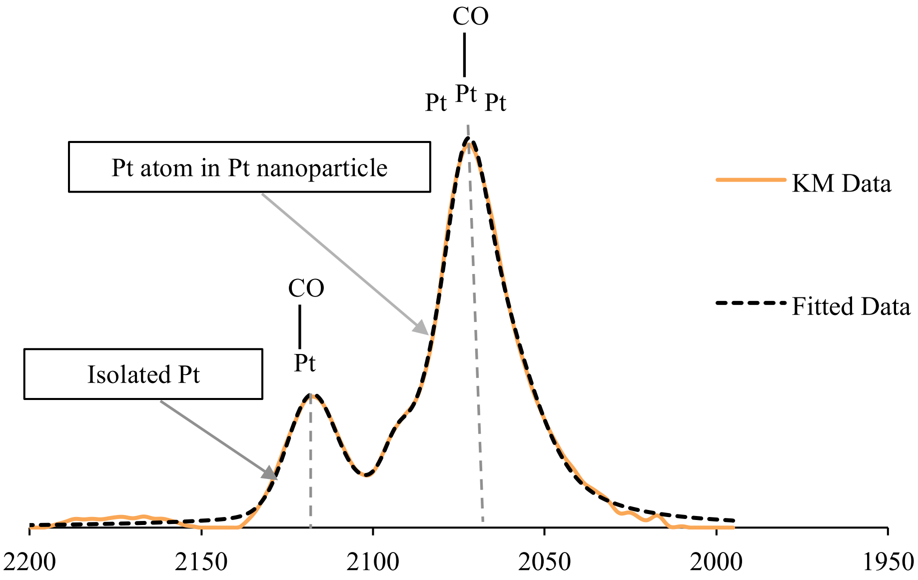

Figure 4.3.7. CO-FTIR spectrum of sample Pt 8ct for demonstrating the peak of a CO molecule adsorbed onto an isolated Pt atom and the peak of a CO molecule adsorbed onto a Pt atom in Pt nanoparticle.

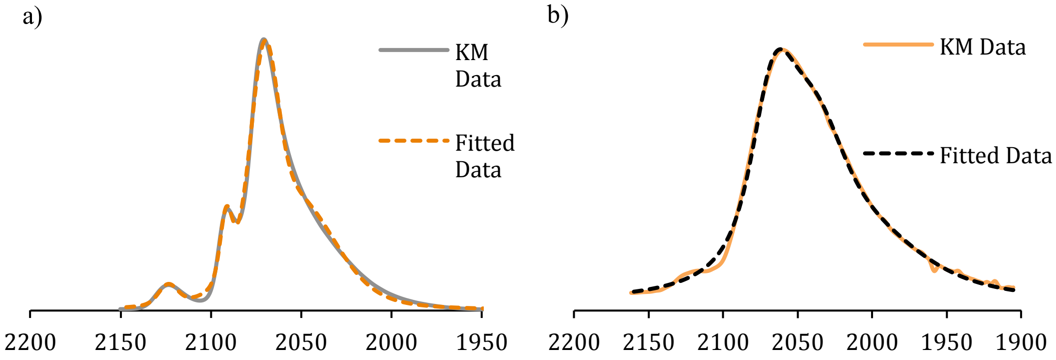

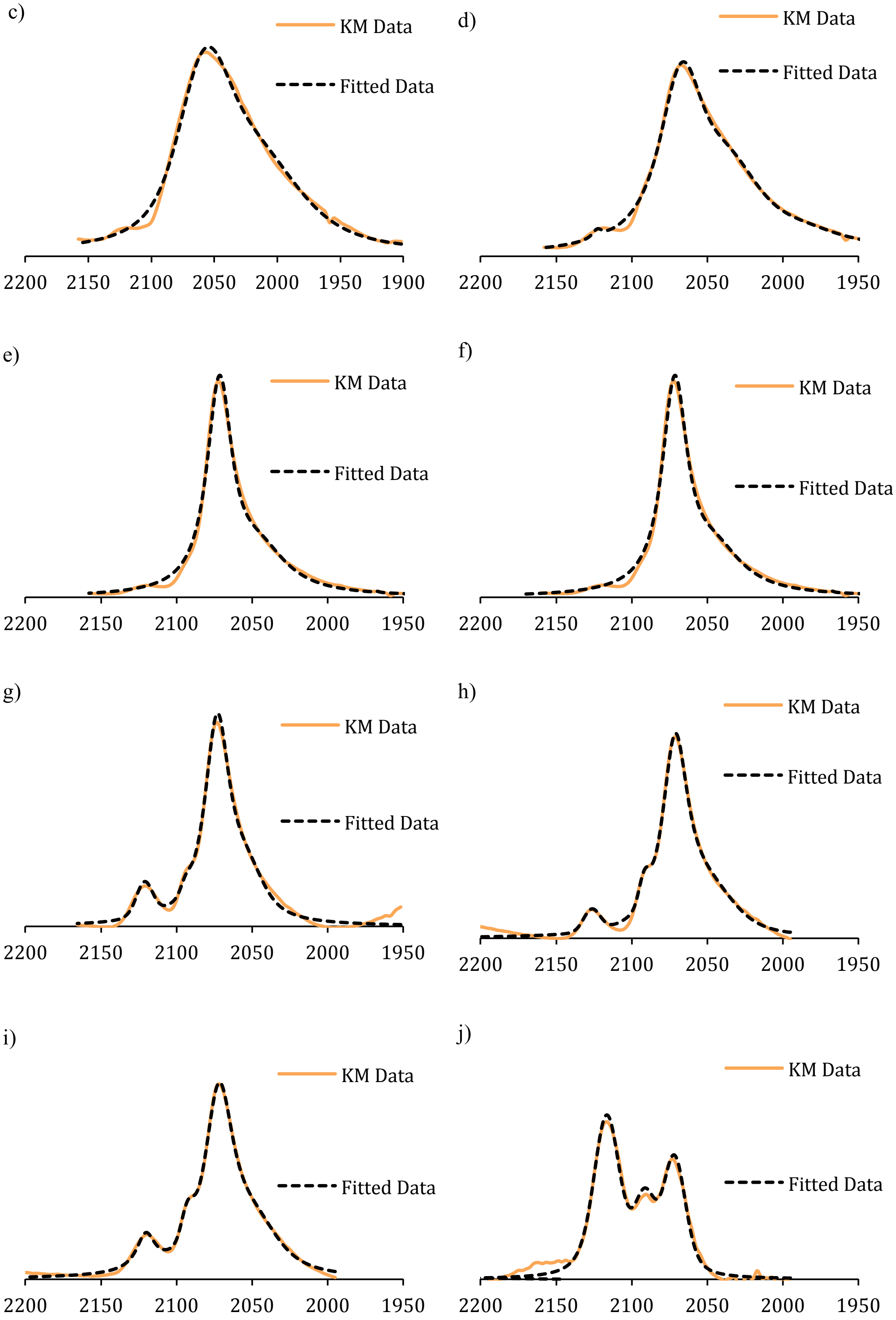
c)
KM Data
Fitted Data
2200
2150
2100
2050
2000
1950
1900
d)
KM Data
Fitted Data
2200
2150
2100
2050
2000
1950
e)
KM Data
Fitted Data
2200
2150
2100
2050
2000
1950
f)
KM Data
Fitted Data
2200
2150
2100
2050
2000
1950
g)
KM Data
Fitted Data
2200
2150
2100
2050
2000
1950
h)
KM Data
Fitted Data
2200
2150
2100
2050
2000
1950
i)
KM Data
Fitted Data
2200
2150
2100
2050
2000
1950
j)
KM Data
Fitted Data
2200
2150
2100
2050
2000
1950

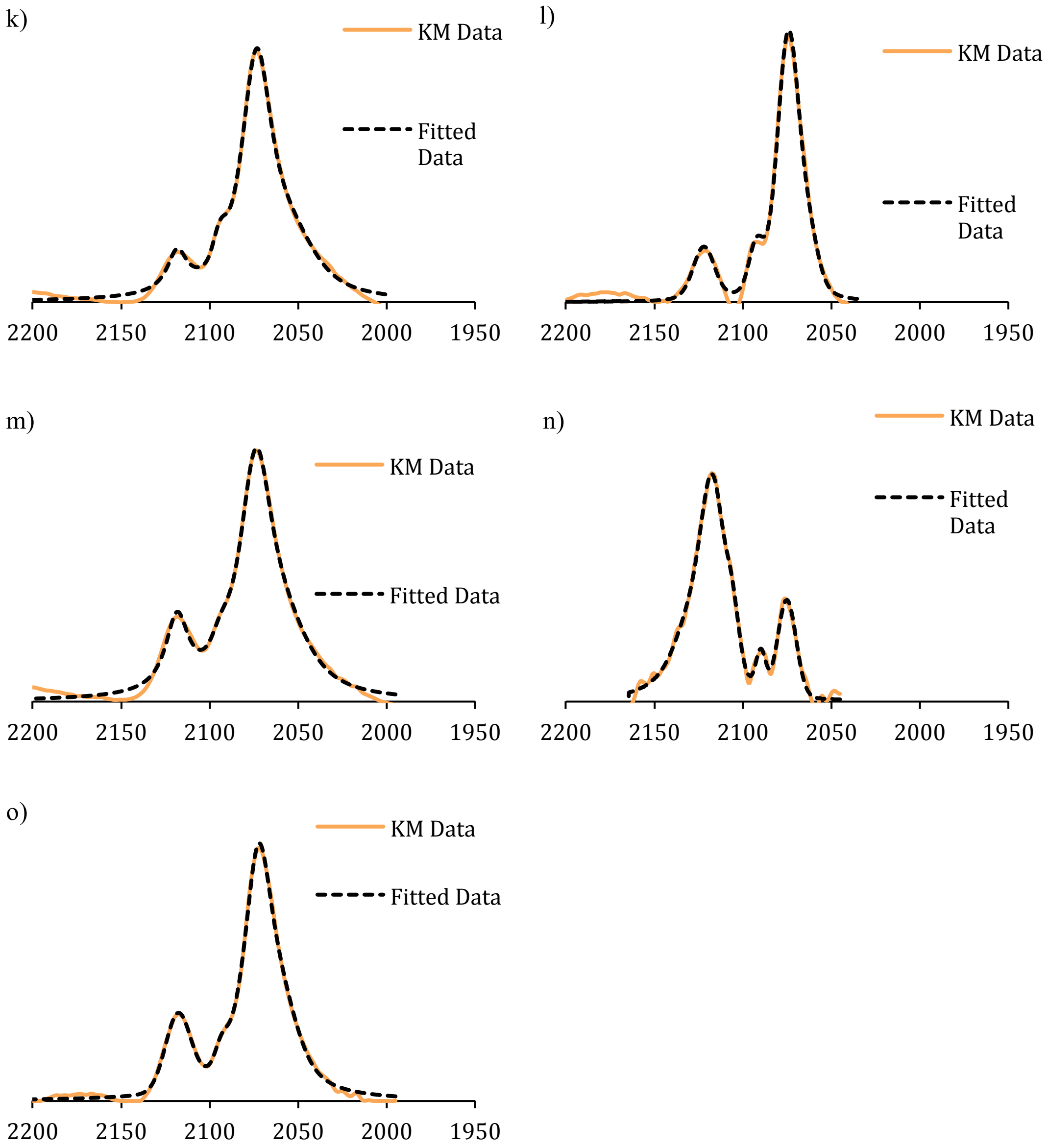

Figure 4.3.8. CO-FTIR results of a) Al_2O_3_Pt, b) Pt 2c, c) Pt 2ct, d) Pt 3c, e) Pt 3ct, f) Pt 4c, g) Pt 4ct, h) Pt 5c, i) Pt 5ct, j) Pt 6c, k) Pt 6ct, l) Pt 7c, m) Pt 7ct, n) Pt 8c, o) Pt 8ct.

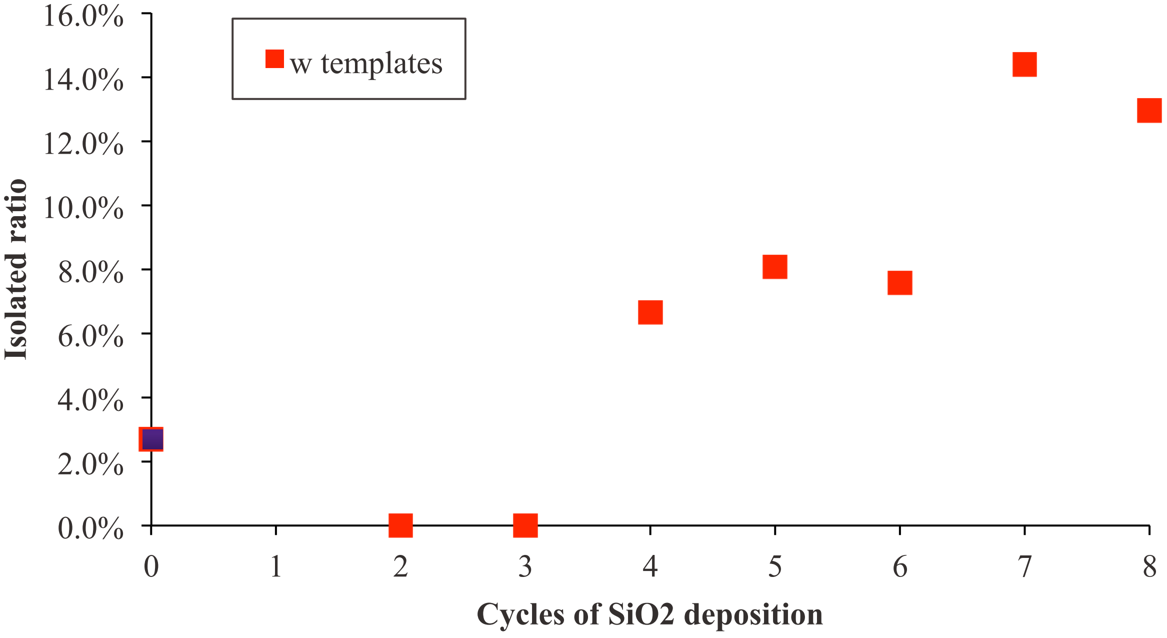

Figure 4.3.9. Plot of ratios between the peak intensity of CO on isolated Pt atom and the sum of peak intensities of CO on all Pt atoms Vs. Cycles of SiO_2 deposition (red squares for the support with template modification and purple square for bare support).

Table 4.3.4 Summary of ratios between the peak intensity of CO on isolated Pt atom and the sum of peak intensities of CO on all Pt atoms

	Isolated CO to total CO ratio	
Cycles of SiO_2 deposition	**w templates**	**w/o templates**
0		2.7%
2	0.0%	0.0%
3	0.0%	0.6%
4	6.6%	0.0%
5	8.1%	3.4%
6	7.6%	46.7%
7	14.4%	13.4%
8	12.9%	69.4%

Propylene hydrogenation study

Selected samples were tested in propylene hydrogenation reaction to understand whether the support modification process or the Pt deposition process changes the catalytic activity of Pt. Two samples (Pt 4c wi and Pt 4ct wi) were prepared by wetness impregnating Pt precursor onto supports with 4 cycles of SiO_2 deposition. Propylene hydrogenation is a structure insensitive reaction, which is not expected to exhibit catalytic activity dependence on the size of the Pt metal particle or the type of the support. The reactivity data in table 4.3.5 shows that the reactivity of Pt atom on the supports modified with SiO_2 is comparable to the Pt atom on the unmodified Al_2O_3. The Pt atoms show very similar catalytic behaviors on the Al_2O_3 support modified with 4 cycles of SiO_2 deposition regardless of Pt deposition methods, suggesting preparation methods do not affect the catalytic activity of as deposited Pt atoms. The plots of conversion Vs. time on stream for samples Pt_Al_2O_3 and Pt 4ct are shown in figure 4.3.10. The catalyst deactivates over time under these reaction conditions, as is typical for hydrogenation, but the catalyst regains its activity after oxidative treatment, indicating the reactivity loss is primarily due to light coking or deposition of other carbonaceous groups.

Table 4.3.5. Summary of Propane hydrogenation reactivities

Sample	**Pt loading (wt%)**	**Propane production rate TOF (mol mol_{pt}^{-1} sec^{-1})**		**Propane Production rate (mmol $g_{catalyst}^{-1}$ sec^{-1})**	
		Initial[a]	**5hr**	**Initial**	**5hr**
Pt_Al_2O_3	0.98	179± 21[b]	110± 19[b]	9± 1	5.5± 0.9
Pt 4c	0.21	101± 49	34± 11	1± 0.4	0.3± 0.1
Pt 4ct	0.23	105± 30	28± 7	1.2± 0.2	0.3± 0.1
Pt 4c wi	0.18	210± 125	62± 41	1.9± 1.1	0.6± 0.4
Pt 4ct wi	0.16	141± 54	45± 25	1.2± 0.44	0.4± 0.2

[a] Initial point was taken at 1 hour after the reaction starts

[b] Error in the data stands for standard deviation of three independent runs.

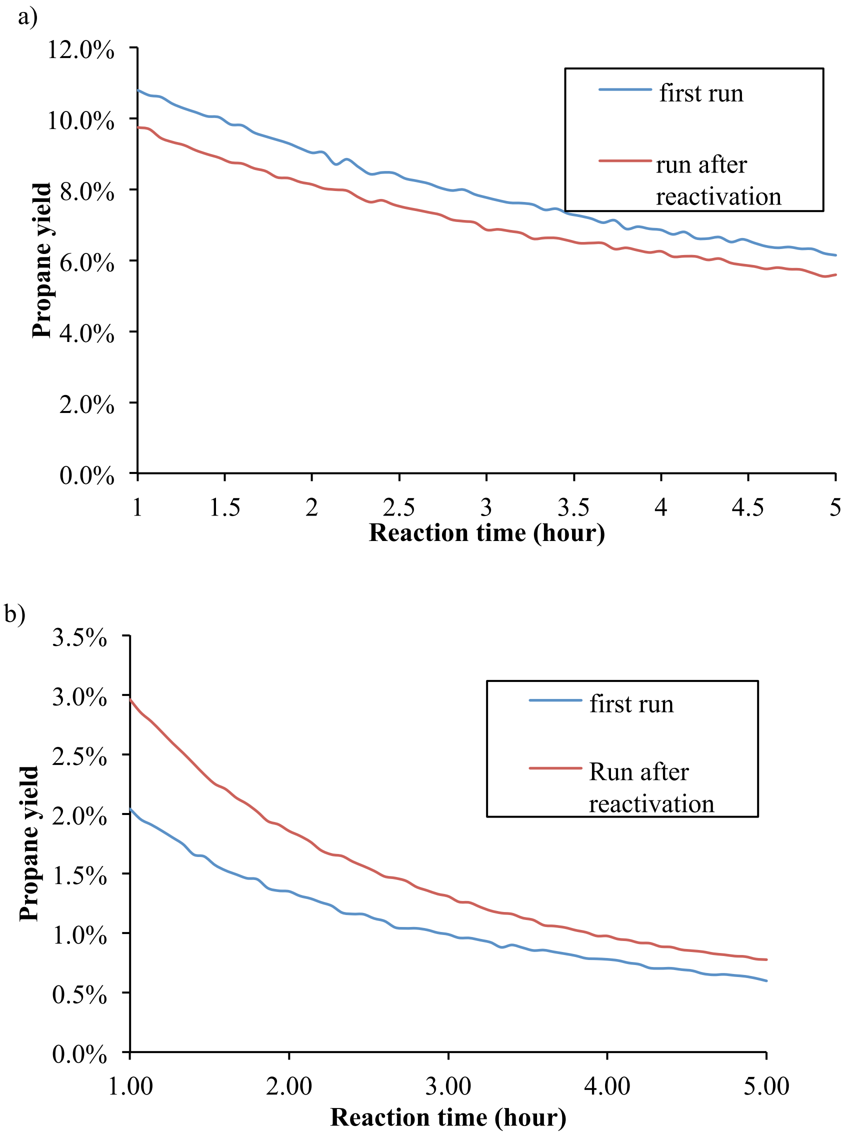

Figure 4.3.10. Propane yield Vs. upstream time plots for Propylene hydrogenation at 50 °C a) Pt_Al_2O_3, b) Pt 4ct. Samples were regenerated in 10%O_2/He at 250 °C for 1 hour. The recovery of reactivity after regeneration indicates that the loss of reactivity is primarily by coking or deposition of other carbonaceous groups.

4.4 Conclusion and Future work

This work demonstrates that the combined use of partial overcoat and SEA allows deposition of highly dispersed Pt onto Al_2O_3 support. Increasing amount of SiO_2 deposited onto Al_2O_3 lowers the IEP of the support material and decreases the number of available adsorption sites during SEA process. Electron microscope characterization and CO chemisorption study show that the Pt deposited on Al_2O_3 surface overcoated with SiO_2 are highly dispersed. Further CO-FTIR study reveals that increasing the amount of SiO_2 deposited onto the support surface with pre-grafted templates increases the ratio of isolated Pt atoms after synthesis. Finally, the propylene hydrogenation reaction study shows the SiO_2 overcoat and deposition method do not change the catalytic behavior of the Pt. In conclusion, the combined use of SEA and sol-gel oxide overcoating method enables deposition of highly dispersed Pt atoms on Al_2O_3 with propylene hydrogenation reactivity of Pt preserved.

In the future, these materials can be used for structure sensitive reaction study such as CO oxidation, which exhibits particle size dependent reactivity behavior. Other supported metal catalysts such as Al_2O_3 supported Pd catalyst can also be prepared using the similar strategy, which utilizes SEA of metal precursor and sol-gel oxide overcoating process.

Chapter 5

Highly Dispersed TaO_x Catalysts Via A Nanocavity Approach

5.1 Introduction

A significant challenge in supported oxides of all types is characterizing them with atomic precision. Historically, characterization of the active sites of supported oxide catalysts has been via probe reactions and via X-ray absorption, UV-visible, NMR, vibrational, and other spectroscopies.[104-108] However, these techniques all give average properties, making it challenging to tease out the finer details of synthesis-structure-function relationships.

Significant advances have been made in recent years for the direct, atomic-level visualization of supported catalyst active sites by electron microscopy, even as the active sites themselves trend towards single-atom dimensions.[101, 109] However, there remain several significant limitations that have prevented its application to the structures most relevant to supported oxide catalysts. First, the successes in imaging of highly-dispersed catalysts via transmission electron microscope and scanning transmission electron microscopy have focused on low-valent, late transition metal clusters and atoms (eg. Au, Pt, Ir),[101, 109, 110] rather than supported high-valent early transition metal cations and oxides. Second, zeolites and certain other crystalline oxides have been preferred for atomic-resolution imaging of supported species.[88] However, it is much more challenging to image species with atomic resolution on the surface of more traditional supports such as Al_2O_3, TiO_2 and SiO_2 because of their amorphous or highly faceted surfaces, making it impossible to focus highly converged electron beams on more than a small area at a time.

In this study, we report the use of 2D TiO_2 nanosheets ($nsTiO_2$) as nearly ideal materials for the direct visualization of highly-dispersed, supported oxides, in this case tantalum oxides (TaO_X/TiO_2). The use of thin (<10nm thick), flat, anatase TiO_2 nanosheets instead of traditional oxide particle supports makes it possible to keep the entire surface in focus during High-Resolution High Angle Annual Dark-Field (HAADF) imaging, rather than very small regions on a particle edge, as is required for conventional supports. Moreover, in contrast to STM, which has long enabled atomic-scale resolution of oxides,[12, 111] or atom-probe tomography, which has recently allowed these types of insights, [112] high surface area powders are used here, permitting bulk characterization tools to be used on the same material with no special modifications. Second- and third-row highly dispersed metal oxides are less commonly used than their first-row counterparts, but have recently gained attention for having comparable, or in many cases greater, activity or selectivity in a variety of thermochemical transformations.

The images provide direct evidence for single-atom dispersion and the distribution of Ta-Ta nearest-neighbor distances over a wide area, giving insight into sensitivity of the TaOx structure on the synthesis precursor and post-synthesis modification by atomic layer deposition. Precursor and post-synthesis modification have both been shown to strongly influence the catalyst activity and stability,[68, 113, 114] but as mentioned above, direct connections to surface speciation have remained elusive.

5.2 Experiment

General remarks: Unless otherwise noted, all materials in this study were synthesized using standard air-free Schlenk line and glove box techniques. Tantalum precursors ($TaCl_5$, $Ta(OEt)_5$) were obtained at the highest possible purity from Strem Chemicals. p-*Tert*-butylcalix[4]arene ("calix") was received from Sigma Aldrich (95%). All metal precursors were stored in an Ar glovebox and used as-received. Toluene was distilled over CaH_2 and degasified using standard techniques. TiO_2 supports (nanosheets ("nsTiO_2") were dehydrated at 110°C under dynamic vacuum (<30 mTorr) for 5 hours prior to use in synthesis. Synthesis apparatuses and sample storage containers were wrapped in aluminum foil and stored in the dark to prevent exposure to ambient light.

Materials Synthesis

Synthesis of TiO_2 nanosheet support (sample: nsTiO_2): nsTiO_2 were synthesized using a previously published hydrothermal synthesis protocol.[115, 116] Briefly, 2.8 mL of concentrated hydrofluoric acid (48 wt% solution, >99%, Macron) was added to 20 mL of titanium butoxide (97%, Sigma-Aldrich) in the PTFE liner of an autoclave vessel and was allowed to stir for 30 minutes. [CAUTION: concentrated hydrofluoric acid is an extremely corrosive contact poison and should be handled and stored with extreme care.] The autoclave vessel was then sealed and placed in a 200°C oven for 24 hours. The resulting solids were washed and centrifuged 3 times in ethanol (200 proof, Sigma-Aldrich), then washed and centrifuged in ultra-pure water until the pH of the centrate reached approximately 5. The solids were then washed and centrifuged 3 times in a solution of 0.1 M NaOH, then washed and centrifuged again several times with 18.2

M$\Omega\cdot$cm^{-1} water until the pH of the centrate was below 8. Finally, the nsTiO_2 solids were allowed to dry in air in a 60°C oven overnight.

Grafted materials from Ta-calix[4]arene ("Ta-calix") precursor (sample: Ta-Calix): Following protocols previously published by some of us,[117, 118] 1.2 mmol $TaCl_5$ was added to a 40 mL toluene suspension of 1.2 mmol p-*tert*-butylcalix[4]arene inside of an Ar glovebox. The reaction flask was equipped with a magnetic stirbar, sealed, and transferred to a Schlenk line under N_2 flow. A reflux condenser was attached, and the flask's contents were refluxed for 14 h. The suspension was cooled to 80°C, and discrete 5.0 mL volumes were syringe-transferred under N_2 purge to flasks containing variable amounts of a dehydrated TiO_2 support; the resulting solution concentrations were 0.1-0.5 Ta-calix complexes per nm^2 support surface area (see main text). The suspension was refluxed for 24 h, after which the solids were vacuum-filtered in air, washed with anhydrous toluene and dried under dynamic vacuum (<30 mTorr) for >24 hours. Some materials were then subjected to atomic layer deposition (ALD; see section below). Materials with and without additional ALD treatment were further treated with ozone at 110°C for 3 h at a ramp rate of 15°C min^{-1} prior to microscopy and catalysis.

Grafted materials from $Ta(OEt)_5$ precursor (sample: Ta-Et) : 0.15 mmol $Ta(OEt)_5$ was added to a 10 mL toluene suspension of variable amounts of TiO_2 support inside of an Ar glovebox; synthesis. A magnetic stirbar was added to the flask, which was then sealed and transferred to a Schlenk line under N_2 purge. A reflux condenser was attached, and the contents were refluxed for 20 h. The solids were vacuum-filtered in air and washed with anhydrous toluene (200 mL) before drying under dynamic vacuum (<30 mTorr) for >24 h. Some solids were then subjected to further ALD treatment (see section below). Materials with and without ALD post-treatment were subjected to ozone treatment at 110°C for 3 h at a ramp rate of 15°C min^{-1} prior to imaging and catalysis.

Atomic layer deposition (ALD) of Al_2O_3 overcoats (sample: Ta-ALD): Thin films of Al_2O_3 were grown using atomic layer deposition (ALD) reactions performed in a custom flow reactor with a stainless steel bed.[119] The reactor operated at 100°C with pressure maintained between 1.0-2.0 Torr using ultra-high purity N_2 carrier gas. Alternating doses of trimethylaluminum (TMA, 99.7%, Sigma-Aldrich) and 18.2 $M\Omega \cdot cm^{-1}$ water were used to create a series of self-limiting reactions.[120] [CAUTION: TMA is pyrophoric and should be handled and stored with extreme care.] One reaction cycle of TMA/H_2O consisted of the following protocol: (a) dosing TMA for 300 s; (b) purging TMA for 300 s; (c) dosing H_2O for 300 seconds; (d) purging H_2O for 300 s.

Scheme 5.2.1. Modification of anatase 001-terminated TiO_2 nanosheets with Ta and Al_2O_3 overcoats[a]

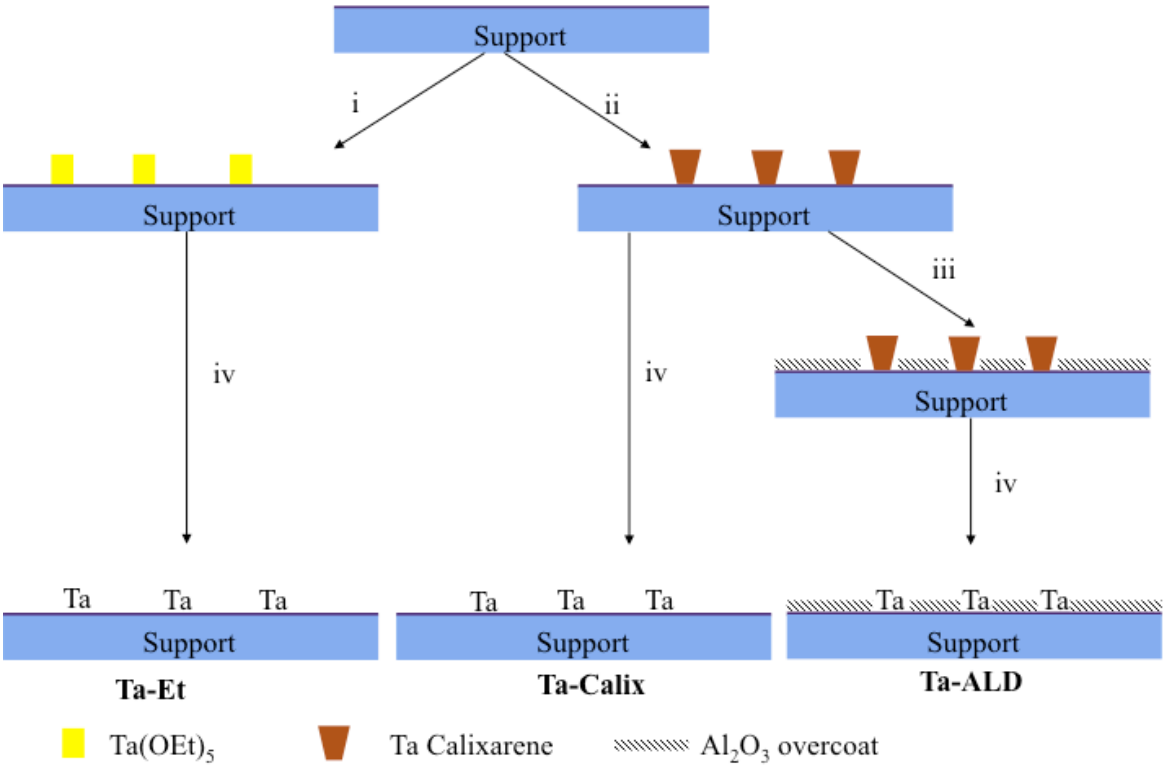

[a] synthetic steps: i) graft $Ta(OEt)_5$ from toluene, reflux 24h; ii) graft calixarene-TiCl from toluene, reflux 24h; iii) atomic layer deposition of 5 cycles of $Al(CH_3)_3$ and H_2O; iv) treatment in O_3 at 110°C.[121]

Physical Characterization

The regular TEM images were acquired using the JEOL JEM-2100 FasTEM operated at 200kV. The single Ta atom on TiO_2 high-angle annular dark field (HAADF) images were acquired using the JEOL JEM-ARM200CF aberration corrected 200kV STEM/TEM. To prepare the samples for imaging, <5mg of samples were dispersed in the ethanol solvent (~3ml) then sonicated to have a homogeneous mixture. Then a few drops of the mixture were drop casted onto a lacey carbon copper TEM grid and air-dried. The post-imaging analysis were completed using ImageJ software, the nearest neighbor distance (NND) was calculated using the Nnd plugin provided by Cooperative Computing Group at Center for Advanced Vehicular Systems at Mississippi State University. The X-ray diffraction pattern was acquired by the Rigaku Ultima PXRD instrument at 40kV. The XPS analysis was completed using the Thermo Scientific ESCALAB 250Xi XPS instrument. The Raman spectrum was acquired using the Acton TriVista CRS confocal Raman spectroscopy equipped with a 514.5 nm 2018 model gas laser in room temperature. The surface area of the nanosheets were determined using a Micrometrics ASAP 2010 with specific surface areas calculated using the Brunauer−Emmett−Teller (BET) method. Thermogravimetric analysis (TGA) was carried out using a TA Instruments Q500 under 90%/ 10 % O_2/N_2. Mass loss between 300 °C and 800 °C is assigned to the combustion of the grafted calixarene template and used to calculate the template loading. Ta loading was determined using a Thermo iCap7600 ICP-OES with sample digestion in a mixture of HF and aqua regia.

5.3 Results and Discussion

Physical characterization

The N_2 physisorption specific surface area of $nsTiO_2$ measured (Figure 5.3.1) by the BET method is 145 m^2/g. These materials consist of platelets with typical particle dimensions of length and width below 100nm and height below 10nm (Figure 5.3.2). These materials have pure anatase phase, with X-ray diffraction peaks corresponding to the (101), (004), (200), (105) and (211) crystal planes (Figure 5.3.3). [122] The grafted Ta atoms has a surface density of ~0.3 Ta nm^-

^{2}, or 70 μmol Ta g^{-1} as determined by thermogravimetric analysis (calixarene ligand content, Figure 5.3.4) and ICP-OES (Ta content). This loading was chosen because it is approximately the geometrical limit resulting from the large calixarene ligand.[68]

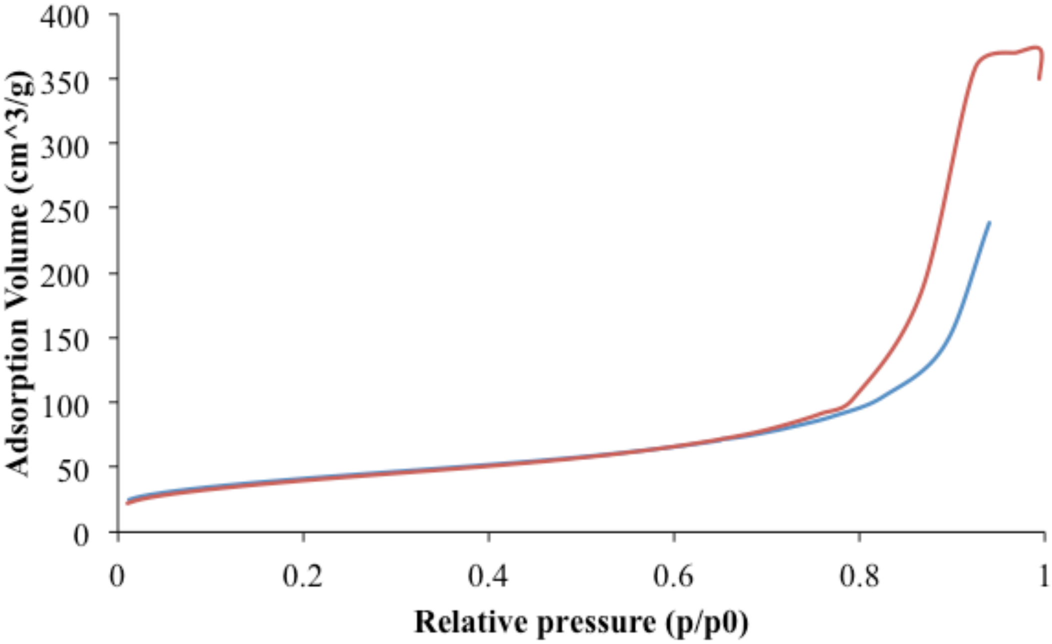

Figure 5.3.1. N_2 adsorption and desorption isothermal curves of as-synthesized **nsTiO$_2$.**

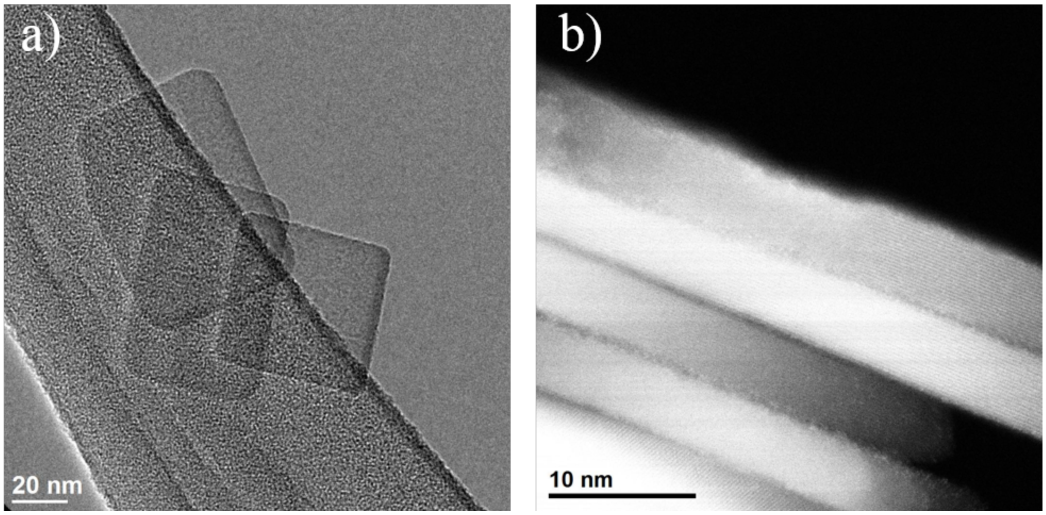

Figure 5.3.2. TEM images of **nsTiO₂** a) obtained using JEOL 2100 FasTEM, b) obtained using JEOL JEM-ARM200CF STEM.

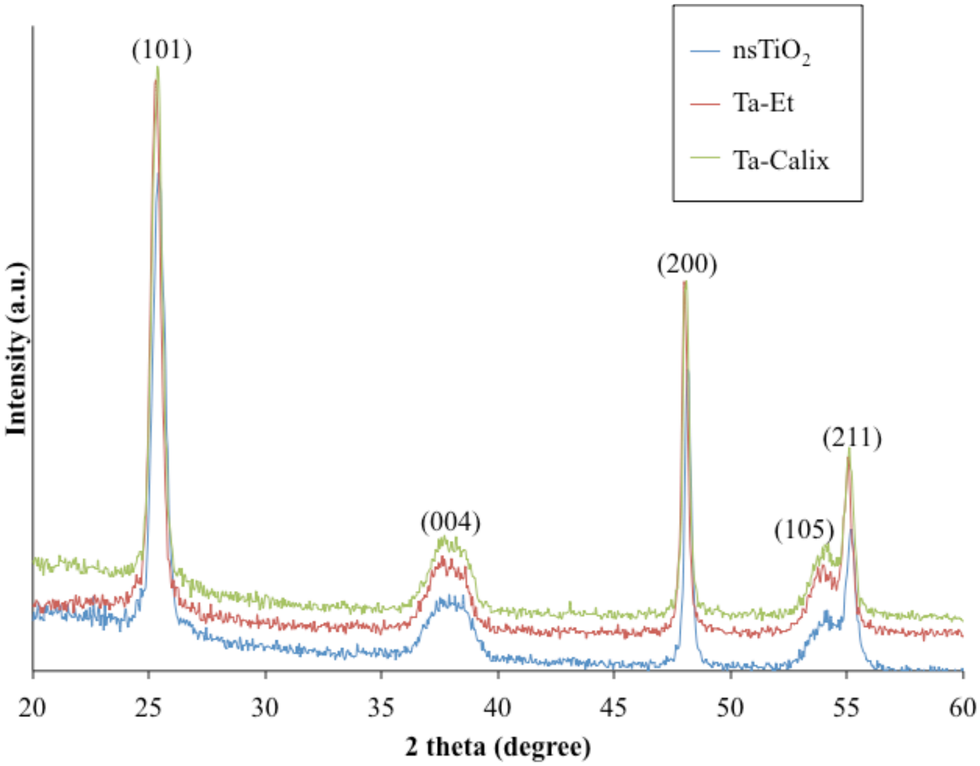

Figure 5.3.3. The XRD patterns of **nsTiO₂** , **Ta-Calix** and **Ta-Et**.

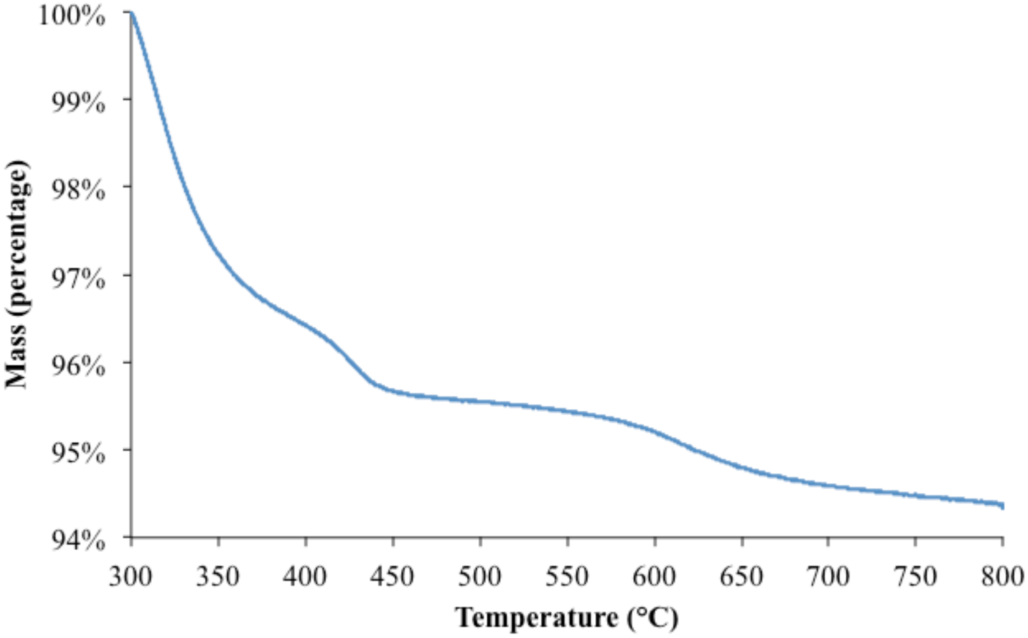

Figure 5.3.4. The TGA curve for **Ta-Calix** materials between 300°C and 800°C.

In addition to electron microscopy, samples were also characterized by XPS, Uv-vis, XRD and Raman spectroscopies. Conventional spectroscopies and other characterization tools are often limited in the information they can provide for mixed or supported oxides, as they often provide ensemble properties of the materials. XRD after Ta deposition or after ALD (Figure 5.3.3) shows no changes or additional features. This indicates that neither did a TaO_x crystal phase form on top of the $nsTiO_2$ nor did Ta insert into the TiO_2 lattice to any significant extent, but it provides no information on the actual TaOx structure taken. XPS spectra (Figure 5.3.5) show binding energy peaks at 458.6 eV and 464.5 eV in the Ti 2p region and at 530 eV in the O 1s region are typical of Ti^{4+} and oxygen ions in metal oxides.[122] The Ta 4f peaks around 25.9 eV and 27.8 eV confirm the presence of Ta with high oxidation states in the Ta-containing samples.[123, 124,125] Raman spectroscopy (Figure 5.3.6) of the Ta-containing materials shows weak and broad features in the region of 900 to 940 cm^{-1} that are attributable to terminal Ta=O bonds found in highly dispersed oxides,[126] while the absence of observable features near 855 cm^{-1} could indicate the absence of Ta-O-Ta bonds that would be found in larger clusters.[126] However, stronger conclusions are precluded by the relatively low loadings of Ta and the strong contribution from nsTiO_2 itself. Likewise, UV-visible spectroscopy is often a useful tool for characterizing supported oxides,[118, 127] but here cannot distinguish the Ta-containing materials from the parent nsTiO_2 (Figure 5.3.7). Overall, XRD, XPS and Raman studies confirm the presence of small amounts of highly dispersed Ta^{5+} oxide on anatase nsTiO_2 but cannot provide further details.

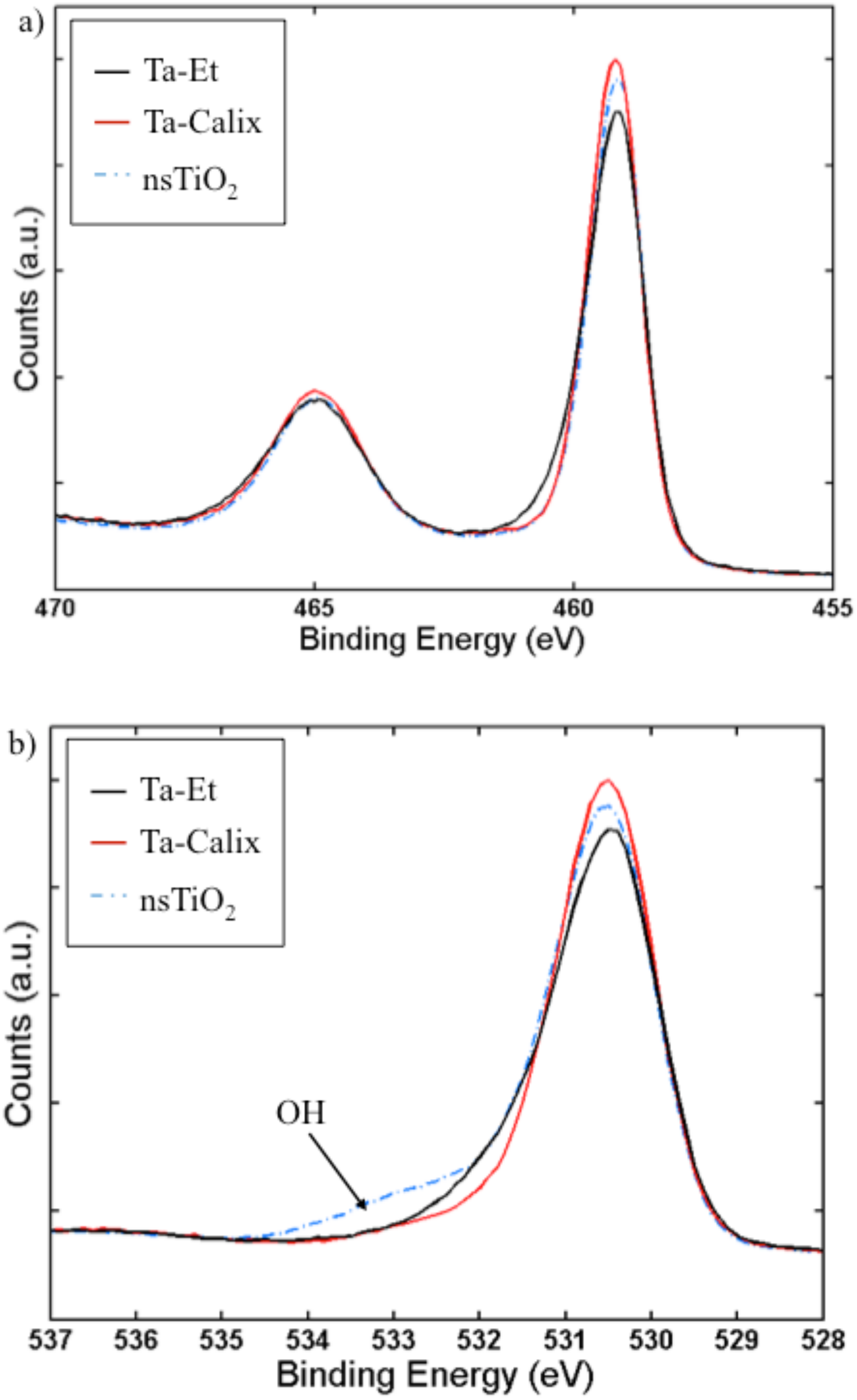
a)
Ta-Et
Ta-Calix
nsTiO$_2$
Counts (a.u.)
470
465
460
455
Binding Energy (eV)
b)
Ta-Et
Ta-Calix
nsTiO$_2$
OH
Counts (a.u.)
537
536
535
534
533
532
531
530
529
528
Binding Energy (eV)

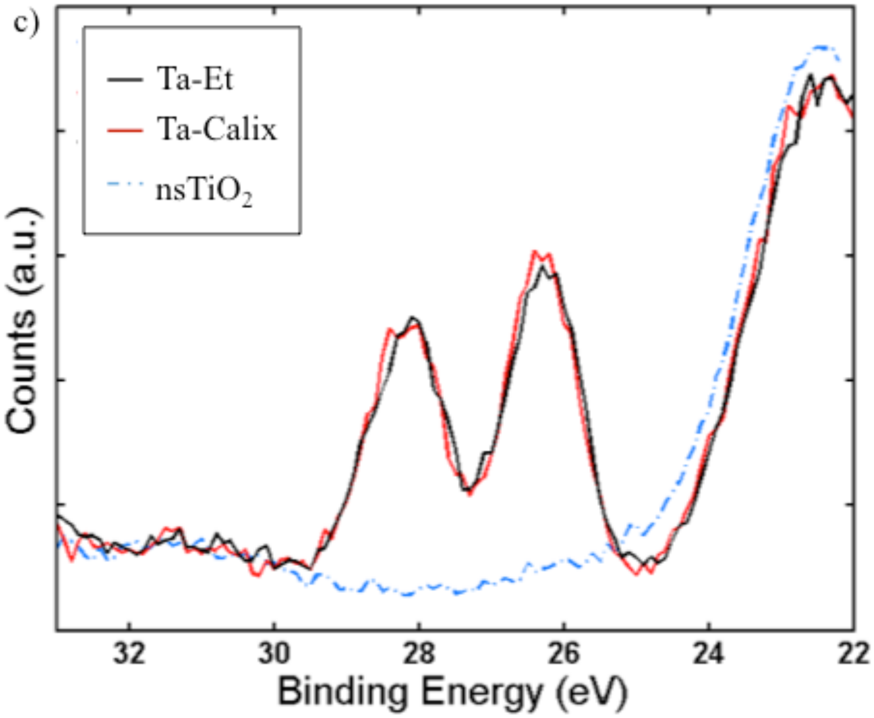

Figure 5.3.5. XPS spectrums of **nsTiO$_2$**, **Ta-Calix** and **Ta-Et** a) Ti 2p, b) O 1s, c) Ta 4f. The peaks are fitted using Matlab® curve fitting function. Shoulder in Oxygen 1s peak of TiO$_2$ ns can be attributed to the hydroxyl groups existing on the surface of TiO$_2$ ns. The binding energy peaks around 530 eV in O 1s region for all three samples can be assigned to Oxygen ions existing in metal oxides. The features at a lower binding energy of ~22 ev can be attributed to O 2s peaks.

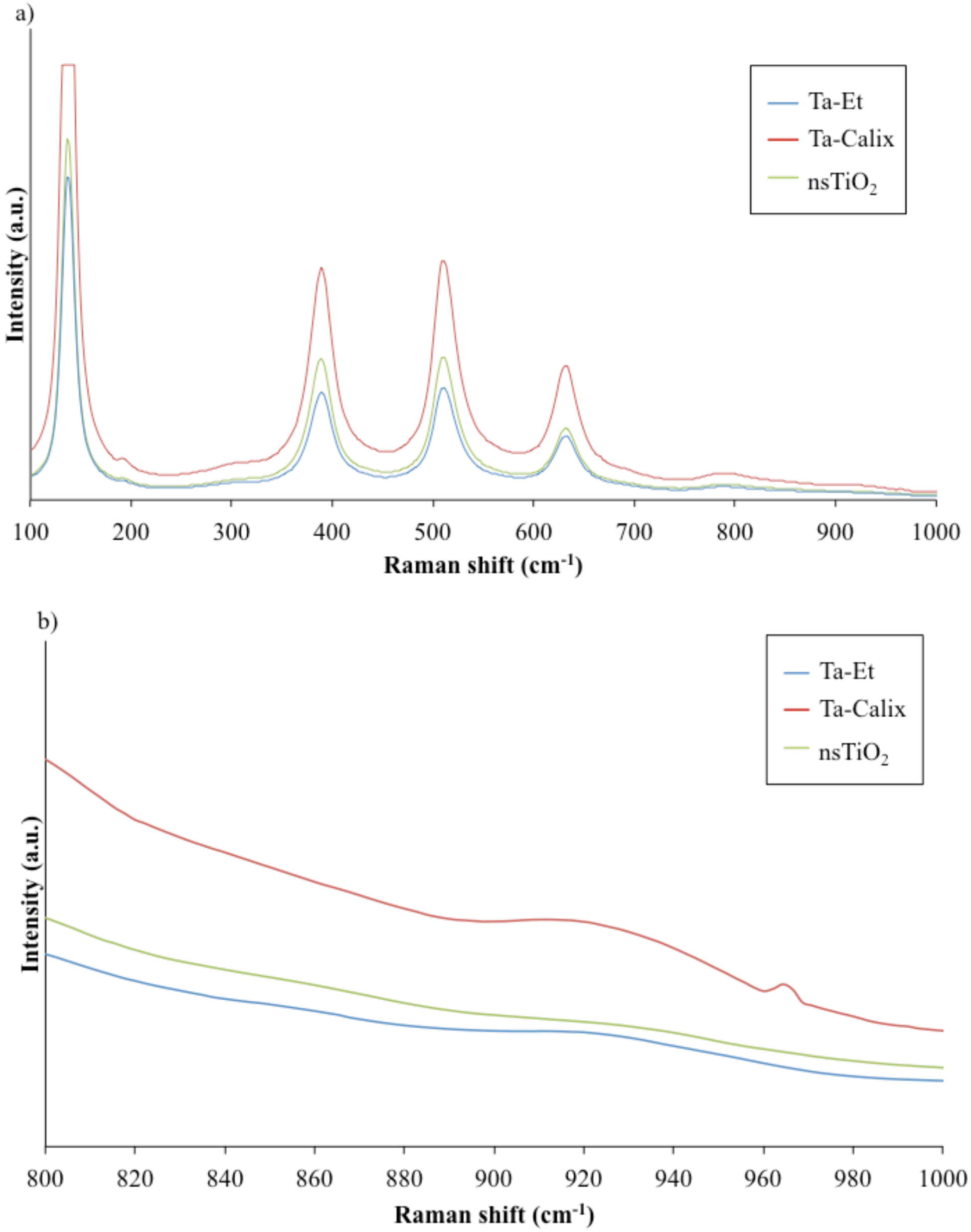

Figure 5.3.6. a) Raman spectrums of **nsTiO$_2$**, **Ta-Calix** and **Ta-Et** in 100 to 1000 cm^{-1} range, b) Raman spectrums of **nsTiO$_2$**, **Ta-Calix** and **Ta-Et** in 800 to 1000 cm^{-1} range, which show the Ta features.

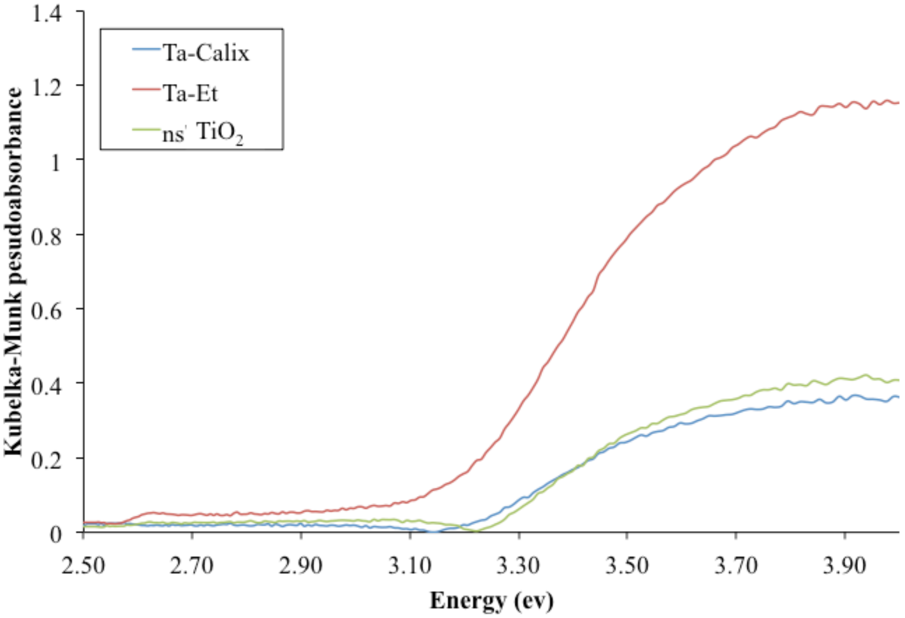

Figure 5.3.7. Diffuse Reflectance Uv-vis characterization of samples **Ta-Calix**, **Ta-Et** and **nsTiO$_2$**.

STEM Characterization

Therefore, High-resolution HAADF-STEM images were acquired to enable direct observation of the distribution of Ta atoms on the TiO$_2$ surface with atomic resolution. Figure 5.3.8 shows the structure of **Ta-Et** taken along the [001] direction of the nsTiO$_2$ crystallite. The image clearly demonstrates that the Ta atoms are located on top of the Ti-O columns, and there were no Ta atoms located between columns. This alignment requires that the Ta atoms were present either directly above the Ti lattice sites, or as substitutions for Ti atoms within the lattice or at the surface. Because of the synthesis method and the mild post-synthesis treatments, it is most likely that Ta grafts directly above the Ti atoms, as illustrated in Scheme 5.2.1. The circles in Figure 5.3.8 highlight some of the many isolated Ta atoms (no Ta atoms at the neighboring lattice position) in this sample. The squares in Figure 5.3.8 show some potential pairs of Ta atoms; such structures are also illustrated schematically in Scheme 1. To the best of our knowledge, this work presents the first direct imaging of supported oxide structures on a high surface area material.

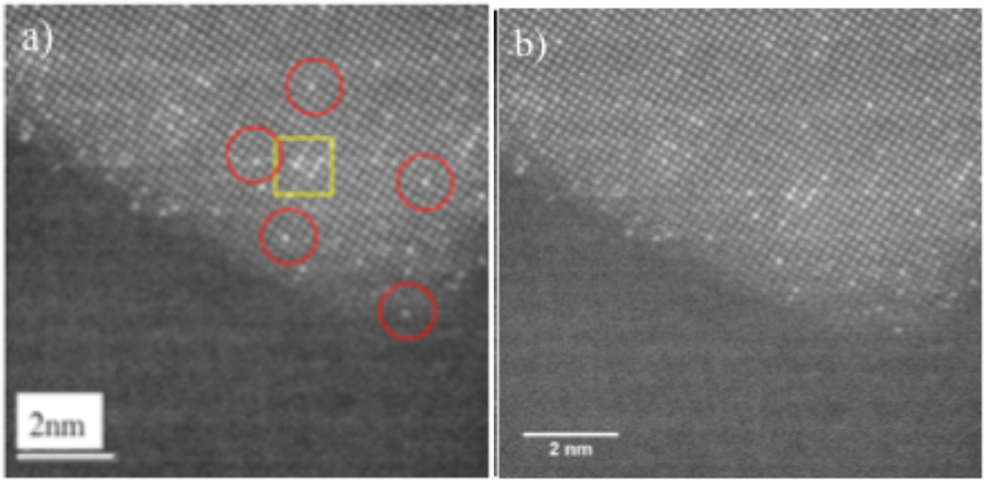

Figure 5.3.8. High-resolution HAADF-STEM images of a) sample Ta_Et acquired along [001] direction of TiO_2 support using a median filter, a median filter with a window of size 2 was applied to this image. The bright dots in the red circles represent individual Ta atoms and the bright cluster in the yellow square represents potential paired Ta atoms. b) The raw image.

Next, the unique ability to locate Ta atoms over longer distances on $nsTiO_2$ is used to map out Ta-Ta distances for other materials. Figure 5.3.9 shows several atomic resolution HAADF-STEM images of **Ta-Et**, **Ta-Calix** and **Ta-ALD**. These images are in plan-view in order to more quickly obtain information about Ta-Ta spacing. Qualitatively, it can be seen that the two Ta precursors, calixarene-TaCl and $Ta(OEt)_5$ do not produce markedly different Ta distributions on the surface with many isolated atoms in both cases. In addition, the Ta distribution is not markedly changed by the ALD overcoating technique. The ALD process utilizes the very reactive molecule $Al(CH_3)_3$ and generates water vapor at moderate temperatures, so the atomic-level stability of the surface has not been known until now.

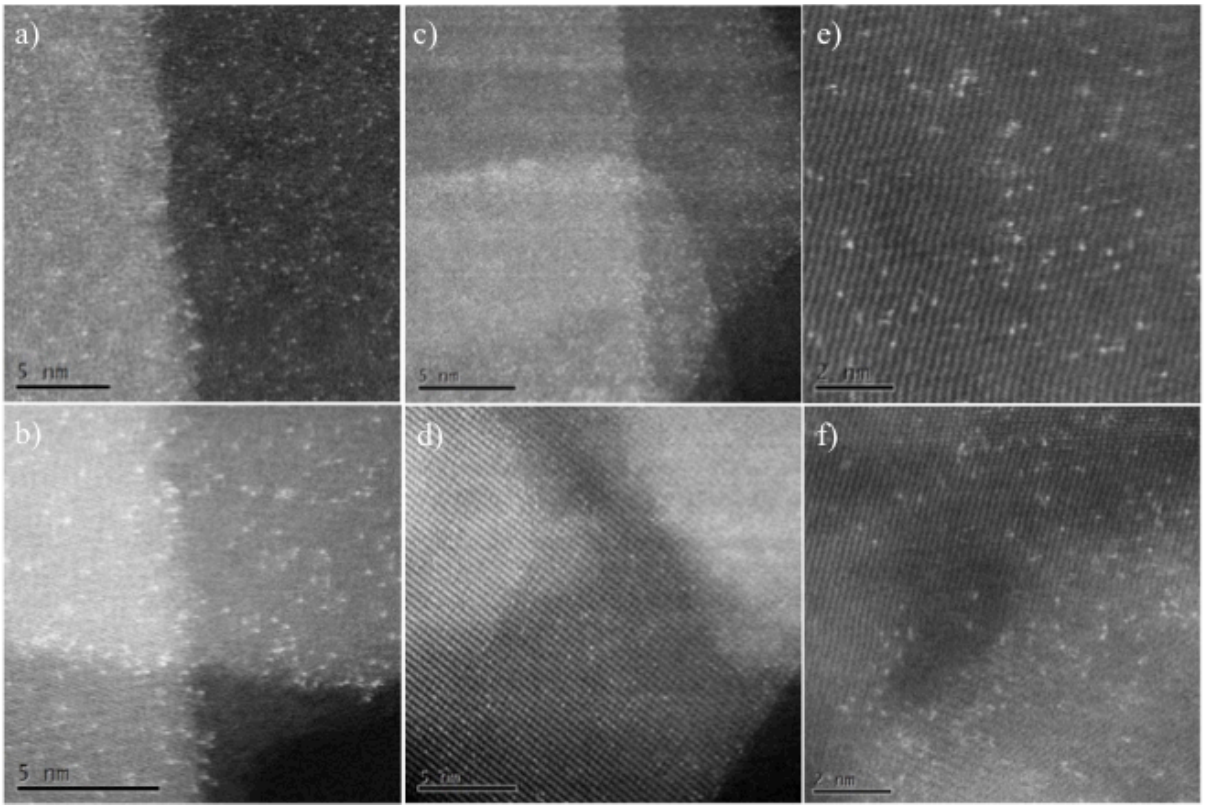

Figure 5.3.9. Representative Hi-Res High Angle Annual Dark Field (HAADF) STEM images of a)- b) **Ta-Calix**, c)- d) **Ta-Et,** e)- f) **Ta-ALD**.

These images enabled by the extended, flat surface of $nsTiO_2$ allows for statistically meaningful estimates (N = 134-186 Ta atoms) of the distribution of supported Ta atoms. The observed nearest neighbor distances (NND) are calculated for all visible Ta atoms in Figure 5.3.9 (individual histogram of NND are available in figure 5.3.10). The mean NND for materials **Ta-**

Et, **Ta-Calix**, and **Ta-ALD** are 0.6, 0.7, and 0.6nm. From the total amount of Ta grafted and the specific surface area of the nsTiO$_2$, perfectly randomly dispersed Ta on the surface would have an apparent Ta-Ta separation of 0.9 nm. The NND for perfectly randomly dispersed Ta atoms is calculated using the following equation: D=$\frac{0.5}{\sqrt{na}}$, where na stands for the surface loading of Ta atoms (0.3 group/nm^2).[128]

a)

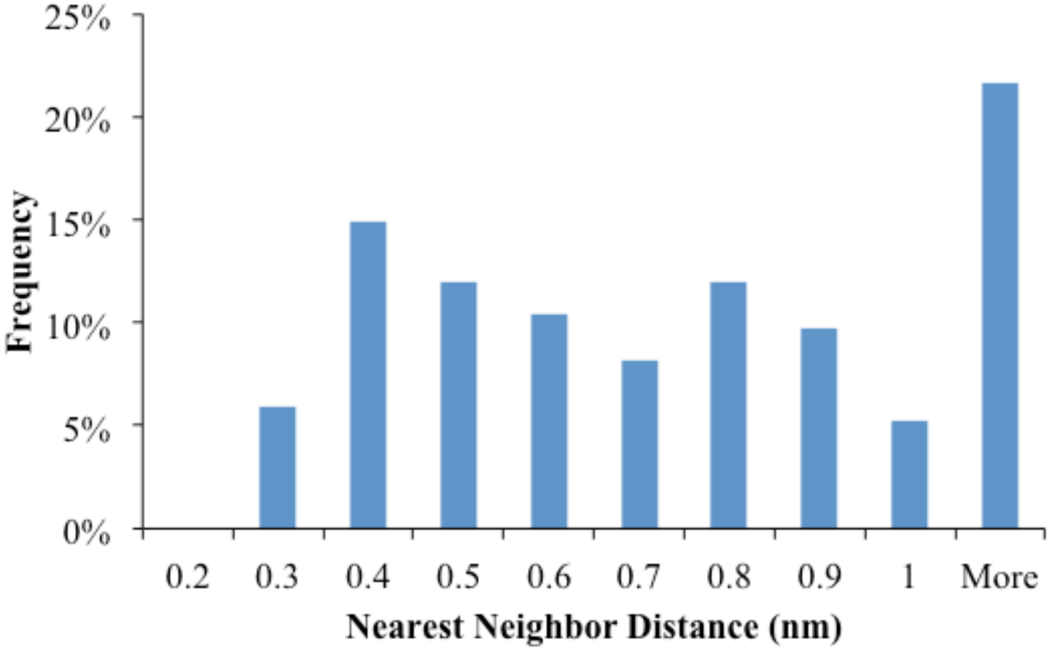
25%
20%
15%
10%
5%
0%
Frequency
0.2
0.3
0.4
0.5
0.6
0.7
0.8
0.9
1
More
Nearest Neighbor Distance (nm)

b)

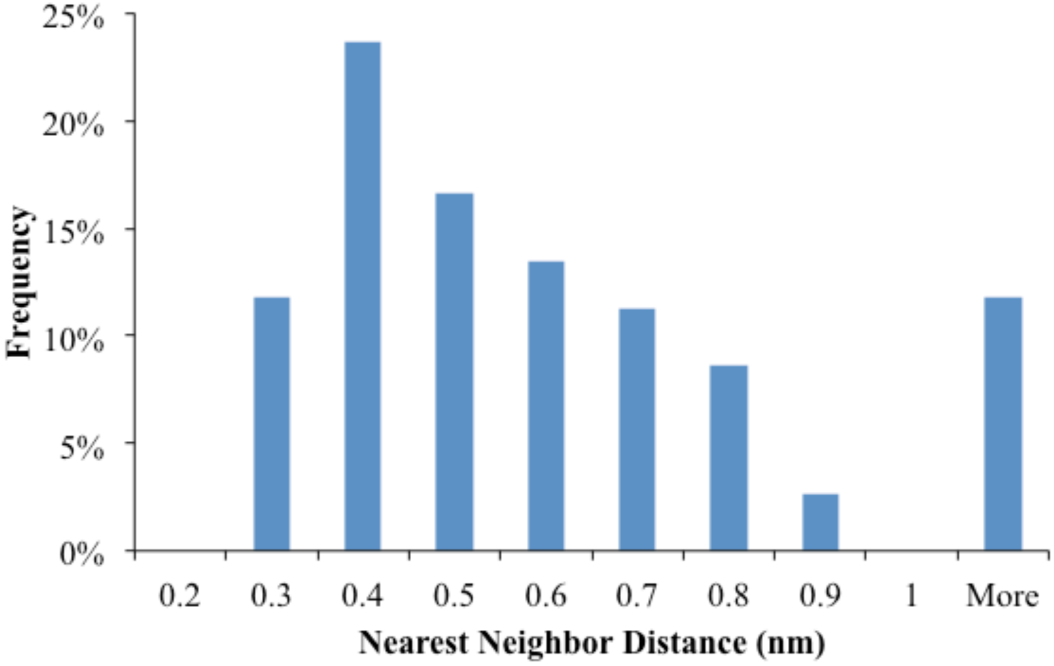
25%
20%
15%
10%
5%
0%
Frequency
0.2
0.3
0.4
0.5
0.6
0.7
0.8
0.9
1
More
Nearest Neighbor Distance (nm)

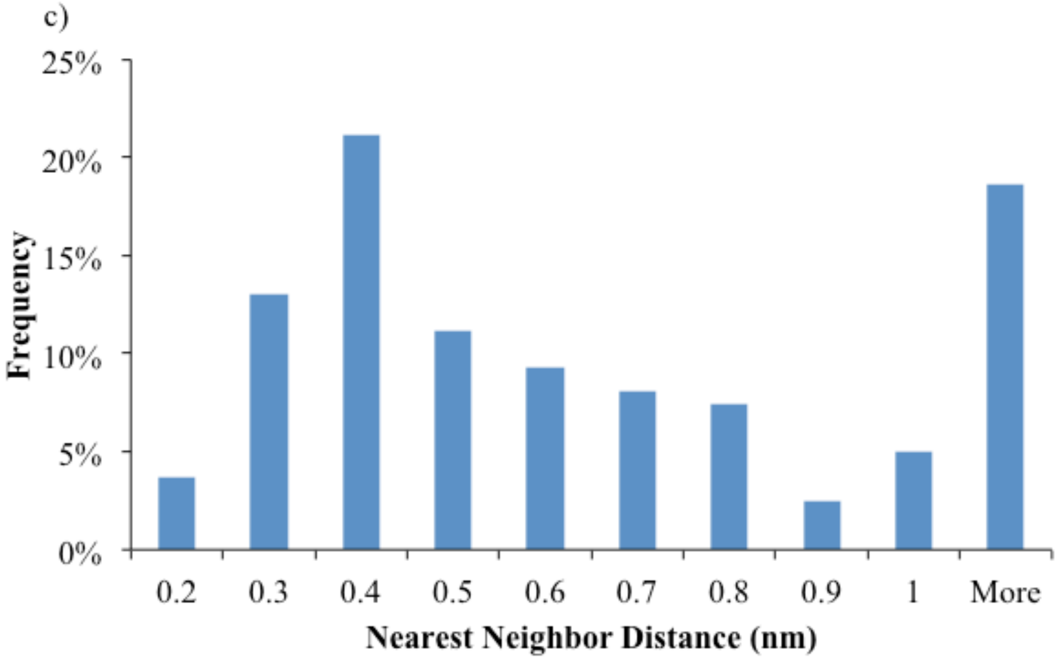

Figure 5.3.10. Histograms of NND of samples a) **Ta-Calix**, b) **Ta-Et** and c) **Ta-ALD**.

We also quantitatively estimate the fraction of Ta atoms that are 'isolated' from another, by placing a cutoff Ta-Ta separation of >0.4 nm from the nearest neighbor, equal to the Ta-O-Ta distance in Ta_2O_5.[129] The cumulative frequency distributions in Figure 5.3.11 show that for all materials, >60% of Ta atoms are isolated from each other, with potentially >80% of the Ta atoms being isolated in the case of Ta-Calix. These estimates are conservative, since Ta atoms on adjacent nanosheets are counted as they are on the same sheet, and Ta atoms that appear to be proximate may not actually be so. "Isolated" sites have long been argued from spectroscopy to be the most active sites in a number of reactions,[110,91] and many synthetic methods, including the use of bulky ligands such as calixarene,[117,68] have been specifically developed to bias the system towards a preponderance of these sites. For the first time, we have directly demonstrated the validity of these claims from HAADF-STEM imaging. The full analysis of the Ta-Ta distances also shows that the conditions of the ALD do indeed cause some rearrangement and aggregation of TaOx, even if the aggregation is not severe enough to be observed by bulk techniques.

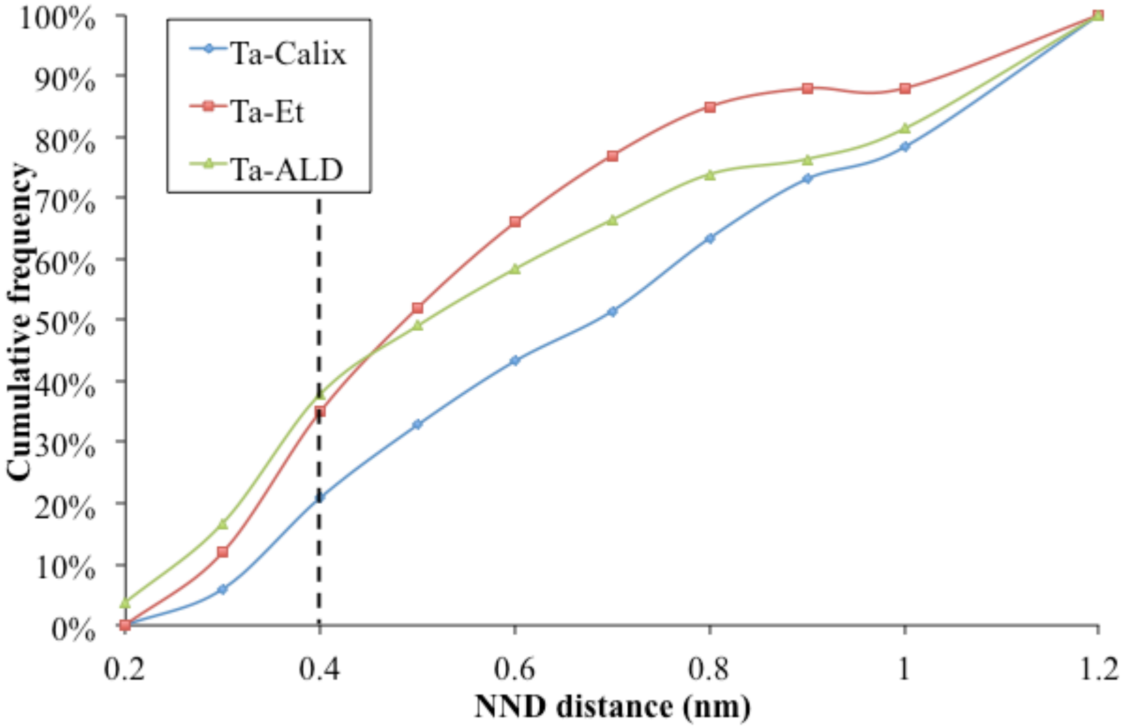

Figure 5.3.11. Cumulative frequency plot of nearest neighbor distance (Ta to Ta distance) for samples **Ta-Et** (186 atoms counted), **Ta-Calix** (134 atoms counted) and **Ta-ALD** (161 atoms counted).

5.4 Conclusion

In conclusion, we’ve demonstrated the use of TiO_2 nanosheets as excellent 2D supports for high resolution STEM imaging of highly dispersed supported oxides and quantification of atom-atom distance distributions. We are currently working to apply this technique to other catalytic systems.

References

1. Park, S.-J.; Lee, J.-P.; Jang, J. S.; Rhu, H.; Yu, H.; You, B. Y.; Kim, C. S.; Kim, K. J.; Cho, Y. J.; Baik, S. *Nanotechnology* **2013,** 24, (29), 295202.
2. Baerns, M., *Basic principles in applied catalysis*. Springer Science & Business Media: 2013; Vol. 75.
3. Ross, J. R., *Heterogeneous catalysis: fundamentals and applications*. Elsevier: 2011.
4. Farrauto, R. J.; Heck, R. M. *Catalysis Today* **1999,** 51, (3), 351-360.
5. Curry, S. *Platinum metals review* **1957,** 1, (2), 38-43.
6. Haruta, M. *Catalysis today* **1997,** 36, (1), 153-166.
7. Boccuzzi, F.; Chiorino, A.; Manzoli, M.; Andreeva, D.; Tabakova, T.; Ilieva, L.; Iadakiev, V. *Catalysis Today* **2002,** 75, (1), 169-175.
8. Van Santen, R. A. *Accounts of chemical research* **2008,** 42, (1), 57-66.
9. Bezemer, G. L.; Bitter, J. H.; Kuipers, H. P.; Oosterbeek, H.; Holewijn, J. E.; Xu, X.; Kapteijn, F.; van Dillen, A. J.; de Jong, K. P. *Journal of the American Chemical Society* **2006,** 128, (12), 3956-3964.
10. Xu, Z.; Xiao, F.-S.; Purnell, S.; Alexeev, O.; Kawi, S.; Deutsch, S.; Gates, B. *Nature* **1994,** 372, (6504), 346-348.
11. Bond, G. C. *Surface Science* **1985,** 156, 966-981.
12. Bell, A. T. *Science* **2003,** 299, (5613), 1688-1691.
13. Regalbuto, J., *Catalyst preparation: science and engineering*. CRC Press: 2016.
14. Schwarz, J. A.; Contescu, C.; Contescu, A. *Chemical Reviews* **1995,** 95, (3), 477-510.
15. Lambert, S.; Job, N.; D'Souza, L.; Pereira, M. F. R.; Pirard, R.; Heinrichs, B.; Figueiredo, J. L.; Pirard, J.-P.; Regalbuto, J. R. *Journal of Catalysis* **2009,** 261, (1), 23-33.
16. Miller, J. T.; Schreier, M.; Kropf, A. J.; Regalbuto, J. R. *Journal of Catalysis* **2004,** 225, (1), 203-212.
17. Zanella, R.; Giorgio, S.; Henry, C. R.; Louis, C. *The Journal of Physical Chemistry B* **2002,** 106, (31), 7634-7642.
18. by Metals, R. C. *Chem. Rev* **1995,** 95, 511-522.
19. Copéret, C.; Basset, J. M. *Advanced Synthesis & Catalysis* **2007,** 349, (1 ‐ 2), 78-92.
20. Wanke, S. E.; Flynn, P. C. *Catalysis Reviews* **1975,** 12, (1), 93-135.
21. Cao, A.; Lu, R.; Veser, G. *Physical Chemistry Chemical Physics* **2010,** 12, (41), 13499-13510.
22. Campbell, C. T.; Parker, S. C.; Starr, D. E. *Science* **2002,** 298, (5594), 811-814.
23. Challa, S. R.; Delariva, A. T.; Hansen, T. W.; Helveg, S.; Sehested, J.; Hansen, P. L.; Garzon, F.; Datye, A. K. *Journal of the american chemical society* **2011,** 133, (51), 20672-20675.
24. Hansen, T. W.; DeLaRiva, A. T.; Challa, S. R.; Datye, A. K. *Accounts of chemical research* **2013,** 46, (8), 1720-1730.
25. Prieto, G.; Zečević, J.; Friedrich, H.; De Jong, K. P.; De Jongh, P. E. *Nature materials* **2013,** 12, (1), 34-39.
26. Campbell, C. T. *Accounts of chemical research* **2013,** 46, (8), 1712-1719.

27. Lu, P.; Campbell, C. T.; Xia, Y. *Nano letters* **2013,** 13, 4957-62.

28. Lu, J.; Liu, B.; Greeley, J. P.; Feng, Z.; Libera, J. a.; Lei, Y.; Bedzyk, M. J.; Stair, P. C.; Elam, J. W. *Chemistry of Materials* **2012,** 24, 2047-2055.

29. Lu, J.; Fu, B.; Kung, M. C.; Xiao, G.; Elam, J. W.; Kung, H. H.; Stair, P. C. *Science* **2012,** 335, 1205-8.

30. Li, L.; King, D. L.; Liu, J.; Huo, Q.; Zhu, K.; Wang, C.; Gerber, M.; Stevens, D.; Wang, Y. *Chemistry of Materials* **2009,** 21, (22), 5358-5364.

31. Prieto, G.; Shakeri, M.; De Jong, K. P.; De Jongh, P. E. *ACS nano* **2014,** 8, (3), 2522-2531.

32. Joo, S. H.; Park, J. Y.; Tsung, C.-K.; Yamada, Y.; Yang, P.; Somorjai, G. A. *Nature materials* **2009,** 8, (2), 126-131.

33. Bore, M. T.; Pham, H. N.; Switzer, E. E.; Ward, T. L.; Fukuoka, A.; Datye, A. K. *The Journal of Physical Chemistry B* **2005,** 109, (7), 2873-2880.

34. Wichner, N. M.; Beckers, J.; Rothenberg, G.; Koller, H. *Journal of Materials Chemistry* **2010,** 20, (19), 3840-3847.

35. Yuranov, I.; Moeckli, P.; Suvorova, E.; Buffat, P.; Kiwi-Minsker, L.; Renken, A. *Journal of Molecular Catalysis A: Chemical* **2003,** 192, (1), 239-251.

36. Hartley, F. R., *Supported metal complexes: a new generation of catalysts*. Springer Science & Business Media: 2012; Vol. 6.

37. Chan, S. C.; Barteau, M. A. *Langmuir* **2005,** 21, (12), 5588-5595.

38. Ohyama, J.; Yamamoto, A.; Teramura, K.; Shishido, T.; Tanaka, T. *ACS Catalysis* **2011,** 1, (3), 187-192.

39. Jiao, L.; Regalbuto, J. R. *Journal of Catalysis* **2008,** 260, (2), 329-341.

40. Attia, Y., *Sol-gel processing and applications*. Springer Science & Business Media: 2012.

41. Bo, Z.; Eaton, T. R.; Gallagher, J. R.; Canlas, C. P.; Miller, J. T.; Notestein, J. M. *Chemistry of Materials* **2015,** 27, (4), 1269-1277.

42. Ardagh, M. A.; Bo, Z.; Nauert, S. L.; Notestein, J. M. *ACS Catalysis* **2016,** 6, (9), 6156-6164.

43. Yan, W.; Mahurin, S. M.; Pan, Z.; Overbury, S. H.; Dai, S. *Journal of the American Chemical Society* **2005,** 127, (30), 10480-10481.

44. George, S. M. *Chemical reviews* **2009,** 110, (1), 111-131.

45. O'Neill, B. J.; Jackson, D. H.; Lee, J.; Canlas, C.; Stair, P. C.; Marshall, C. L.; Elam, J. W.; Kuech, T. F.; Dumesic, J. A.; Huber, G. W. *ACS Catalysis* **2015,** 5, (3), 1804-1825.

46. O'Neill, B. J.; Jackson, D. H.; Crisci, A. J.; Farberow, C. A.; Shi, F.; Alba‐Rubio, A. C.; Lu, J.; Dietrich, P. J.; Gu, X.; Marshall, C. L. *Angewandte Chemie* **2013,** 125, (51), 14053-14057.

47. Schirmer, J.; Kim, J.; Klemm, E. *Journal of analytical and applied pyrolysis* **2001,** 60, (2), 205-217.

48. Storck, S.; Bretinger, H.; Maier, W. F. *Applied Catalysis A: General* **1998,** 174, (1), 137-146.

49. Brunauer, S.; Emmett, P. H.; Teller, E. *J. Am. Chem. Soc* **1938,** 60, (2), 309-319.

50. Imelik, B.; Vedrine, J. C., *Catalyst characterization: physical techniques for solid materials*. Springer Science & Business Media: 2013.

51. Rezaaiyaan, R.; Hieftje, G.; Anderson, H.; Kaiser, H.; Meddings, B. *Applied Spectroscopy* **1982,** 36, (6), 627-631.

52. Oura, K.; Lifshits, V.; Saranin, A.; Zotov, A.; Katayama, M., *Surface science: an introduction*. Springer Science & Business Media: 2013.

53. Hammer, B.; Morikawa, Y.; Nørskov, J. K. *Physical review letters* **1996,** 76, (12), 2141.

54. Stakheev, A. Y.; Shpiro, E.; Tkachenko, O.; Jaeger, N.; Schulz-Ekloff, G. *Journal of Catalysis* **1997,** 169, (1), 382-388.

55. Fan, Q.; Sha He, L. H.; Liu, X.; Zhu, Y.; Xu, S.; Zhang, F. *Scientific Reports* **2017,** 7.

56. Hagen, J., *Industrial catalysis: a practical approach*. John Wiley & Sons: 2015.

57. Somorjai, G. *Catalysis Letters* **1990,** 7, (1), 169-182.

58. Zaera, F.; Somorjai, G. *J. Am. Chem. Soc.;(United States)* **1984,** 106, (8).

59. Cremer, P. S.; Su, X.; Shen, Y. R.; Somorjai, G. A. *The Journal of Physical Chemistry* **1996,** 100, (40), 16302-16309.

60. Tauster, S.; Fung, S.; Garten, R. L. *Journal of the American Chemical Society* **1978,** 100, (1), 170-175.

61. Tauster, S.; Fung, S.; Baker, R.; Horsley, J. *Science* **1981,** 211, (4487), 1121-1125.

62. Sondi, I.; Salopek-Sondi, B. *Journal of colloid and interface science* **2004,** 275, (1), 177-182.

63. Kestenbaum, H.; Lange de Oliveira, A.; Schmidt, W.; Schüth, F.; Ehrfeld, W.; Gebauer, K.; Löwe, H.; Richter, T.; Lebiedz, D.; Untiedt, I. *Industrial & engineering chemistry research* **2002,** 41, (4), 710-719.

64. Grünert, W.; Brückner, A.; Hofmeister, H.; Claus, P. *The Journal of Physical Chemistry B* **2004,** 108, (18), 5709-5717.

65. Flura, A.; Courtois, X.; Can, F.; Royer, S.; Duprez, D. *Topics in Catalysis* **2013,** 56, (1-8), 94-103.

66. Notestein, J. M.; Iglesia, E.; Katz, A. *methods* **2007,** 9, 13.

67. Eaton, T. R.; Campos, M. P.; Gray, K. A.; Notestein, J. M. *Journal of Catalysis* **2014,** 309, 156-165.

68. Canlas, C. P.; Lu, J.; Ray, N. a.; Grosso-Giordano, N. a.; Lee, S.; Elam, J. W.; Winans, R. E.; Van Duyne, R. P.; Stair, P. C.; Notestein, J. M. *Nature chemistry* **2012,** 4, 1030-6.

69. Courrol, L. C.; de Oliveira Silva, F. R.; Gomes, L. *Colloids and Surfaces A: Physicochemical and Engineering Aspects* **2007,** 305, (1), 54-57.

70. Miller, J.; Kropf, A.; Zha, Y.; Regalbuto, J.; Delannoy, L.; Louis, C.; Bus, E.; Van Bokhoven, J. *Journal of Catalysis* **2006,** 240, (2), 222-234.

71. Friedrich, H.; de Jongh, P. E.; Verkleij, A. J.; de Jong, K. P. *Chemical reviews* **2009,** 109, (5), 1613-1629.

72. Min, B.; Wallace, W.; Santra, A.; Goodman, D. *Journal of Physical Chemistry B* **2004,** 108, 16339-16343.

73. Xin, B.; Jing, L.; Ren, Z.; Wang, B.; Fu, H. *The Journal of Physical Chemistry B* **2005,** 109, (7), 2805-2809.

74. Jiang, Z.; Ouyang, Q.; Peng, B.; Zhang, Y.; Zan, L. *Journal of Materials Chemistry A* **2014,** 2, (46), 19861-19866.

75. Zhai, Y.; Pierre, D.; Si, R.; Deng, W.; Ferrin, P.; Nilekar, A. U.; Peng, G.; Herron, J. A.; Bell, D. C.; Saltsburg, H. *Science* **2010,** 329, (5999), 1633-1636.

76. Panagiotopoulou, P.; Kondarides, D. I. *Catalysis Today* **2006,** 112, (1), 49-52.

77. Yoo, J. W.; Hathcock, D.; El-Sayed, M. A. *The Journal of Physical Chemistry A* **2002,** 106, (10), 2049-2054.

78. Makosch, M.; Lin, W.-I.; Bumbálek, V.; Sá, J.; Medlin, J. W.; Hungerbühler, K.; van Bokhoven, J. A. *ACS Catalysis* **2012,** 2, (10), 2079-2081.

79. Kahsar, K. R.; Schwartz, D. K.; Medlin, J. W. *Journal of the American Chemical Society* **2014,** 136, (1), 520-526.

80. Huang, D.; Zhang, B.; Bai, J.; Zhang, Y.; Wittstock, G.; Wang, M.; Shen, Y. *Electrochimica Acta* **2014,** 130, 97-103.

81. Paulus, U. A.; Wokaun, A.; Scherer, G. G.; Schmidt, T. J.; Stamenkovic, V.; Radmilovic, V.; Markovic, N. M.; Ross, P. N. *The Journal of Physical Chemistry B* **2002,** 106, (16), 4181-4191.

82. Bo, Z.; Eaton, T. R.; Gallagher, J. R.; Canlas, C. P.; Miller, J. T.; Notestein, J. M. *Chemistry of Materials* **2015,** 27, (4), 1269-1277.

83. Brinker, C. J.; Scherer, G. W., *Sol-gel science: the physics and chemistry of sol-gel processing*. Academic press: 2013.

84. Notestein, J. M.; Iglesia, E.; Katz, A. *Chemistry of Materials* **2007,** 19, (20), 4998-5005.

85. Bamwenda, G. R.; Tsubota, S.; Nakamura, T.; Haruta, M. *Catalysis Letters* **1997,** 44, (1-2), 83-87.

86. Kim, M.-Y.; Choi, J.-S.; Toops, T.; Jeong, E.-S.; Han, S.-W.; Schwartz, V.; Chen, J. *Catalysts* **2013,** 3, (1), 88-103.

87. Liu, R. J.; Crozier, P. A.; Smith, C. M.; Hucul, D. A.; Blackson, J.; Salaita, G. *Applied Catalysis A: General* **2005,** 282, (1–2), 111-121.

88. Flytzani-Stephanopoulos, M.; Gates, B. C. *Annual review of chemical and biomolecular engineering* **2012,** 3, 545-574.

89. Lin, J.; Wang, A.; Qiao, B.; Liu, X.; Yang, X.; Wang, X.; Liang, J.; Li, J.; Liu, J.; Zhang, T. *Journal of the American Chemical Society* **2013,** 135, (41), 15314-15317.

90. Yang, X.-F.; Wang, A.; Qiao, B.; Li, J.; Liu, J.; Zhang, T. *Accounts of chemical research* **2013,** 46, (8), 1740-1748.

91. Yang, M.; Allard, L. F.; Flytzani-Stephanopoulos, M. *Journal of the American Chemical Society* **2013,** 135, (10), 3768-3771.

92. Yang, M.; Li, S.; Wang, Y.; Herron, J. A.; Xu, Y.; Allard, L. F.; Lee, S.; Huang, J.; Mavrikakis, M.; Flytzani-Stephanopoulos, M. *Science* **2014,** 346, (6216), 1498-1501.

93. Liu, P.; Zhao, Y.; Qin, R.; Mo, S.; Chen, G.; Gu, L.; Chevrier, D. M.; Zhang, P.; Guo, Q.; Zang, D. *Science* **2016,** 352, (6287), 797-800.

94. Samad, J. E.; Hoenig, S.; Regalbuto, J. R. *ChemCatChem* **2015,** 7, (21), 3460-3463.

95. Feltes, T. E.; Espinosa-Alonso, L.; de Smit, E.; D'Souza, L.; Meyer, R. J.; Weckhuysen, B. M.; Regalbuto, J. R. *Journal of Catalysis* **2010,** 270, (1), 95-102.

96. Grosso-Giordano, N. A.; Eaton, T. R.; Bo, Z.; Yacob, S.; Yang, C.-C.; Notestein, J. M. *Applied Catalysis B: Environmental* **2016,** 192, 93-100.

97. Kittaka, S. *Journal of Colloid and Interface Science* **1974,** 48, (2), 327-333.

98. Schwarz, J.; Driscoll, C.; Bhanot, A. *Journal of Colloid and Interface Science* **1984,** 97, (1), 55-61.

99. Cuddy, M. F.; Poda, A. R.; Brantley, L. N. *ACS applied materials & interfaces* **2013,** 5, (9), 3514-3518.

100. Júnior, J. A. A.; Baldo, J. B. **2014**.

101. Ding, K.; Gulec, A.; Johnson, A. M.; Schweitzer, N. M.; Stucky, G. D.; Marks, L. D.; Stair, P. C. *Science* **2015,** 350, (6257), 189-192.

102. De Mallmann, A.; Barthomeuf, D. *Studies in surface science and catalysis* **1989,** 46, 429-438.

103. De Menorval, L.-C.; Chaqroune, A.; Coq, B.; Figueras, F. *Journal of the Chemical Society, Faraday Transactions* **1997,** 93, (20), 3715-3720.

104. Weckhuysen, B. M.; Keller, D. E. *Catalysis Today* **2003,** 78, (1), 25-46.

105. Eaton, T. R.; Boston, A. M.; Thompson, A. B.; Gray, K. A.; Notestein, J. M. *ChemCatChem* **2014,** 6, (11), 3215-3222.

106. Nozaki, C.; Lugmair, C. G.; Bell, A. T.; Tilley, T. D. *Journal of the American Chemical Society* **2002,** 124, (44), 13194-13203.

107. Hess, C.; Hoefelmeyer, J. D.; Tilley, T. D. *The Journal of Physical Chemistry B* **2004,** 108, (28), 9703-9709.

108. Chen, Y.; Fierro, J. L.; Tanaka, T.; Wachs, I. E. *Journal of Physical Chemistry B* **2003,** 107, (22), 5243-5250.

109. Fu, Q.; Saltsburg, H.; Flytzani-Stephanopoulos, M. *Science* **2003,** 301, (5635), 935-938.

110. Kistler, J. D.; Chotigkrai, N.; Xu, P.; Enderle, B.; Praserthdam, P.; Chen, C. Y.; Browning, N. D.; Gates, B. C. *Angewandte Chemie* **2014,** 126, (34), 9050-9053.

111. Fernandez-Garcia, M.; Martinez-Arias, A.; Hanson, J.; Rodriguez, J. *Chemical Reviews* **2004,** 104, (9), 4063-4104.

112. Buurmans, I. L.; Weckhuysen, B. M. *Nature chemistry* **2012,** 4, (11), 873-886.

113. Gao, X.; Wachs, I. E. *Topics in Catalysis* **2002,** 18, (3), 243-250.

114. Iglesia, E. *Applied Catalysis A: General* **1997,** 161, (1-2), 59-78.

115. Han, X.; Kuang, Q.; Jin, M.; Xie, Z.; Zheng, L. *J. Am. Chem. Soc.* **2009,** 131, (9), 3152-3153.

116. Liang, Y. T.; Vijayan, B. K.; Lyandres, O.; Gray, K. A.; Hersam, M. C. *J. Phys. Chem. Lett.* **2012**, 1760-1765.

117. Morlanés, N.; Notestein, J. M. *Journal of Catalysis* **2010,** 275, (2), 191-201.

118. Thornburg, N. E.; Thompson, A. B.; Notestein, J. M. *ACS Catalysis* **2015,** 5, (9), 5077-5088.

119. Elam, J. W.; Groner, M. D.; George, S. M. *Rev. Sci. Instrum.* **2002,** 73, (8), 2981-2987.

120. Groner, M. D.; Fabreguette, F. H.; Elam, J. W.; George, S. M. *Chem. Mater.* **2004,** 16, (4), 639-645.

121. Ingale, S. V.; Wagh, P. B.; Tripathi, A. K.; Srivastav, R. S.; Singh, I. K.; Bindal, R. C.; Gupta, S. C. **2012**.
122. Södergren, S.; Siegbahn, H.; Rensmo, H.; Lindström, H.; Hagfeldt, A.; Lindquist, S.-E. *The Journal of Physical Chemistry B* **1997,** 101, (16), 3087-3090.
123. Masuda, Y.; Wakamatsu, S.; Koumoto, K. *Journal of the European Ceramic Society* **2004,** 24, (2), 301-307.
124. Liu, J.; Yang, H.; Tan, W.; Zhou, X.; Lin, Y. *Electrochimica Acta* **2010,** 56, (1), 396-400.
125. Liu, X.; Wu, X.; Scott, K. *Catalysis Science & Technology* **2014,** 4, (11), 3891-3898.
126. Chen, Y.; Fierro, J. L.; Tanaka, T.; Wachs, I. E. *The Journal of Physical Chemistry B* **2003,** 107, (22), 5243-5250.
127. Gao, X.; Wachs, I. E. *Catalysis Today* **1999,** 51, (2), 233-254.
128. Pinder, D.; Witherick, M. *Geography* **1972**, 277-288.
129. Takahara, Y.; Kondo, J. N.; Takata, T.; Lu, D.; Domen, K. *chemistry of materials* **2001,** 13, (4), 1194-1199.